UNIVERSITÄT BONN
Physikalisches Institut

Observation of top quark pair production and estimation of W+jets background with ATLAS at the LHC

by

Bálint Radics

Top quark pair production, in events with one muon, missing transverse energy and with at least four jets, has been studied with the ATLAS detector at the Large Hadron Collider, using the data recorded from March until September of 2010, with corresponding integrated luminosity of $\mathcal{L} = 2.9$ pb^{-1}. The two major background rates, multijet and W boson with associated jet productions, have been estimated from control regions in the data. The observed number of events in the control and signal regions have been compared with the Monte Carlo predictions.

Postal address:
Nußallee 12
D-53115 Bonn
Germany

BONN-IR-2010-14
Bonn University
November 2010
ISSN-0172-8741

UNIVERSITÄT BONN
Physikalisches Institut

Observation of top quark pair production and estimation of W+jets background with ATLAS at the LHC

by

Bálint Radics

Referent:	Prof. Ian C. Brock
Korreferent:	Prof. Norbert Wermes

Angenommen am:	04.10.2010
Tag der Promotion:	30.11.2010

Contents

List of Figures

List of Tables

Acknowledgements

First of all, I would like to thank to my advisor, Prof. Ian C. Brock, for all the unbelievable patience, trust and support I have received from him during the three and a half years I have spent in Bonn and at CERN, Geneva.

During my top quark pair analysis and work at the ATLAS experiment I got invaluable help from the following people: Max Baak, Marcello Barisonzi, Ilaria Besana, Sebastien Binet, James Catmore, David Cote, Martijn Gosselink, Richard Hawkings, Andreas Höcker, Karsten Köneke, Péter Kövesárki, Attila Krasznahorkay, Tommaso Lari, Marjorie Shapiro, Akira Shibata, Jörg Stelzer, Eric Torrence, Wouter Verkerke, Viktor Veszprémi and Ivo van Vulpen.

Then I would like to thank to the members of the Bonn Group who helped me during my time (and sorry if I forgot anybody): Detlef Bartsch, Markus Cristinziani, Prof. Klaus Desch, Sebastian Fleischmann, Götz Gayken, Marc Lehmacher, Agnieszka Leyko, Thomas Loddenkötter, Markus Jüngst, Gia Khoriauli, Lucia Masetti, Klemens Müller, Gizo Nanava, Guilherme Nunes Hanninger, Adriana Elizabeth Nuncio Quiroz, Marc-André Pleier, Robindra Prabhu, Verena Schönberg, Jan Schumacher, Jan Stillings, Duc Bao Ta, Kirika Uchida, Nikolai Vlasov, Prof. Norbert Wermes and Michal Własenko.

Thanks also for the help I received from these people: Hugo Beauchemin, Janet Dietrich, Davide Forcella, Dezső Horváth, Larry Hudson, Ádám Kardos, Christoffer Peterson, Gábor Somogyi, Kerim Suruliz, Cyril Topfel, Alessandro Tricoli, Zoltán Trócsányi and Panteleimon Tziveloglou (Pantelis).

Last but not least, I would like to thank to my family, including our beloved cat, Edison.

Chapter 1

Introduction

In the 20th century the universe has been found to be ultimately built from two types of fundamental particles: quarks and leptons. The interactions between these particles are mediated by gauge bosons which are derivable from basic symmetry laws. Technology today is able to provide machines that can produce these fundamental particles under clean circumstances in the laboratory, letting us investigate them in a reproducible way. In fact it is not only possible to produce the elementary particles but it is also possible to create new ones that can only exist in laboratory because it takes so much energy to produce them, and because their lifetime is so short, that there is no chance that they exist elsewhere in the whole universe as we know it.
Six types of quarks, and six types of leptons (and also corresponding antiquarks and antileptons) have been found. The top quark is the last and heaviest. Historically it has been discovered at the D0 [2] and CDF [3] experiments in 1995 at the Tevatron proton-antiproton collider in 2 TeV center-of-mass energy collisions. Since then a tremendous amount of study has been performed to precisely measure its mass and production cross section at this energy scale. The first 7 TeV proton-proton collisions of the Large Hadron Collider open up the possibility to study these properties of the top quark at even higher energies and to put further constraints on the Standard Model of elementary particle physics. This thesis discusses the simulation and first observation of the top quark in the ATLAS experiment [4] at the Large Hadron

collider in 2.9 pb^{-1} integrated luminosity of collision data.

The structure of the thesis is the following. Chapter 2 gives an introduction to the Standard Model of particle physics and the role of the top quark in it, and discusses the production and decays of the top signal and background processes. Chapter 3 describes the detector system of the ATLAS experiment. The reconstruction of electrons, jets, missing transverse energy and muons in the experiment is detailed in Chapter 4. The event selection analysis and the background estimation methods used in the measurement is described in Chapter 5. The extraction and the statistical significance of the observed signal excess is discussed in Chapter 6. The thesis closes with a summary in Chapter 7.

Chapter 2

Top quark and the Standard Model

2.1 Introduction to the Standard Model

The Standard Model of elementary particles is an effective quantum field theory with gauge fields mediating interactions between particle fields [5]. The gauge fields arise from a special symmetry requirement: the fundamental Lagrangian describing the physical system must be invariant against local transformations of certain kinds. Each symmetry transformation is also reflected in conserved quantities of the physical system. Historically the first successful quantum field theory was the quantum electrodynamics (QED), describing the interaction of fermions mediated by photons. The fundamental Lagrangian density describing the physical system of spin-1/2 fermions is given in terms of four-component spinor fields,

$$\mathcal{L} = \bar{\psi}(i\gamma_\mu \partial^\mu - m\mathbb{1})\psi, \tag{2.1}$$

where γ^μ are the 4×4 Dirac matrices, acting on the four-component spinor fields, ψ, and having four Lorentz components, and $\mathbb{1}$ is the 4×4 unit matrix [6]. Following the classical Lagrangian mechanics we assume that an action integral can be defined which would yield an extremum on the real path of the particle between some space-time boundaries,

$$S = \int_a^b \mathcal{L}\, d^4x. \tag{2.2}$$

This means that the variation of the action integral, between fixed space-time boundaries, must disappear

$$0 = \delta S = \delta \int_{\text{fix}} d^4x \mathcal{L} = \int_{\text{fix}} d^4x \left\{ \frac{\partial \mathcal{L}}{\partial \psi} \delta\psi + \frac{\partial \mathcal{L}}{\partial(\partial_\mu \psi)} \delta(\partial_\mu \psi) \right\}. \tag{2.3}$$

When integrating by parts on the second term the boundary term vanishes because the end points of the integral are fixed,

$$0 = \delta S = \int_{\text{fix}} d^4x \frac{\partial \mathcal{L}}{\partial \psi} \delta\psi + \underbrace{\left[\frac{\partial \mathcal{L}}{\partial(\partial_\mu \psi)} \delta\psi \right]_{\text{fix}}}_{0} - \int_{\text{fix}} d^4x \partial_\mu \left(\frac{\partial \mathcal{L}}{\partial(\partial_\mu \psi)} \right) \delta\psi, \tag{2.4}$$

which means that the following integral vanishes

$$0 = \int_{\text{fix}} d^4x \left\{ \frac{\partial \mathcal{L}}{\partial \psi} - \partial_\mu \left(\frac{\partial \mathcal{L}}{\partial(\partial_\mu \psi)} \right) \right\} \delta\psi. \tag{2.5}$$

The domain of the integral is non-vanishing, therefore the integrand must vanish over the entire domain of integration which leads to the field equivalent of the classical Euler-Lagrange equation

$$0 = \frac{\partial \mathcal{L}}{\partial \psi} - \partial_\mu \left(\frac{\partial \mathcal{L}}{\partial(\partial_\mu \psi)} \right). \tag{2.6}$$

Substituting the Lagrangian density for the spin-1/2 fermion system in equation (2.1) provides the equation of motion for the spinor field, the Dirac equation,

$$(i\gamma^\mu \partial_\mu - m\mathbb{1})\psi = 0. \tag{2.7}$$

In the same manner one can derive the equation of motion for scalar or vector fields. The significance of this is that knowing the equation of motion of certain types of fields it is possible to describe scattering processes by finding the corresponding Green functions of the fields and using them in the analytical calculation for the physical amplitude of any hard scattering process. The mediators of the interactions of the spinor fields arise upon demanding symmetry invariance on the Lagrangian. The fundamental invariance principle is local gauge invariance. Local gauge invariance means that the following phase transformation leaves the Lagrangian invariant

$$\psi \rightarrow e^{i\alpha(x)}\psi. \tag{2.8}$$

Because the phase, $\alpha(x)$, depends on the space-time position the partial derivative terms leave a new phase term in the Lagrangian after the transformation, therefore it is not invariant. The interesting solution to this problem is to introduce new fields into the equation and therefore redefine the derivative,

$$\partial_\mu \rightarrow \mathrm{D}_\mu \equiv \partial_\mu - ieA_\mu, \tag{2.9}$$

and also require a certain transformation property for the new field,

$$A_\mu \rightarrow A_\mu + \frac{1}{e}\partial_\mu\alpha \tag{2.10}$$

where the vector field, A_μ, is called the gauge field. The vector field is a spin-1 particle, therefore a boson. This example of a $U(1)$ symmetry transformation invariance has serious consequences. With a knowledge of the symmetry group describing properties of a certain physical system of particles one can generate the gauge fields mediating the interactions. Quantum electrodynamics successfully describes interacting fermions at atomic level. It predicts lifetimes of order $10^{-20} \rightarrow 10^{-16}s$ for particles decaying via electromagnetic interactions (e.g. $\pi^0 \rightarrow \gamma\gamma$). But it couldn't explain the lifetime of order $\sim 10^{-8}s$ the of the pion, $\pi^- \rightarrow \mu^-\bar{\nu}$. Decay processes have been found with even shorter lifetimes, $\sim 10^{-23}s$ (e.g. $\Delta^{++} \rightarrow p\pi^+$). High energy collider experiments have found during the course of the 20th century that at subatomic and subnuclear levels there are two further fundamental interactions, the weak and strong interactions, responsible for these lifetimes. The corresponding symmetry groups of the weak and the strong interactions were found to be $SU(2)$ and $SU(3)$. The choice of $SU(2)$ group for the weak interaction emerged from two observations. The first is that there are three massive vector bosons mediating interactions: the W$^{\pm}$ [7] and the Z bosons [8], the second is that these interactions typically involve a lepton and a neutrino, therefore rotating in an abstract two-dimensional space of the different fermion fields. The reason for choosing $SU(3)$ as the fundamental symmetry group of the strong interactions was that experimentally it has been found that baryons contain three constituents, the quarks. The quarks have been found to be fermions forming a three-body bound state in baryons. However, according to the Pauli principle two fermions cannot occupy the same quantum state. Therefore they must have an internal quantum number, a new degree of freedom. Thus, the corresponding symmetry transformation rotates in a three dimensional abstract space, which was historically called color-space, reflecting the abstract notion of three fundamental colors (red, green, blue).

The fourth interaction, gravitation, cannot take a fundamental role in high energy interactions because the mass scale of the fundamental particles (quarks, leptons, and mediating gauge bosons) is so small that the coupling (which happens via the masses of the interacting particles) of the gravitational interaction is completely negligible.

Therefore the three fundamental interactions experimentally found and playing a significant role in high energy particle interactions at colliders are the electromagnetic, the weak and the strong interactions, the symmetries of which are given by three groups, $U(1)$, $SU(2)$ and $SU(3)$, respectively. As mentioned before, the fundamental Lagrangian describing the physical system can be constructed to contain the fermions and, with certain local gauge invariance constraints, the interactions with the vector bosons as well. However, the vector bosons also have their own dynamics, therefore invariant terms for them can be plugged into the Lagrangian.

For the electromagnetic interactions the photon fields can be described by the field strength tensor

$$F_{\mu\nu} = \partial_\mu A_\nu - \partial_\nu A_\mu \tag{2.11}$$

in the form

$$\mathcal{L} = -\frac{1}{4} F_{\mu\nu} F^{\mu\nu}. \tag{2.12}$$

We are thus lead to the Lagrangian of the QED

$$\mathcal{L} = \bar{\psi}(i\gamma^\mu \partial_\mu - m\mathbb{1})\psi + e\bar{\psi}\gamma^\mu A_\mu \psi - \frac{1}{4} F_{\mu\nu} F^{\mu\nu}. \tag{2.13}$$

The Standard Model is however able to unite QED and the weak interactions in a single framework, the electroweak theory. It was formulated by Glashow, Salam, and Weinberg in the middle of the 1960s [9] [10]. On similar grounds as quantum electrodynamics one constructs the fundamental Lagrangian, but separates the left- and right-handed components of the spinors

$$\psi_L = \frac{1-\gamma^5}{2}\psi, \; \psi_R = \frac{1+\gamma^5}{2}\psi. \tag{2.14}$$

Since the weak interaction involves a lepton and a neutrino, and acts only on left handed particles [11] [12] [13], the Lagrangian is constructed from $SU(2)$ doublets, $\psi_L = (\ell_L \;\; \nu_{\ell,L})$, and $SU(2)_L$ singlets, $\psi_R = (\ell_R)$. We require then that the Lagrangian is invariant under $SU(2)_L \times U(1)_Y$ transformation, where L denotes the left-handedness and Y is called the weak hypercharge which is equal to -1 for the left-handed fermion doublets and -2 for the right-handed fermion singlets. Similar to the QED the invariance is fulfilled if new vector fields are introduced

$$\mathrm{D}_\mu = \partial_\mu - i\left(g\frac{\vec{\tau}}{2}\vec{W}_\mu + g'\frac{Y}{2}B_\mu \right), \tag{2.15}$$

where the W^a_μ $(a = 1, 2, 3)$ gauge fields correspond to the $SU(2)_L$ and B_μ to the $U(1)_Y$ transformations, g and g' are the coupling constants of the two interactions and τ^a are the 2×2 Pauli matrices which generate rotations in the $SU(2)$ space. The hypercharge, Y, is related to the electric charge, Q, and the weak isospin, T, as $Q = T_3 + \frac{Y}{2}$. The Lagrangian contains the gauge fields in their weak eigenstates but the physically observable bosons are in their mass eigenstates. Indeed the Pauli matrices, acting as generators of $SU(2)$, mix up the $\vec{W}_\mu$ and B_μ fields in such a way that one gets the gauge field terms as a 2 × 2 matrix as

$$\begin{pmatrix} gW^3_\mu + g'B_\mu & g(W^1_\mu - iW^2_\mu)/\sqrt{2} \\ g(W^1_\mu + iW^2_\mu)/\sqrt{2} & -gW^3_\mu + g'B_\mu \end{pmatrix} \tag{2.16}$$

where, introducing $\tan\theta_W = g'/g$, one can identify the physical fields for the $W^\pm$ bosons as,

$$W^\pm_\mu = \frac{1}{\sqrt{2}}(W^1_\mu \mp iW^2_\mu) \tag{2.17}$$

and for the photon and Z fields as

$$A_\mu = \cos\theta_W B_\mu + \sin\theta_W W^3_\mu \tag{2.18}$$

$$Z_\mu = -\sin\theta_W B_\mu + \cos\theta_W W^3_\mu \tag{2.19}$$

and the corresponding invariant field strength tensors are

$$B_{\mu\nu} = \partial_\mu B_\nu - \partial_\nu B_\mu \tag{2.20}$$

$$\vec{W}_{\mu\nu} = \partial_\mu \vec{W}_\nu - \partial_\nu \vec{W}_\mu + g\vec{W}_\mu \times \vec{W}_\nu \tag{2.21}$$

where the last term for $\vec{W}_{\mu\nu}$ comes from the fact that $SU(2)$ is a non-abelian group. This property leads to self-interaction terms for the weak gauge bosons as well as interactions between them, while there is no self interaction for $U(1)$ as the photon doesn't interact with itself. One can already predict that the $SU(3)$ group, describing the color interaction between quarks, will also exhibit self-interaction between the corresponding mediating gauge bosons. So far the fermions and the electroweak gauge bosons were massless, there were no explicit mass terms introduced into the Lagrangian. Experimentally three different massive leptons have been found: the electron, the muon and the tau lepton. Also, neutrinos have been found associated with these leptons and it has been confirmed that there are also three types of neutrinos, each of them forming a weak doublet with one of the leptons. These $SU(2)$ weak doublets are traditionally called lepton families and the understanding of their multiplicity of three in nature is commonly believed to be of fundamental importance. However, there is no experimental sign of

fourth, or further lepton families yet.
So far there was no mention on the origin of the masses of the fundamental fermions and gauge bosons which are free parameters of the Standard Model. The solution has been proposed by Higgs [14] in 1964 but its validity still has not been proved experimentally. The proposal is the introduction of a new field, the *Higgs field*, with which every fermion and boson interacts, but in such a way that certain symmetries are broken. The Higgs field in the Standard Model is a complex doublet field, $\Phi = (\Phi^+, \Phi^0)$. This means four real fields which are needed to generate masses for the three gauge bosons, $W^\pm$ and Z. Assume a potential of the field of form, $V(\Phi) = -\mu^2|\Phi|^2 + \lambda|\Phi|^4$. This potential has a minimum at $|\Phi|^2 = v^2/2$, $v = \sqrt{\mu^2/\lambda}$. The spontaneous symmetry breaking occurs when Φ develops a vacuum expectation value at this minimum. The ground state of the field is chosen to break the $SU(2)$ and $U(1)_Y$ symmetries but not the $U(1)_{EM}$ (the electromagnetic gauge symmetry, the photon has zero mass). The minimal doublet field can be expressed as a perturbation of the field around the vacuum expectation value, v, and any unphysical degrees of freedom can be eliminated by choosing a proper unitary gauge using the invariance. After spontaneously breaking the symmetry the doublet field in the ground state is

$$\Phi_0 = \frac{1}{\sqrt{2}} \begin{pmatrix} 0 \\ v \end{pmatrix} . \tag{2.22}$$

Expressing the Higgs field as a perturbation around the vacuum,

$$\Phi_0 = \frac{1}{\sqrt{2}} \begin{pmatrix} 0 \\ v + h \end{pmatrix} , \tag{2.23}$$

the gauge boson masses can be generated as an interaction with the Higgs field. Writing the Lagrangian of the Higgs field one arrives at

$$\begin{aligned}\mathcal{L}_{\Phi} =&(D_{\mu}\Phi)^{\dagger}(D_{\mu}\Phi) - V(\Phi) = \left|\left(\partial_{\mu} - ig\frac{\vec{\tau}}{2}\vec{W}_{\mu} - g'\frac{Y}{2}B_{\mu}\right)\frac{v+h}{\sqrt{2}}\begin{pmatrix}0\\1\end{pmatrix}\right|^{2} + \\ &+ \mu^{2}\left(\frac{v+h}{\sqrt{2}}\right)^{2} - \lambda\left(\frac{v+h}{\sqrt{2}}\right)^{4}. \qquad (2.24)\end{aligned}$$

Evaluating this equation expressions can be found for the kinetic terms of the Higgs field, interaction between the Higgs and the gauge boson field and mass terms for the $W^{\pm}$ and Z bosons corresponding to the ground state vacuum expectation value of the Higgs. In particular the very interesting results are the masses of the gauge bosons,

$$m_W = \frac{1}{2}gv \qquad (2.25)$$

$$m_Z = \frac{M_W}{\cos\theta_W}, \qquad (2.26)$$

where θ_W is the Weinberg's angle. The correct prediction of the relation between the masses of the electroweak gauge bosons was an important success of the Higgs theory. The vacuum expectation value, v, can also be calculated from the equations above, but the theory does not yield information on the Higgs mass. λ remains a free parameter.

The fermion masses can also be obtained from interactions with the Higgs field by a Yukawa coupling. The Lagrangian with an explicit spinor mass term, $m\bar{\psi}\psi$, would not be invariant under gauge transformation because it would contain a mixture of $SU(2)$ doublet and singlet fields which have different transformation properties. A solution is offered by the Higgs mechanism,

$$\mathcal{L}_{Yukawa} = -g\left[\bar{\psi_L}\Phi\psi_R + \bar{\psi_R}\Phi^{\dagger}\psi_L\right]. \qquad (2.27)$$

The problem in this case is that the coupling, g, is completely arbitrary. With the choice $m_f = gv/2$ the coupling of fermions to Higgs takes the form

$$- m_f \bar{f} f \frac{h}{v} \ . \tag{2.28}$$

High energy colliders in the past and future decades have been and will be searching for the Higgs boson to confirm or reject this simple and elegant mechanism.

Quantum Chromodynamics (QCD) describes the interaction of quarks and their mediator eight massless gauge bosons, the gluons. Because of the color degrees of freedom the quarks have a color quantum number, while the gluons mediate the colors between the quarks. Historically six massive quarks have been found, they are named up, down, charm, strange, top and bottom. The quarks and gluons have color charges, in addition to their fractional electromagnetic charges.

The Lagrangian of the system of quarks can be constructed, similarly to QED, from fermion fields. But this time we must label the color degrees of freedom of the fermions,

$$\mathcal{L} = \bar{q}_j (i\gamma^\mu \partial_\mu - m) q_j. \tag{2.29}$$

We require this time local invariance of the Lagrangian against rotations in $SU(3)$ color space

$$q_j(x) \rightarrow e^{i\alpha_a(x)T_a} q_j(x) \ , \tag{2.30}$$

where T_a are the 8 Gell-Man 3×3 matrices acting on the color space. As before, this transformation will not leave the Lagrangian invariant and the solution is to introduce new gauge fields to resolve the symmetry by means of the covariant derivative

$$D_\mu \equiv \partial_\mu + igT_a G^a_\mu. \tag{2.31}$$

The corresponding transformation property of the gauge fields, G^a_μ is not straightforward, as the $SU(3)$ group is non-abelian

$$G^a_\mu \to G^a_\mu - \frac{1}{g}\partial_\mu \alpha^a - f^a_{bc}\alpha^b G^c_\mu \ , \tag{2.32}$$

where f^{abc} are the real structure constants of the group $SU(3)$ defined by the commutation relation between the T^a group elements

$$[T^a, T^b] = i f^{abc} T^c. \tag{2.33}$$

The invariant gauge field kinetic term has to be constructed from the corresponding field strength tensor of $SU(3)$

$$G^a_{\mu\nu} = \partial^\mu G^a_\nu - \partial^\nu G^a_\mu - g f_{abc} G^b_\mu G^c_\nu, \tag{2.34}$$

leading to the invariant kinetic Lagrangian term

$$\mathcal{L} = -\frac{1}{4} G^a_{\mu\nu} G^{\mu\nu}_a. \tag{2.35}$$

A further property of the quarks is that experimentally a free quark has not been found. They were only found in quark-antiquark bound states and three quark bound states. The consequence of this is that only certain combinations of color quantum numbers can exist in nature in bound states. Using the color notion, there are three colors: red (R), green (G) and blue(B), used to label the color quantum number. Only white combinations have been observed experimentally. The mesons are bound states of color-anticolor pairs, and the baryons are bound states of three quarks each with a different color. In QCD the coupling constant behaves opposite to the coupling in QED. An electric charge probed at smaller and smaller distance scales (i.e. higher and higher energies) will show more and more of its charge, while at larger distance scales it is screened by the polarization of the virtual electron-positron pairs in the vacuum. Therefore the coupling in QED increases with increasing energy scale. In contrast, in QCD the gluon-gluon interaction produces anti-screening: the coupling decreases with increasing energy scale, and in-

creases with increasing distance scale. The first effect is called the asymptotic freedom, the second is called the color confinement. As a consequence at very high energy scattering interactions the quarks are quasi-free because of small coupling, but no quark or gluon can be separated because of the increasing coupling. In fact there are complicated color connections between all the quarks and gluons in QCD processes at high energy colliders. But after the interaction they are confined in colorless hadrons.
The quarks also take part in the weak interaction, forming left handed doublets, the weak processes turn one type of quark into another, in the same way as it turns leptons into neutrinos. There are therefore associated weak quark doublet terms in the full Lagrangian of the Standard Model. Similar to the three lepton doublet families, only three quark doublet families have been confirmed so far

$$\begin{pmatrix} e \\ \nu_e \end{pmatrix}_L \begin{pmatrix} \mu \\ \nu_\mu \end{pmatrix}_L \begin{pmatrix} \tau \\ \nu_\tau \end{pmatrix}_L$$

$$\begin{pmatrix} u \\ d' \end{pmatrix}_L \begin{pmatrix} c \\ s' \end{pmatrix}_L \begin{pmatrix} t \\ b' \end{pmatrix}_L$$

where the prime on the down, strange and bottom quarks indicates that the weak eigenstates (isospin doublets) of the quarks are not the same as the physically observable mass eigenstates (isospin singlets). Therefore a mixing matrix is needed between the left-handed quark isospin doublets and the right-handed quark isospin singlets. The transformation between the one eigenstate and the other is described by a 3×3 unitary matrix, the Cabbibo-Kobayashi-Maskawa (CKM) matrix,

$$\begin{pmatrix} d' \\ s' \\ b' \end{pmatrix} = V_{\mathrm{CKM}} \begin{pmatrix} d \\ s \\ b \end{pmatrix} . \tag{2.36}$$

An important consequence of the mixing is that the CKM matrix elements directly enter into the charged current weak interaction terms between quarks. When an interaction occurs between the up-type (u, c, t) and the down-type (d', s', b') quarks the CKM matrix elements can be identified for each mutual interaction between two quarks as

$$V_{\mathrm{CKM}} = \begin{pmatrix} V_{ud} & V_{us} & V_{ub} \\ V_{cd} & V_{cs} & V_{cb} \\ V_{td} & V_{ts} & V_{tb} \end{pmatrix} = \begin{pmatrix} 0.94718(27) & 0.2255(19) & 0.00393(36) \\ 0.230(11) & 1.04(6) & 0.00412(11) \\ 0.0081(6) & 0.00387(23) & > 0.74 \end{pmatrix} \tag{2.37}$$

where the current experimental values with uncertainties (denoted with a parenthesis after the corresponding last decimal places) or limits (at 95% confidence level) on the magnitude of the matrix elements have been indicated too [1].

Table 2.1 shows the lepton and quark families and some of their properties [1]. The top quark, the heaviest of the third generation of fermions, is very special. Its large mass makes it very peculiar. Here a brief summary is given about the various important features of the top quark in the Standard Model.

1. The existence of the top quark had been predicted before its discovery. After the experimental determination of the isospin quantum number of the left- and right-handed b quarks of $T^3_L(b) = -1/2$ and $T^3_R(b) = 0$ it has been predicted that an isospin doublet partner must exist too [15]. However, no experimental evidence was found for a fourth generation of doublets, neither in the lepton, nor in the quark sector. Assuming SU(2) is an effective low energy theory there must be a special role for the top quark being the last piece in the experimentally found doublets.

2. Considerations from delicate cancellations of possible loop anomalies also suggested that there must be a third generation of quark isospin doublets. The cancellations are complete by adding top quark loops to the possible loop diagrams.

Table 2.1: *Mass, charge, weak isospin and hypercharge quantum numbers of leptons and quarks*

Particle	**Mass [MeV]**	**Q**	$\mathbf{T^3}$	**Y**
ν_e	$< 460 \times 10^{-6}$	0	1/2	-1
e	0.511	± 1	$e_L = -1/2$ $e_R = 0$	-1 -2
ν_μ	< 0.19	0	1/2	-1
μ	105.6	± 1	$\mu_L = -1/2$ $\mu_R = 0$	-1 -2
ν_τ	< 18.2	0	1/2	-1
τ	1776.84	± 1	$\tau_L = -1/2$ $\tau_R = 0$	-1 -2
$up(u)$	1.5 - 3.3	+2/3	$u_L = 1/2$ $u_R = 0$	1/3 4/3
$down(d)$	3.5 - 6.0	$-1/3$	$d_L = -1/2$ $d_R = 0$	1/3 $-2/3$
$charm(c)$	1.27×10^3	+2/3	$c_L = 1/2$ $c_R = 0$	1/3 4/3
$strange(s)$	70 - 130	$-1/3$	$s_L = -1/2$ $s_R = 0$	1/3 $-2/3$
$top(t)$	172×10^3	+2/3	$t_L = 1/2$ $t_R = 0$	1/3 4/3
$bottom(b)$	4.2×10^3	$-1/3$	$b_L = -1/2$ $b_R = 0$	1/3 $-2/3$

3. The large mass of the top quark puts it well into the regime of perturbation theory in QCD because the running strong coupling, α_s, decreases with increasing energy scale. Therefore comparison of theoretical predictions and experimental measurements of top quark production serves as an excellent test of perturbative QCD.

4. The mass also couples the top quark strongly to the Standard Model Higgs boson and therefore precise measurements of the top quark properties put constraints on the Higgs properties which is believed to subsequently lead to a better understanding of mechanism of spontaneous symmetry breaking.

5. Extraction of the CKM matrix element V_{tb} is possible from the measurement of top quark production.

6. Last but not least there are natural expectations for the production of top quarks from the decays of even more massive exotic particles at the TeV scale. The decay branching ratios favor the top as a final state in a lot of cases.

These points illustrate that the top quark plays a fundamental role in the theory of particle physics. Experimental observation of top quark pair production is, however, not straightforward because the top quark is a heavy object therefore the probability of producing it, or even two of them, is much smaller than elastic proton-proton scattering and inelastic production of light quarks, or even the production of W or Z bosons. Finding a top quark pair signal among these various background processes in proton-proton collision data needs an understanding of the various patterns in the properties of both the production and decay mechanism of the signal and background processes.

2.2 Simulation of hard scattering processes at hadron colliders

Hard subprocess

Scattering of particles can be used to study their properties. The particles are represented by relativistic quantum fields in order to be able to construct creation and annihilation of particles in the theory. Experimentally particle beams are prepared far away from each other with no interaction between them. Then the experiment lets them collide head on with each other and interact. Finally the remnants of the initial beams are separated again and the final-state particles of the primary process are scattered away from the initial beams where detectors collect their signals. Such a scattering process can be described as a probability amplitude from a particular initial state $\mid i\rangle$ to a particular final state $\mid f\rangle$ as

$$\langle f \mid S \mid i\rangle \equiv S_{fi} \tag{2.38}$$

where the matrix, S_{fi}, must fulfill the condition that for all final states the total probability amplitude must be unity. In the Dyson-Wick formalism [5] the S matrix can be expanded as a perturbation series

$$S = \sum_{n=0}^{\infty} S^{(n)} \equiv \sum_{n=0}^{\infty} \frac{-i^n}{n!} \int \dots \int d^4x_1 \dots d^4x_n \mathcal{T}\{\mathcal{H}_I(x_1)\dots\mathcal{H}_I(x_n)\}, \tag{2.39}$$

where $\mathcal{H}_I$ is the interaction Hamiltonian density describing the particular interaction between the fermion and gauge fields, $\mathcal{T}$ is a normal product of the quantized field operators in the Hamiltonian density, while the integrals are taken over all space-time. For $n = 0$ the $S^{(0)}$ matrix is the free field *propagator*. For $n = 1$ the S matrix gives a *vertex* contribution, e.g. in QED $S^{(1)} = ie \int d^4x(\bar{\psi}\gamma^\mu A_\mu \psi)_x$. For a $2 \rightarrow 2$ scattering process one has $S^{(2)}$, etc. An $S^{(2)}$ order is called *leading order* or *tree-level* process, while higher orders are called *corrections*. One can identify always kinematic and dynamic terms when calculating the transition probability amplitudes and the kinematic terms are usually called *phase space factors* while the dynamic terms are called *Feynman rules*. The latter can be derived for any kind of fields and interactions in the Hamiltonian or Lagrangian density of a given model. A calculation is usually carried out at a given order in perturbation theory. The differential cross section at that given order, n, is then calculated as the transition rate into a group of final states for one scattering center and unit incident flux, while the differential decay rate of a given particle is calculated similarly but with only a single initial particle. It is the task of the particular quantum field theoretical model in question to show that the cross section can be calculated as a converging perturbation series up to a given order. The convergence is typically considered in terms of the magnitude of the coupling constants. QCD in particular is such that the coupling constant gets smaller at larger energies, therefore it is possible to apply perturbation calculation for the hard scattering process. At orders higher than leading order divergent integrals show up because of self-interaction, loops and soft and collinear processes. To regularize the calculation typically cut-off scales are introduced into the theory to account for the fact that the theoretical approximation is not correct at any arbitrary scale. The choice of a particular scale is where the perturbative approach meets the non-perturbative regime.

Parton density functions

Protons are composite particles, they are made of quarks and gluons, or in general partons. Therefore any kind of production process at the LHC proton-proton collider will basically have partons in the initial state. The partons within the proton have momentum and the distribution of parton momentum fractions within the proton is important for understanding the different initial states of the proton which contribute to the top pair production mechanism. It is believed that the total cross section of hard scattering processes in a hadron collider can be approximated as a convolution of a hard scattering cross section that can be calculated perturbatively [16] and parton distribution functions (PDFs) [17], which are in a non-perturbative QCD regime. This is called *factorization*. The proton structure is described in the PDFs. The PDF, $f_a(x, \mu_F)$, gives the probability that a parton with flavor a has a momentum fraction x in the proton at an energy scale μ_F. However, there is always a normalization scale used in the definition because the relative fraction of partons depends on the energy scale at which one probes the proton. There is a renormalization group equation that gives the μ_F dependence

$$\frac{d}{d\ln\mu_F} f_a(x, \mu_F) = \sum_b \int_x^1 \frac{d\xi}{\xi} P_{ab}(x/\xi, \alpha_s(\mu_F)) f_b(\xi, \mu_F). \tag{2.40}$$

This is known as the DGLAP (Dokshitzer-Gribov-Lipatov-Altarelli-Parisi) equation [18], [19], [20], [21]. The interpretation of this evolution with μ_F is as follows. When the renormalization scale μ_F changes, the probability to find a parton with momentum fraction x and flavor a changes. This change in probability is related to finding such a parton with large momentum. The way to get this parton with large momentum is for a parton carrying momentum fraction ξ and much smaller momentum to split into partons carrying large transverse momenta, including the parton in question. This splitting probability, integrated over the transverse momentum ranges, is the so called P_{ab} kernel function. In principle the PDFs can be calculated from lattice QCD methods. However, currently they are parametrized and measured using experimental methods at a scale μ_0 and the scale dependence is evaluated using the DGLAP equation [22], [23].

Parton shower

Experimentally, in the final state of hard proton-proton collision well collimated spray of hadrons are detected, so called *jets*. The reason for the production of jets is that after the hard subprocess, which can be approximated with perturbative calculations in QCD, partons enter into the regime of non-perturbative QCD where the coupling is stronger and produce emissions of radiation in form of gluons and quarks. These emitted additional partons are flying also into the same direction as the initial parton and are highly boosted. Such emissions are highly enhanced for soft and collinear radiations. Monte Carlo methods, so-called *parton shower* Monte Carlos simulations [24] [25], are used to simulate evolution processes of such emissions, leading to a tree-like structure, both in the initial and in the final state of the hadron collisions. At leading order the parton splitting probabilities can be used to distribute the energy fractions of the partons to split. But higher order corrections are also important because of the enhanced contribution from soft and collinear emissions.

In general it is difficult to unambiguously separate the components of the picture which belong to the hard subprocess (to be calculated in the matrix element) from those developing during the parton shower evolution. A given $(n+1)$-jet event can be obtained in two ways: from the parton shower evolution of an appropriate $(n+1)$-parton final state, or from an n-parton configuration where hard, large-angle emission during its evolution leads to the extra jet. Therefore an additional important step to get physical results is to correctly match the partons in the hard subprocess to the parton showers in the splitting evolution simulations. During the matching procedure scale parameters are used to regulate the results. Therefore jet production rates can be sensitive to matrix element-parton shower matching parameters [26].

Hadronization

The colored partons after the showering form color singlet hadrons. There are two main ways to simulate this process: the cluster model [24] and the string model [25]. The assumption is that a parton again splits into quark-antiquark pairs and forms mesons. What need to be given is the relative probabilities to produce the various possible quark-antiquark pairs with different flavors and the relative probabilities that a given quark pair combination forms a specific meson. To produce barions similar relative probabilites are needed to combine an antiquark and a di-quark state to a three-quark state. After creating the groups of such combinations, depending on the flavor and mass of the combined system, there can be special corrections.

In hadron-hadron collisions there are also “spectator” partons in the incoming hadrons. The *underlying event* is the simulation of the soft collision between these spectators from the initial state hadrons. The presence of underlying event can affect the experimental reconstruction of the final state of the hard subprocess.

2.3 Top quark pair production and decay

From kinematics it is obvious that to produce two massive quarks at rest there has to be at least enough energy

$$\hat{s} \geq (p_i + p_j)^2 = 2m_t^2 + 2E_t^2 = 4m_t^2, \tag{2.41}$$

where p_i and p_j denote the four momenta of the inital partons and t denotes top. However, the total partonic center of mass energy is $\hat{s} = x_i x_j s$. Assuming $x_i \approx x_j$ the typical values of the parton momentum densities can be predicted by considering x at threshold top pair production, $x \approx 2m_t/\sqrt{s}$ [1], as shown in Fig 2.1. For $\sqrt{s} = 7$ TeV one gets $x \approx 0.05$. This can be interpreted using the parton momentum densities and the conclusion is that at the LHC energies top quark pair production is basically dominated by gluon-gluon fusion processes.

2.3.1 Top quark pair production cross section

The total cross section for top quark pair production initiated by a proton-proton collision at a center of mass energy $\sqrt{s}$ can therefore be calculated as

$$\sigma^{t\bar{t}}(\sqrt{s}, m_t) = \sum_{i,j=q,\bar{q},g} \int dx_i dx_j f_i(x_i, \mu^2) f_j(x_j, \mu^2) \hat{\sigma}^{i,j\rightarrow t\bar{t}}(\rho, m_t^2, x_i, x_j, \alpha_s(\mu^2), \mu^2) \tag{2.42}$$

where $f_{i,j}(x_{i,j}, \mu^2)$ are the parton distribution functions of the parton i or j in the protons evaluated at energy scale μ^2, the summation indices i, j run

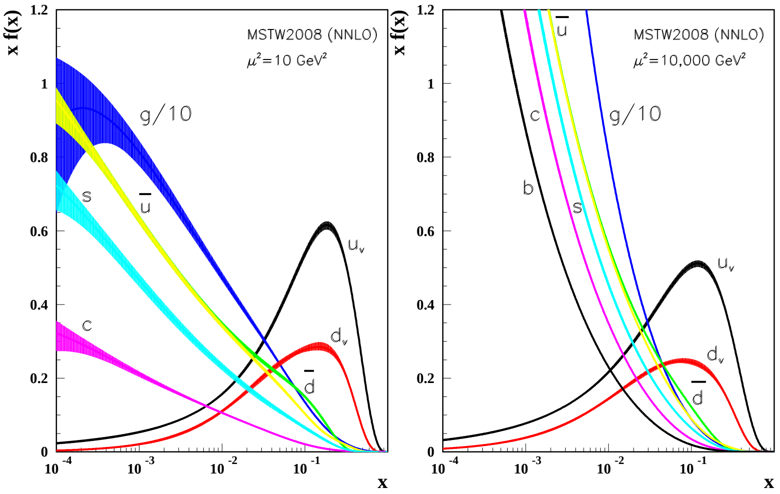

Figure 2.1: *The quark, antiquark and gluon momentum densities in the proton as a function of the longitudinal proton momentum fraction x at $\mu^2 = 10$ GeV^2 (left) and at $\mu^2 = 10000$ GeV^2 (right) from the MSTW2008 parametrization.*

over all $q\bar{q}$, gg, qg and $\bar{q}g$ initial states, $\hat{\sigma}^{i,j\to t\bar{t}}$ is the partonic cross section of the hard scattering process, $\rho = 4m_t^2/\hat{s}$, m_t is the mass of the top quark and $\hat{s} = x_i x_j s$ is the partonic center-of-mass energy squared.

The hard scattering process of top quark pair production is contained in $\hat{\sigma}^{i,j\to t\bar{t}}$. This is the parton level cross section for pair production from initial partons i and j. The partonic cross section can be calculated in QCD using perturbation theory. The leading order (LO) Feynman diagrams contributing to the top pair production are shown in Fig 2.2, from where, following the arguments above, the gluon-gluon fusion processes give the main contribution. At next-to-leading order (NLO) in QCD perturbation theory there are real and virtual corrections to the LO processes. Virtual correction means adding single loop and vertex corrections to the LO graphs while real correction means to add, either in the initial or final state, a real emission of gluons or quarks. Corrections can be added to the LO Feynman diagrams up to a fixed order and the cross section can be evaluated at this level. In perturbative calculations, however, there are certain higher order corrections which give rather large enhancements to the cross section: these are soft

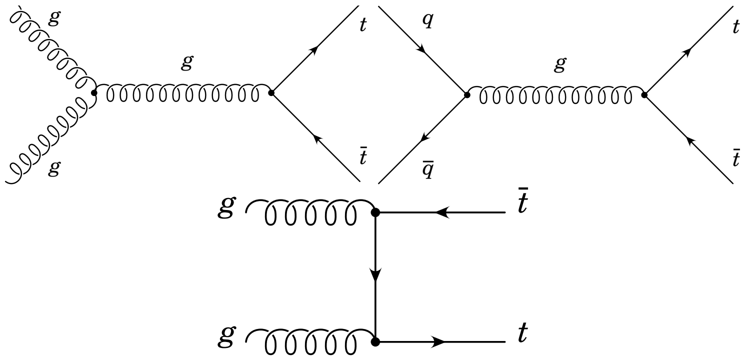

Figure 2.2: *The leading order Feynman diagrams contributing to top quark pair production at LHC.*

and collinear emissions of partons. In fact, it turns out that a certain part of these corrections can be summed up to all orders in perturbation theory. These kind of corrections are called leading logarithm (LL), and next-to-leading-logarithm (NLL), and next-to-next-to-leading-logarithm (NNLL), etc. corrections because they can be factorized into logarithmic terms in the perturbation series. The recent theoretical calculations at NLO level [27] or at NLO+NNLL [28] level as a function of the proton-proton collision center of mass energy are shown on Fig 2.3. For the latter case the renormalization and factorization scale uncertainty is also shown with shaded areas.

2.3.2 Top quark decays

In the top-quark decay the branching ratio is governed by the V_{tb} CKM matrix element. The decay width of the top quark is expected to be dominated by the two-body channel $t \to Wb$. The approximate decay width in the Standard Model for the top quark is [29],

$$\Gamma_t \approx \frac{G_F m_t^3}{8\pi\sqrt{2}} \left(1 - \frac{M_W^2}{m_t^2}\right)^2 \left(1 + 2\frac{M_W^2}{m_t^2}\right) \left[1 - \frac{2\alpha_s}{3\pi}\left(\frac{2\pi^2}{3} - \frac{5}{2}\right)\right], \tag{2.43}$$

resulting in $1.0 - 1.5$ GeV depending on the top quark mass. This gives an extremely short lifetime for the top quark of $\tau \approx 0.5 \times 10^{-24} s$. Therefore

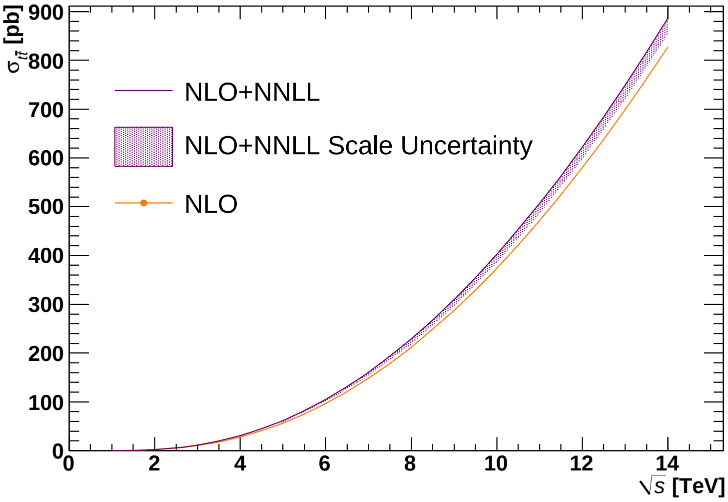

Figure 2.3: *QCD NLO and NLO+NNLL predictions for the top quark pair production cross section at the TeV energies of proton-proton colliders.*

Table 2.2: *Branching fractions (BR) of the different $t\bar{t}$ decay channels at Born level and the experimental value [1].*

Decay mode	Born level BR	PDG value
$t\bar{t} \rightarrow q\bar{q}'bq''\bar{q}'''\bar{b}$	36/81	46.2 %
$t\bar{t} \rightarrow q\bar{q}'bl\bar{\nu}_l\bar{b} + \bar{l}\nu_l bq\bar{q}'\bar{b}$	36/81	43.5 %
$t\bar{t} \rightarrow \bar{l}\nu_l bl'\bar{\nu}_{l'}\bar{b}$	9/81	10.3 %

the top quark is expected to decay before forming top flavored bound states. The leading order (LO) Feynman diagrams for the top pair decay are shown in Fig 2.4. The decay modes are classified according to the final states of the two W decays. Table 2.2 shows the branching ratios of the top quark pair decay. The highest branching ratio is when both W bosons decay to quarks (all hadronic channel). In this channel four jets form from the W decays and there are two b quark jets from the top decays. Experimentally however, it is rather the dilepton and the lepton+jets channels which are favored, because in the all-hadronic channel the instrumental multiparton scattering during proton-proton collisions produces a huge background. In the dilepton

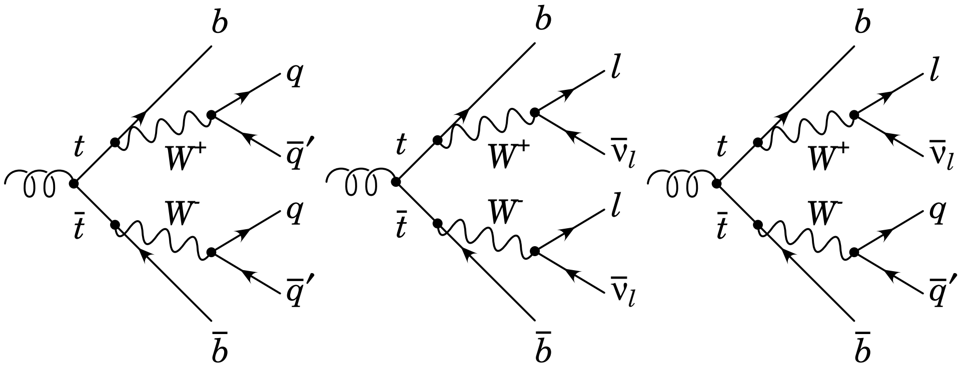

Figure 2.4: *Feynman diagrams illustrating at LO the three decay modes of the top quark pair signal: left: all hadronic channel, middle: dilepton channel, right: lepton+jets channel.*

channel, each of the W bosons decay to a lepton and a neutrino with the presence of the two b quarks. The dilepton channel is favored because the two isolated leptons with high transverse momentum produce a clean signal, and the significant amount of missing transverse energy from the neutrinos also discriminates against instrumental background processes. Additionally the two b quarks hadronize to two jets which can be tagged by b-tagging discrimination techniques. Athough the dilepton channel produces a rather clean signal the decay branching fraction is the smallest, only $\sim$ 10%. The channel with the second highest branching fraction, 43.5%, is the lepton+jets channel. It produces several signatures which are useful for discrimination. The following patterns are expected to be produced by this channel:

- a single, isolated lepton with high transverse momentum,
- large transverse missing energy,
- the presence of at least 4 jets from the W decay and the two top decays.

Experimentally the single, isolated, high transverse momentum lepton can be efficiently triggered. The requirements of high transverse missing energy and the presence of at least four jets can be used to discriminate against background processes. In particular in the analysis the jet multiplicity is used as the main discriminator. Because of these reasons this analysis focuses on the lepton+jets channel.

2.4 Background processes for top quark pair signal

Cross sections (in nanobarns = $10^{-33}\mathrm{cm}^2$) and event rates of the main Standard Model processes are shown in Fig 2.5 as a function of the center-of-mass energy of the colliding protons or protons and antiprotons. The step at $\sqrt{s} = 4$ TeV marks the transitions from the Tevatron $p\bar{p}$ collider energies to the LHC pp collider energies. The most important conclusion from the plot is that the b quark and jet production rates are at least four orders of magnitude larger and the W boson production rate is at least two orders of magnitude larger than that of the top quark production. In general the jet production is a dangerous background because it can create leptons (so-called non-prompt leptons) from the decays of kaons and pions which are usually present in jets with large fractions. W bosons decaying to a single isolated lepton and to a neutrino, however, produce patterns very similar to the lepton+jets channel of the top quark pair signal. W bosons can also be produced along with additional partons in the hard QCD subprocess with partons populating high jet multiplicity bins too. Z production rate is also large but the Z decays typically to two isolated leptons and produces low missing transverse energy. Therefore the probability of faking single isolated leptons is suppressed compared to the QCD multiparton production rate and the high missing transverse energy requirement also suppresses such events rather well. Therefore the main backgrounds for the lepton+jets channel of the top quark pair signal are W+jets and plain QCD multijet production. There are also smaller background contributions expected from processes with tau final states producing leptons and neutrinos and therefore missing transverse energy. W bosons, Z bosons and top quarks subsequently decaying to W bosons can also produce tau leptons in their final states. Table 2.3 summarizes the various processes expected to contribute as a background for

Table 2.3: *Processes expected to contribute as background for top quark pair signal in the lepton+jets final state, indicating their main signatures.*

QCD multiparton	Non-prompt and fake lepton production, multijet
W→ $l\nu$ + jets	Single lepton, tau lepton, neutrino, multijet
W→ b jets, Z→ b jets	b-jets with high momentum
Z→ ll + jets	Single lepton, tau lepton, multijet
WW, WZ, ZZ	Single lepton, neutrino

the top quark pair signal in the lepton+jets channel. The main signatures of the processes are also indicated.
The estimation of the contributions from the various background processes to top quark pair signal will be discussed in the Chapter 5.

2.5 Monte Carlo simulation of signal and background events

In this section a brief summary is given about the Monte Carlo event generator programs used in this thesis. For more details about the generator settings see [30].

2.5.1 Simulation of signal events

Top quark pair and single top production have been simulated using the Monte Carlo generator MC@NLO [27]. The hard process of $t\bar{t}$ production is calculated in QCD at next-to-leading order, so that real and virtual corrections are included at the matrix element level. The parton density function CTEQ6M [22] is used. The parton showering, the fragmentation and hadronisation are simulated using HERWIG [24] and the underlying event simulation was done by the program Jimmy [31].

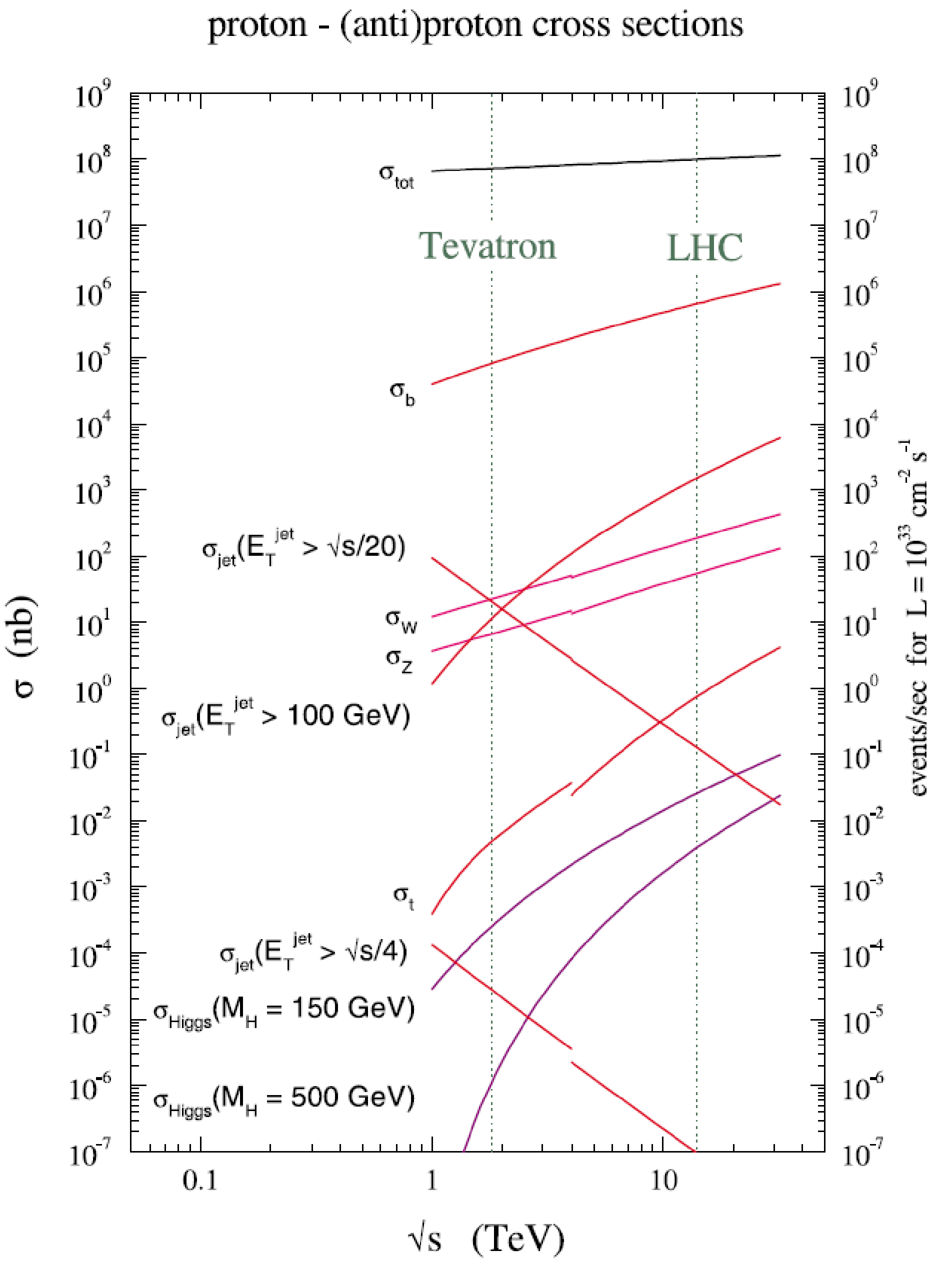

Figure 2.5: *QCD predictions for hard scattering cross sections and event rates at the Tevatron and the LHC at nominal luminosity of* $L = 10^{33}$ cm^{-2} s^{-1}*. The step at* $\sqrt{s} = 4$ *TeV marks the transition from the Tevatron* $p\bar{p}$ *collider to the LHC* pp *collider.*

2.5.2 Simulation of W+jets and Z+jets events

For the production of $W+$ jets and Z+jets the ALPGEN version 2.13 [32] generator is used with HERWIG for the simulation of the parton showering, fragmentation and the hadronisation and Jimmy for the underlying event. For the parton density functions, the CTEQ6L1PDF [22] is used. In ALPGEN, the MLM [33] algorithm has been used to match the parton shower simulation to the matrix element calculations.

2.5.3 Simulation of background events

For the simulation of di-boson production (WW, ZZ, WZ) the HERWIG generator was used.

2.5.4 Monte Carlo cross sections

The cross sections used to normalize the Monte Carlo samples are summarized in the Appendix C.

Chapter 3

Overview of the ATLAS experiment

3.1 The Large Hadron Collider

The Large Hadron Collider (LHC) is a circular proton-proton collider at CERN, Geneva. A schematic view of the CERN accelerator complex is shown on Fig 3.1. The machine has been designed to produce 14 TeV collisions with 100 fb^{-1} integrated luminosity of data per year at the design luminosity of 10^{34} $\mathrm{cm}^{-2}\mathrm{s}^{-1}$. However, in the initial phase the LHC operates at a lower luminosity and at a center-of-mass energy of 7 TeV. The LHC beam pipe has a circumference of a 27 km and the two proton beams, circulating in opposite directions in the same cryostat, are brought together at four points for collisions. The LHC tunnel houses super-conducting bending dipole magnets producing an 8.3 T field needed to keep the particles in orbit. The operating temperature of the magnets is 1.9 K cooled by liquid helium. The protons are accelerated by radio-frequency (RF) cavities.

The protons are created by an ion source which injects them into a RF cavity which accelerates them to 750 KeV. After this, they are transmitted to the proton Linear Accelerator (LINAC) to reach energies of 50 MeV. The Proton Synchrotron Booster (PSB) increases the energy up to 1.4 GeV and sends

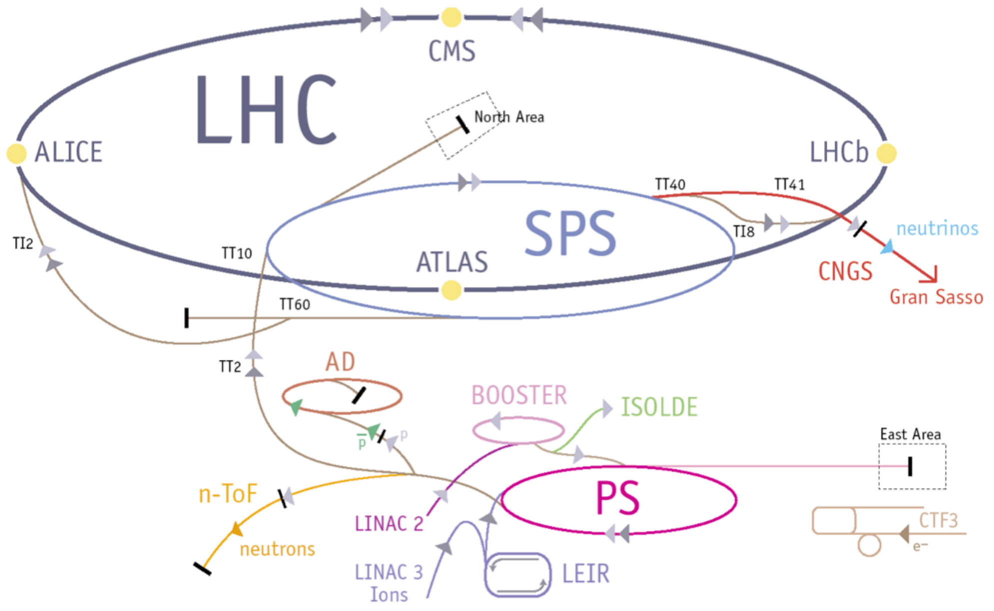

Figure 3.1: *Schematic view of the CERN accelerator comlex.*

the protons to the Proton Synchrotron (PS). The synchrotron increases the energy of the protons further up to 25 GeV. The next step of acceleration is the Super Proton Synchrotron (SPS) which brings the energy to 450 GeV. The proton bunches at 450 GeV are then injected into each LHC ring at a rate such that the time between bunch crossings at the collision points is 25 ns.

The number of events per second produced in the LHC collisions is given by

$$N = L\sigma$$

where L is the machine luminosity and σ is the cross section of the relevant processes. The machine luminosity depends on the beam parameters

$$L = \frac{N_{\mathrm{b}}^2 n_{\mathrm{b}} f_{\mathrm{rev}} \gamma_r}{4\pi\epsilon_n\beta^*}F,\ F = 1/\sqrt{1+\left(\frac{\theta_c\sigma_z}{2\sigma^*}\right)^2}$$

Table 3.1: *LHC nominal parameters*

Parameter [unit]	Nominal
Beam energy [GeV]	7000
Revolution frequency [kHz]	11.245
Relativistic γ_r	7461
No. p^+ per bunch, N_b [10^{11}]	1.5
No. of bunches, n_b	2808
Bunch spacing [ns]	25
Beta at IP β^* [m]	0.55
Full crossing angle, θ_c [μrad]	285
Ratio $\theta_c\sigma_z/(2\sigma^*)$	0.64
Transverse normalized emittance, ϵ_n [μm rad]	3.75
RMS bunch length [cm]	7.55
RMS transverse beam size at IP [μm]	16.7

where N_b is the number of protons per bunch, n_b is the number of bunches per beam, f_rev is the revolution frequency, γ_r is the relativistic gamma factor, ϵ_n is the normalized transverse beam emittance, β^* is the beta function at the collision point and $F(\theta_c, \sigma_z, \sigma^*)$ is a geometric factor due to the crossing angle at the interaction point. The crossing angle, θ_c, introduces the geometric factor F by which the luminosity is reduced, σ^* and σ_z being the transverse and the longitudinal RMS beam size at the interaction point, respectively. Some nominal LHC parameters are summarized in Table 3.1.

3.2 The ATLAS detector

The ATLAS (A Toroidal Lhc ApparatuS) detector [4] is a multi-purpose particle detector and has been built around one of the bunch-crossing collision points of the LHC. ATLAS has been designed to trigger on interesting events in the LHC bunch crossings and subsequently detect all particles emerging from the triggered collisions. An overview of the ATLAS detector system is shown in Fig 3.2. The overall structure of ATLAS is driven by the eight-fold azimuthal symmetry of its three large superconducting toroids (one barrel and two end-caps) which is completed by a superconducting solenoid. Going from inside out there is an inner detector providing pattern recognition, vertex finding and momentum measurements. It is made of silicon pixels and strips, and a straw-tube tracking detector capable of generating and detecting transition radiation. The inner detector sits in a 2T solenoidal field. The solenoid is surrounded by a high granularity liquid-argon (LAr) electromagnetic calorimeter and the hadronic calorimeter which in the barrel region uses scintillator-tile detectors while in the forward region uses LAr technology. The muon spectrometer is the outermost detector built from tracking chambers.

At ATLAS a standard coordinate system is used. The beam direction defines the $z-$ axis. The $x-y$ transverse plane is perpendicular to the beam direction. The azimuthal angle, ϕ, is measure around the beam axis, and the polar angle, θ, is measured from the beam axis. The pseudorapidity is defined as $\eta \equiv -\ln(\tan(\theta/2))$. Distance between physics objects is usually measured in the $\eta-\phi$ space as $dR = \sqrt{(\Delta\eta)^2 + (\Delta\phi)^2}$.

In the rest of this chapter the details of each of these sub-detector systems are described along with the trigger and data acquisition system and the measurement of luminosity in ATLAS.

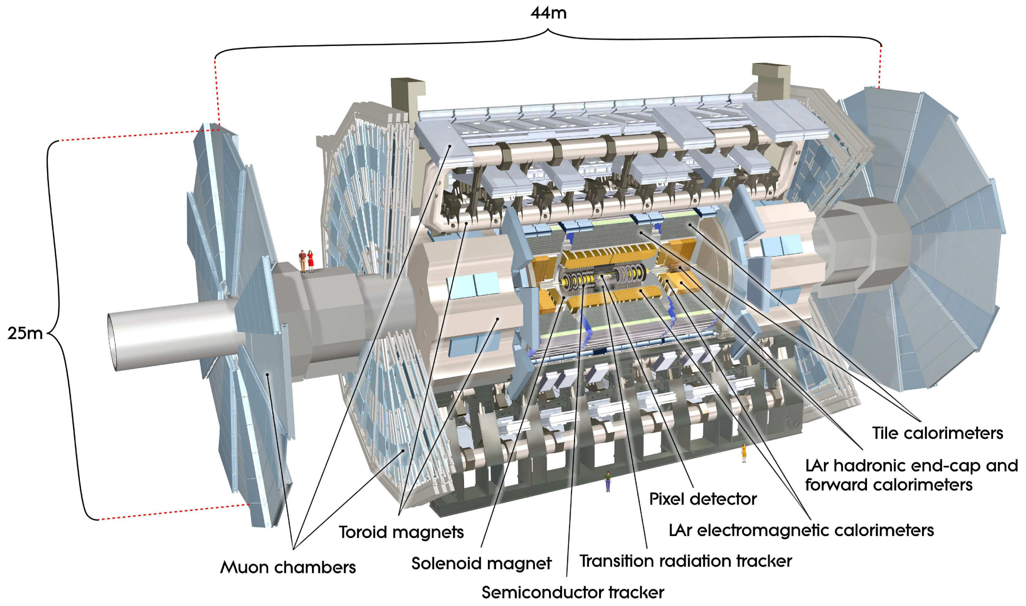

Figure 3.2: *The ATLAS detector.*

3.2.1 Inner detector

Fig 3.3 shows an overall view of the ATLAS Inner Detector (ID). The ID is contained in a cylinder of length 5.5 m and radius 1.15 m, in a solenoid magnetic field of 2 T. It contains three sub-detectors: the silicon pixel detector, the Semi Conductor Tracker (SCT) micro-strip detector and the Transition Radiation Tracker (TRT) made of straw tubes. Each detector has barrel and end-cap parts. A view of a quarter of the inner detector is shown on Fig 3.4. The precision tracking detectors (pixels and SCT) cover the region $|\eta| < 2.5$. In the barrel region, they are arranged in concentric cylinders around the beam axis while in the end-cap regions they are located on disks perpendicular to the beam axis.

Pixel detector

The pixel layers are segmented in $R - \phi$ and z. The first layer of the pixel system, the vertexing layer or Layer-0, is at a radius of 51 mm. There are two more pixel barrel layers, Layer-1 and Layer-2. The pixel sensors are 250 μm thick detectors, using oxygenated n-type wafers with readout pixels on the n^+-implanted side of the detector. There are 1744 pixel sensors: the nominal pixel size is 50 x 400 μm^2 and there are 47232 pixels on each sensor. The pixel sensors are mounted on modules. The modules are mounted on the three barrel layers and on the three disks of the two end-caps.

SCT

The 15912 sensors of the SCT each have a thickness of 285 μm. The strips are on 4088 modules. They are mounted on four coaxial cylindrical layers in the barrel region and on nine disks in each end-cap. In the barrel region the SCT uses small-angle (40 mrad) stereo strips to measure both coordinates, with one set of strips in each layer parallel to the beam direction, measuring $R - \phi$. In the end-cap region the detectors have a set of strips running radially and a set of stereo strips at an angle of 40 mrad. The mean pitch of the strips is also approximately 80 μm.

TRT

The TRT straw tubes are drift tubes of 4 mm diameter. The straw (cathode) drift tube consists of an anode wire and operates with a gas mixture chosen to be 70% Xe, 27% CO_2 and 3% O_2. The TRT contains 73 layers of straws in the barrel region and 160 straw planes in the end-cap region. The barrel TRT is structured into cylindrical layers and the end-caps are made into wheels. A view of a quarter of the inner detector is shown on Fig 3.4. Charged tracks with $p_T > 0.5$ GeV and $|\eta| < 2.0$ are expected to traverse 22-36 straws.

The combination of precision trackers at small radii with the TRT at the larger radius gives very robust pattern recognition for charged tracks passing through the detector and high precision in both $R - \phi$ and z coordinates. The straw hits at the outer radius contribute significantly to the momentum

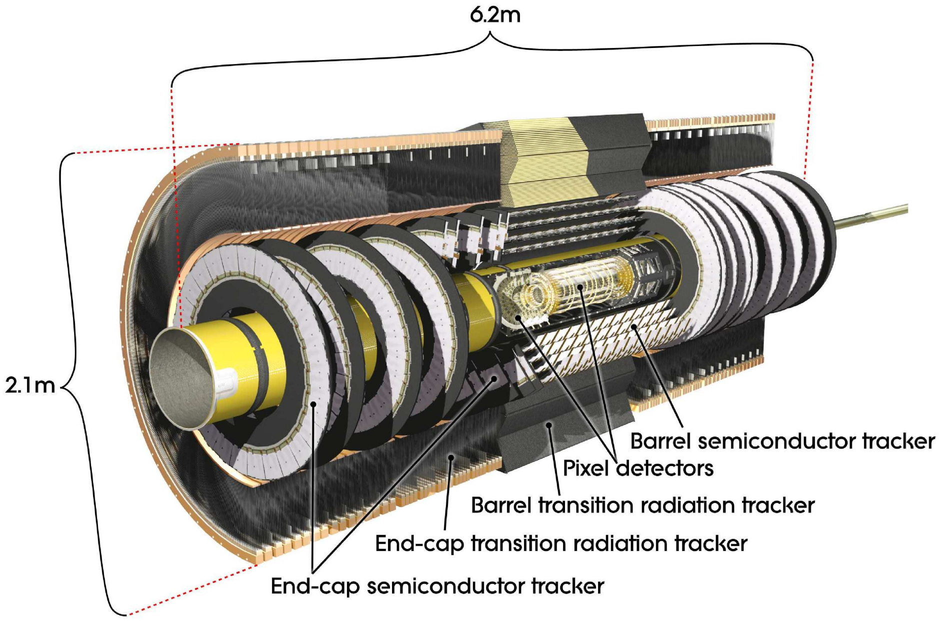

Figure 3.3: *The ATLAS inner detector.*

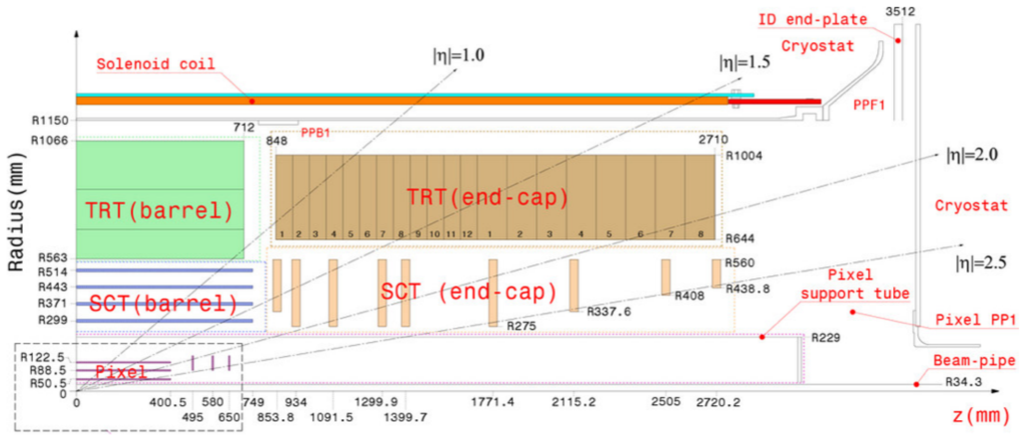

Figure 3.4: *Plan view of a quarter section of the ATLAS inner detector showing the major elements.*

measurement, since the lower precision per point compared to the silicon is compensated by the large number of measurements and longer measured track length.

3.2.2 Calorimetry

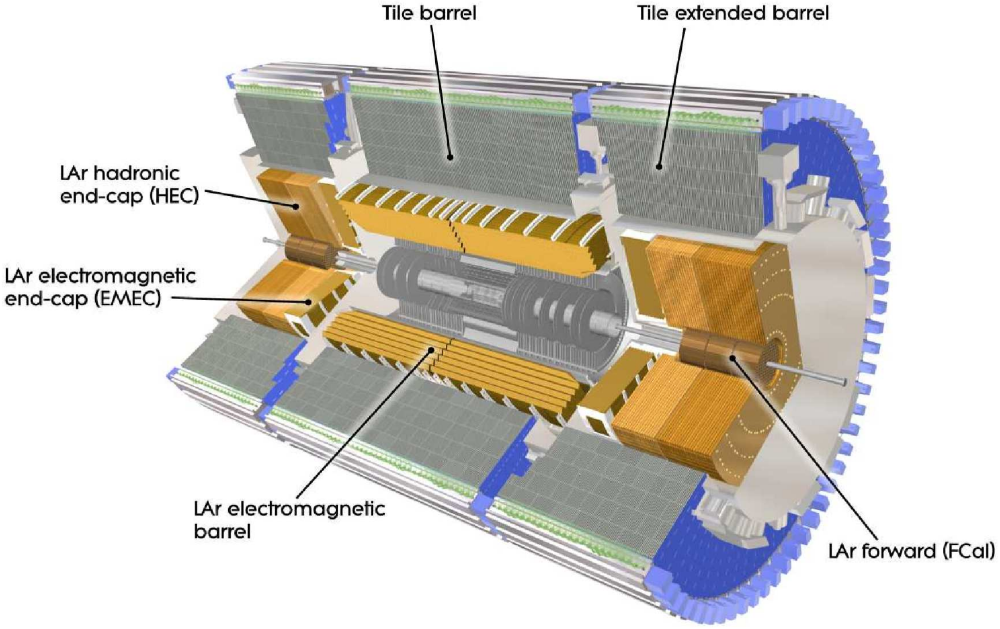

Figure 3.5: *The ATLAS Calorimeters.*

The ATLAS calorimeters surround the inner detector, both in the barrel and in the end-cap regions. Closest to the beam pipe the barrel cryostat houses the barrel electromagnetic calorimeter, while the two end-cap cryostats contain the electromagnetic end-cap calorimeter (EMEC), a hadronic end-cap calorimeter (HEC) behind the EMEC, and a hadronic forward calorimeter (FCAL). All these calorimeters use liquid argon technology (LAr) as active detector material. Outside the cryostat of the LAr components the tile calorimeter resides.

Electromagnetic calorimeters

The electromagnetic barrel and end-cap calorimeters have an accordion geometry, as shown in Fig 3.6 along with the granularities. This geometry provides full coverage in ϕ without any cracks. The absorbers are made of lead plates. The barrel covers the region $0 < |\eta| < 1.475$. The inner surface of the barrel calorimeter is complemented with a liquid-argon presampler over the full η range. It is used mainly to correct for energy lost by electrons and photons upstream of the calorimeter. The EMEC calorimeters consist of two wheels on each side of the barrel. They cover the region $1.375 < |\eta| < 3.2$, however there is a precision region of $1.5 < |\eta| < 2.5$. To improve the energy measurement in the transition region between the barrel and EMEC calorimeters a liquid-argon presampler was implemented in front of the end-cap calorimeter, covering the range $1.5 < |\eta| < 1.8$. The total thickness of the calorimeter is greater than 22 radiation lengths (X_0) in the barrel and greater than 24 X_0 in the end-caps.

The electromagnetic calorimeter is segmented in depth into three layers: the front, middle and back layers. They are also called Layer 1, Layer 2 and Layer 3. The $\Delta\eta$ and $\Delta\phi$ granularities of the front and middle layers are shown in Table 3.2. The granularity of the back layer is $\Delta\eta \times \Delta\phi = 0.050 \times 0.025$.

Hadron calorimeters

The hadronic tile calorimeter is a sampling calorimeter using steel as the absorber and scintillator as the active medium. It is segmented into a central barrel, and into two extended barrels, and is located in the region $|\eta| < 1.7$, residing behind the liquid-argon electromagnetic calorimeter. The cell structure of the scintillator modules form $\Delta\eta \times \Delta\Phi = 0.1 \times 0.1$ cell size in the first two layers and 0.2×0.1 cell size in the last layer of the tile calorimeter. The hadronic end-cap calorimeter (HEC) is a copper/liquid-argon sampling calorimeter which covers the range $1.5 < |\eta| < 3.2$. The HEC shares the same end-cap cryostats with the electromagnetic end-cap and forward calorimeters in the two separate end-cap regions. The readout

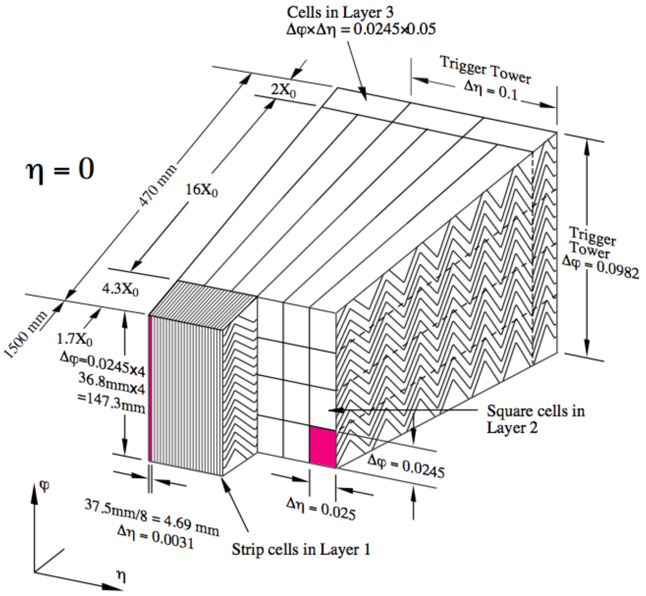

Figure 3.6: *Sketch of an electromagnetic calorimeter barrel module. The granularity in η and Φ of the cells of each of the layers and of the trigger towers is shown.*

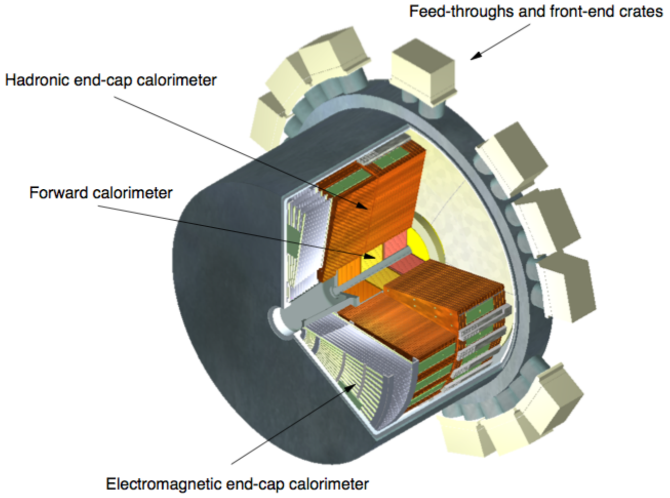

Figure 3.7: *Schematic diagram showing the three FCal modules located in the end-cap cryostat.*

Table 3.2: *The electromagnetic calorimeter granularity ($\Delta\eta \times \Delta\phi$) for the separate layers.*

Detector region	$\lvert\eta\rvert$-range	Layer 1	Layer 2
Barrel	$0 - 1.4$	0.025×0.1	0.025×0.025
	$1.4 - 1.475$	0.025×0.1	0.075×0.025
End-cap	$1.375 - 1.425$	0.05×0.1	0.05×0.025
	$1.425 - 1.5$	0.025×0.1	0.025×0.025
	$1.5 - 1.8$	0.025/8×0.1	0.025×0.025
	$1.8 - 2.0$	0.025/6×0.1	0.025×0.025
	$2.0 - 2.4$	0.025/4×0.1	0.025×0.025
	$2.4 - 2.5$	0.025×0.1	0.025×0.025

cell size of the HEC modules are $\Delta\eta \times \Delta\Phi = 0.1 \times 0.1$ in the region $|\eta| < 2.5$ and 0.2×0.2 for $|\eta| > 2.5$.

The forward calorimeters (FCal) are located in the same cryostats as the end-cap calorimeters and they cover the range $3.1 < |\eta| < 4.9$. The FCal is split into one electromagnetic and two hadronic modules. In the electromagnetic module the absorber is copper, while in the hadronic module it is tungsten. A schematic view of the FCal modules in the end-cap cryostat is shown on Fig 3.7.

3.2.3 Muon spectrometer

An overview plot of the muon spectrometer is show in Fig 3.8 along with the solenoid and the toroid magnet system. The muon spectrometer is instrumented with high-precision tracking and separate fast trigger chambers. Magnetic bending of tracks over the range $|\eta| < 1.4$ is provided by the large barrel toroid, while for the range $1.6 < |\eta| < 2.7$ muon tracks are bent by the two end-cap magnets placed at the ends of the barrel toroid. In the region $1.4 < |\eta| < 1.6$ magnetic bending is provided by a combination of barrel and end-cap fields. The magnet configuration has been designed such that the magnetic field is mostly orthogonal to the muon trajectories. Performance of the magnets is characterized usually in terms of bending power which is the field integral, $\int Bdl$, where B is the field component normal to the muon direction and the integral is computed along an infinite-momentum muon trajectory over the muon-chamber planes. The barrel toroid provides 1.5 to 5.5 Tm of bending power in the pseudorapidity range $0 < |\eta| < 1.4$, while the end-cap toroids provide 1 to 7.5 Tm in the region $1.6 < |\eta| < 2.7$. In the transition regions, $1.4 < |\eta| < 1.6$, the bending power is lower.

The precision-tracking chambers in the barrel region are located between and on the eight coils of the superconducting barrel toroid magnet and in front and behind the end-cap toroids. In the barrel region the muon chambers are arranged in three cylindrical layers around the beam axis. In the end-cap region the chambers form three large wheels, perpendicular to the beam. There are four types of muon chambers.

Monitored Drift Tubes

Over most of the pseudorapidity range the precision measurement of the track coordinates in the bending direction of the magnetic field is provided by Monitored Drift Tubes (MDT) which have high measurement accuracy. The MDTs comprise the 3 layers of precision tracking chambers in the barrel region. The MDT chambers consist of three to eight layers of drift tubes. There are around 16-72 tubes per layer in a chamber. The drift tubes have a diameter of around 30 mm and operate with a mixture of Ar/CO_2 gas at 3 bar. The electrons from ionization are collected by a central tungsten-rhenium wire at a high voltage. The chambers have an average resolution of 35 μm and can provide up to 20 measurements per track both in the barrel and in the end-cap regions.

Cathode Strip Chambers

At large pseudorapidities, $2 < |\eta| < 2.7$, Cathode Strip Chambers (CSC) with high granularity are used due to their high rate capability. They are mounted on the innermost of the end-cap regions' three large wheels, just downstream of the end-cap calorimeter. The CSCs are multi-wire proportional chambers using a similar Ar/CO_2 gas mixture as the MDT. The cathodes of the CSCs are segmented into strips both perpendicular and parallel to the wires. The CSCs have a 40 μm chamber resolution in the bending direction and 5 mm resolution over ϕ.

RPC and TGC trigger detectors

The trigger system covers the pseudorapidity range of $|\eta| < 2.4$, and provides a very good timing resolution of 1.5 to 4 ns to trigger on muons. There are three trigger chamber layers mounted together with the precision-tracking chambers, placed on the inner and outer sides of the MDTs and CSCs. In $|\eta| < 1.05$ Resistive Plate Chambers (RPC) are used in the barrel, and for $1.05 < |\eta| < 2.4$ Thin Gap Chambers (TGC) are used in the end-cap regions. The RPCs are gaseous parallel electrode-plate detectors. Two resistive plates are kept parallel to each other at a distance of 2 mm by insulating spacers. The electric field between the plates allows avalanches to form along the ionizing tracks. TGCs operate on the same principle as multi-wire proportional chambers with the characteristic that the wire to cathode distance is smaller than the wire-to-wire distance, and they operate at a high electric field - these two properties leading to very small drift times and therefore very good time resolution. Apart from providing bunch-crossing identification and trigger thresholds, the muon trigger detectors measure the muon coordinate in the direction orthogonal to that determined by the precision tracking chambers.

3.2.4 Trigger and data aquisition

At design luminosity and with a bunch-crossing interval of 25 ns at the LHC the frequency of collisions is expected to happen at a rate of 40 MHz. The trigger system is responsible for reducing this high rate by selecting only interesting events. The ATLAS trigger is made of three levels of event se-

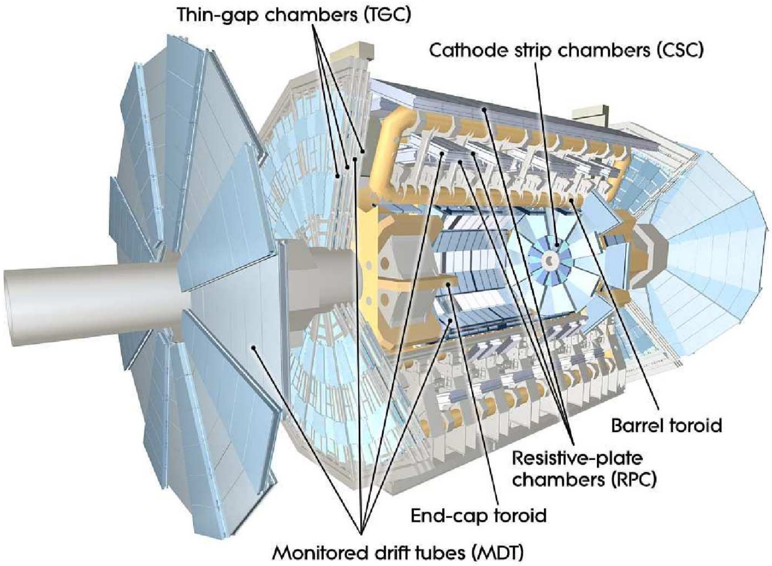

Figure 3.8: *The ATLAS Muon spectrometer.*

lection: level 1 (L1), level 2 (L2), and a final event filter level (EF). The L1 trigger level is made completely of electronics, while the L2 and EF triggers are computer-based implementations. Each trigger level refines the decisions of the previous trigger level. In parallel the data acquisition system buffers the event data from the detector-specific readout electronics at the L1 trigger accept rate. A simplified view of the ATLAS trigger and data acquisition is shown on Fig 3.9.

The L1 trigger consists of searches for signatures of muons, electrons/photons, τ-leptons decaying into hadrons, and events with large missing transverse energy (E_T^{miss}) and large total transverse energy. It performs the initial event selection based on information from the calorimeters and the muon detectors. In particular the L1 muon triggers are the RPC and TGC fast detectors, searching for high-p_T muons originating from the interaction region. The L1 trigger uses only a limited amount of the total detector information and makes a decision in around 2.5 μs. During this time information from all the detector channels is stored in pipeline memories. Once an event has been selected by the L1 trigger, all detector channels are read out to readout drivers (RODs) and then into readout buffers (ROBs). The maximum L1 accept

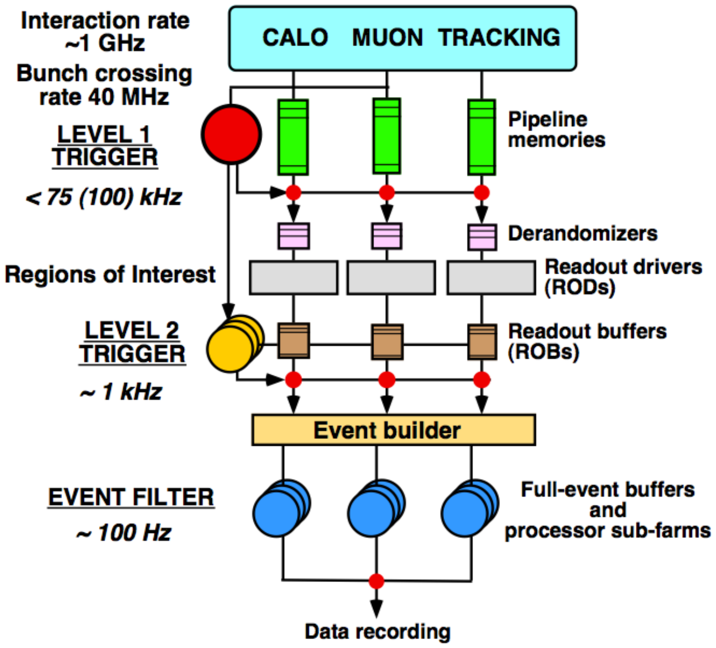

Figure 3.9: *Schematic view of the ATLAS trigger and data acquisition system.*

rate which the detector readout system can handle is 75 kHz. The overall L1 decision is made by the Central Trigger Processor (CTP) which also stores different trigger menus containing trigger items corresponding to different thresholds and signatures. The L1 decision is based only on the multiplicity of the trigger objects, position information from the detectors is not used at this level but only at the L2 level. The L1 accept decision from the CTP is stored for each luminosity block as well. (A luminosity block is the shortest time of interval for which the integrated luminosity can be determined.)

The L2 trigger is seeded by Regions-of-Interest (RoI) information made of the regions of the detector where the L1 trigger has fired on possible interesting object candidates within an event. The trigger at this level starts from the RoIs and applies decisions in a series of steps, each refining existing information by adding data from increasingly more detectors. A list of physics signatures, or so called trigger chains, implemented in the form of selection algorithms (e.g. identifying features from tracks or calorimeter clusters) are used. The L2 trigger reduces the event rate to a level of 3.5 kHz. The event processing time of L2 is approximately 40 ms. All the detector data is stored in the ROBs at this point until the event is accepted or rejected by the L2 trigger. If the event is accepted all data is moved from the ROBs to the Event Filter and the event building process starts.

The EF trigger is based on full offline analysis algorithms further reducing the rate of events to a level at which they can be recorded for subsequent offline analysis. The event rate is reduced at this level to approximately 200 Hz with an average event processing time of 4 seconds. Part of the selection process is the classification of the events into ATLAS physics data streams: electrons, photons, muons, jets, E_T^{miss}, τ leptons and B-physics. Each event is recorded in one or more files according to the stream classification definition. At ATLAS an inclusive streaming procedure has been implemented therefore a particular event could be stored in more than one streams if it fulfills several stream requirements. In this thesis the muon trigger stream data is used for analysis.

3.2.5 Luminosity

In section 3.1 the beam luminosity has been defined for the Large Hadron Collider. ATLAS also monitors and measures the relative and absolute luminosity. In the following we give a list of methods used at ATLAS [34]:

- Beam parameter scans can be used to determine absolute and relative luminosity (van der Meer scans of the beam, or direct determination of the bunch current).
- The optical theorem can be used to relate the total rate of proton-proton interactions to the rate of forward elastic scattering and extract the absolute luminosity. The ALFA (Absolute Luminosity For ATLAS) detector, placed at ± 240 m from the interaction point (IP), is used to measure elastic scattering at small angles. The detector is a scintillating-fibre tracker placed inside a volume (Roman-pot) and is moved in vacuum close to the beam to detect particles at very small scattering angles.
- Physics processes with high rate can also be used to make both absolute and relative measurements. Having a precise knowledge of the W or Z production, and of the parton distribution functions, leptonic final states can be selected to estimate the absolute luminosity.
- The cross section of lepton pair production via two photon fusion can be calculated to a precision of 1%. However the cross section of this process is very small and the background contribution must be well under control.
- The LUCID (LUminosity measurement using Cerenkov Integrating Detector) online relative luminosity monitoring detector is located at ±17 m from the IP. LUCID's main purpose is to detect inelastic pp scattering in the forward direction. The detector has been designed to have sufficient time resolution to identify individual bunch crossings. LUCID measures Cerenkov light emitted by forward scattered particles

entering into Cerenkov tubes. The detector is used for hit counting per tube, using a pulse-height threshold for the counting.

- The Minimum Bias Trigger Scintillator (MBTS) counters consist of scintillators. They are mounted on each side of the IP in front of the LAr end-cap. The relative luminosity is measured by counting the minimum bias trigger rate. The MBTS also provides L1 trigger information.

- The tile calorimeter has a minimum bias monitoring system based on the integrated anode current of the photomultiplier tubes.

- The LAr end-cap calorimeter has the possibility to monitor the high voltage current in the LAr detector and therefore to provide relative luminosity information.

The luminosity is measured and stored for each luminosity block (LB) which is the atomic unit of the data at ATLAS. One LB contains roughly 1 minute of data taking, but this can vary due to run conditions and other operational issues. The central trigger processor of the ATLAS trigger system provides timing information for the beginning and ending time for each LB and for each trigger chain separately. Integrating luminosity over a fraction of data means to get the list of the corresponding luminosity blocks and for each of them substitute the time and other trigger related values, and finally sum up the values in the simplified 'discretized integral formula':

$$L_{tot} = \sum_i \Delta t_i \cdot \mathcal{L}_i \tag{3.1}$$

where L_{tot} is the total integrated luminosity, i in the sum goes over the selected list of LBs, Δt_i is the time length of the ith LB of a given trigger, and finally $\mathcal{L}_i$ is the average luminosity of the ith LB in the data.
The uncertainty on the luminosity estimation is dominated by systematic uncertainties, which are 100% correlated between the luminosity blocks. The

ATLAS Luminosity Working Group's current estimation of the total uncertainty is 11% based on the uncertainties associated with the van de Meer scans [35], [36].

3.2.6 Detector simulation

Simulation of the signals produced in the detector system is an essential tool for analysis. Particles flying through the detector system ionize, excite, scatter and recombine with the detector material, producing so-called signal hits. The hits are recorded through electronic circuits which digitize the analog signals. The simulation of the detector hits is done with the GEANT4 [37] Monte Carlo program which models the interaction of the various particles with the detector material using stochastic methods. During the description of the analysis the phrase *full detector simulation* will be used frequently referring to the procedure outlined above. The full detector simulation of the signals created by a particular event of a Monte Carlo event generator is followed by an object reconstruction step where physics particle candidates are searched for using pattern recognition algorithms. Afterwards object reconstruction algorithms are applied on each such physics particle candidate to correctly identify or reject them. These latter two steps (pattern searching and reconstruction) will be referred to as *full reconstruction* during the further chapters of the thesis. The physics object reconstruction algorithms are detailed in Chapter 4.

Chapter 4

Reconstruction of physics objects

4.1 Tracking

In ATLAS at design LHC luminosity approximately 1000 particles will traverse the inner detector every 25 ns, therefore reconstruction of tracks is a challenging task. However, the very high granularity of the pixel detector and the several TRT and SCT layers make it possible to efficiently reconstruct tracks emerging from the proton-proton collisions, and measure the track parameters with sufficient resolution. Track finding and reconstruction in the inner detector happens in the following way at ATLAS. First there is a pre-processing stage in which the raw data from the pixel and SCT detectors are converted into clusters and the TRT raw timing information is translated into calibrated drift circles. The SCT clusters are transformed into space-points, using a combination of the cluster information from opposite sides of a SCT module. Next is the track finding stage when the tracking reconstruction exploits the high granularity of the pixel and SCT detectors to find prompt tracks originating from the vicinity of the interaction region. First, track seeds are formed from a combination of space-points in the three pixel layers and the first SCT layer. These seeds are then extended throughout the SCT to form track candidates. Next, these candidates are fitted, outlier clusters are removed, ambiguities in the cluster-to-track association are resolved and fake tracks are rejected. This is achieved by applying quality cuts. The selected tracks are then extended into the TRT to associate drift-circle information in a road around the extrapolation and to resolve the left-right ambiguities. Finally, the extended tracks are refitted with the full information of all three detectors. The last stage is a post-processing stage in which a dedicated vertex finder is used to reconstruct primary vertices. This is followed by algorithms dedicated to the reconstruction of photon conversions and of secondary vertices.

The resolution of the track parameters at high p_T are dominated by the intrinsic detector resolution, while at low p_T the resolution is dominated by multiple scattering. The expected track-parameter resolutions, from Monte Carlo simulation, are shown in Table 4.1 [38], where momentum and angular resolutions are shown for simulated muons, and impact parameter resolutions are shown for simulated pions. The numbers quoted are only for tracks for which there was at least one hit in the vertexing layer. The resolution of a track parameter, X, can be expressed as a function of p_T as

$$\sigma_X(p_T) = \sigma_X(\infty)(1 \oplus p_X/p_T)$$

where $\sigma_X(\infty)$ is the asymptotic resolution expected at infinite momentum, p_X is a constant representing the value of p_T for which the intrinsic and multiple-scattering terms in the equation are equal for the parameter X under consideration, while $\oplus$ denotes addition in quadrature.

Determination of the lepton charge for high-p_T leptons is also important. For muons the charge is measured in the muon system, while for electrons it can only be measured by the inner detector. The charge misidentification for electrons is slightly worse than for muons because for electrons there are competing effects from bremsstrahlung and conversion of bremsstrahlung photons. For reconstructed muons with $p_T \approx 500$GeV the misidentification probability is ≈ 1 %.

The reconstruction efficiency of tracks differs also between pions, electrons

Table 4.1: *Expected track-parameter resolutions for muons and pions in the barrel (*$0.25 < |\eta| < 0.50$*) and end-cap (*$1.50 < |\eta| < 1.75$*) regions.*

Track parameter	$\sigma_X^B(\infty)$	$\sigma_X^{EC}(\infty)$
Inverse trans. momentum (q/p_T)	0.34 TeV^{-1}	0.41 TeV^{-1}
Azimuthal angle (Φ)	70 μrad	92 μrad
Polar angle ($\cot\Theta$)	0.7×10^{-3}	1.2×10^{-3}
Transverse impact parameter (d_0)	10 μm	12 μm
Long. impact parameter ($z_0 \sin\Theta$)	91 μm	71 μm

and muons, and also whether the track is isolated. In addition to multiple scattering effects, pions are affected by hadronic interactions in the detector material. Within or near jets the rate of fake tracks increases significantly because of the high density of tracks induces pattern-recognition problems. This effect increases as the jet p_T increases. Based on Monte Carlo simulations the reconstruction efficiency for pions and electrons varies between 85 and 95 %, while for muons it is expected to be above 95 %.

Vertexing

The reconstruction of the primary vertex (PV) is important in order to identify tracks coming from the primary collision and not from pile-up of additional minimum bias events at higher luminosity. The PV resolution in the transverse ($x - y$) and beam direction (z), as well as the reconstruction and selection efficiency are shown in Table 4.2 for simulated top-antitop pair events with and without a beam constraint. The additional beam constraint means to add the beam (spot) position as an additional pseudo-measurement to the existing ones for the vertex finding. The reconstruction and selection efficiencies are measured for vertices within $\pm 300\,\mu$m of the true vertex position in z. The PV is selected as the vertex with largest $\sum p_T^2$, where the sum runs over all constituent tracks. The reconstruction and selection efficiencies are rather high, the resolutions are $< 20\,\mu$m and $\approx 40\,\mu$m for the transverse

Table 4.2: *Primary vertex resolutions, reconstruction and selection efficiency with and without beam constraint (BC) for simulated $t\bar{t}$ events.*

Event	$x - y$ resolution (μm)	z resolution (μm)	Reconstruction efficiency (%)	Selection efficiency (%)
$t\bar{t}$ (no BC)	18	41	100	99
$t\bar{t}$ (BC)	11	40	100	99

and beam direction respectively.

4.2 Electrons

Electrons are reconstructed from clusters in the electromagnetic calorimeter. The rectangular clusters are formed with a fixed size and positioned to maximize the amount of energy within the cluster. The fixed size of the rectangular window depends on the particle type (electrons need larger clusters than photons). Several different fixed-sized clusters are built therefore and these are the starting points of calibration and selection of electron and photon candidates. For the standard reconstruction of electrons a seed electromagnetic tower with transverse energy above 3 GeV is taken from the EM calorimeter. For each reconstructed cluster or tower the reconstruction tries to find a matching track within a $\Delta\eta \times \Delta\phi$ window of 0.05×0.10 with momentum, p, compatible with the cluster energy, E (typical requirement for matching is to cut for $E/p < 10$). If a track is found the reconstruction checks for the presence of an associated photon conversion. An electron candidate is created only if the matched track has no associated conversion found. Otherwise the candidate is considered as a photon. With a 3 GeV threshold approximately 93 % of the true isolated electrons, with $E_T > 20$ GeV and $|\eta| < 2.5$, are selected as electron candidates.

After electron candidates have been found the standard identification of high-p_T electrons is done with three major types of classifications of electron candidates. The classes are called *loose*, *medium* and *tight*. Each level tightens the previous level's criteria. In the following the definitions of each of these electron candidate classes are given.

Loose electrons

Loose electrons are formed from cuts providing the simplest identification based on calorimeter information:

- detector acceptance $|\eta| < 2.47$,
- ratio of E_T in the first sampling of the hadronic calorimeter to E_T of the electromagnetic cluster (hadronic leakage),
- ratio of η of cell energies in 3×7 and 7×7 cells in the second layer of the EM calorimeter,
- ratio of ϕ of cell energies in 3×3 and 3×7 cells in the second layer of the EM calorimeter,
- lateral width of the shower in the second layer of the EM calorimeter.

The main motivation for taking the ratios of cell energies and the shower shape is that electron/photon showers are narrower and deposit most of their energies in fewer cells than hadronic showers. Additionally, high energety jets deposit a significant amount of energy in the hadronic calorimeter while electrons and photons deposit energy in the electromagnetic calorimeter. The hadronic leakage is defined as the ratio of transverse energy in the first section of the hadronic calorimeter to that of the electromagnetic calorimeter. This variable rejects such high energy jets. The result of these cuts is high electron identification efficiency but low background rejection.

Medium electrons

Medium electron cuts improve the quality by using the first layer of the EM calorimeter (strips) and the tracking variables. The following discriminating variables are used for defining medium electrons in the first layer of the EM calorimeter:

- loose cuts,
- showers are studied in a window of $\Delta\eta \times \Delta\phi = 0.125 \times 0.2$. Around the cell with the highest E_T a search is performed to find a window containing a second maximum. It serves to reject $\pi^0 \rightarrow \gamma\gamma$ decays which often form two maxima, if more than two maxima are found the second is considered. The discriminating variable used is the difference between the energy of the second maximum and the energy with the minimal value found between the first and the second maximum,
- use of the second largest energy deposit normalized to the cluster energy,
- total shower width,
- shower width over the three strips around the one with maximum energy deposit,
- fraction of energy outside the core of the three central strips but within seven strips.

The following cuts on track parameters are used for additional discrimination:

- at least one hit in the pixel detector,
- at least nine hits in the pixels and SCT,
- transverse impact parameter of the track $d_0 < 1$ mm.

The advantage of the medium cuts is that it increases the jet rejection by a factor of $3-4$ with respect to the loose cuts but the disadvantage is that at the same time it reduces the identification efficiency by 10%.

Tight electrons

The tight cuts use all the available information from the tracking system. The discriminating variables, using isolation, vertexing layer and TRT detector data, include:

- medium cuts,
- ratio of transverse energy in a cone $\Delta\mathrm{R} < 0.2$ to the total cluster transverse energy,
- at least one hit in the vertexing layer,
- $\Delta\eta(\mathrm{cluster} - \mathrm{track}) < 0.005$ between the cluster and the track,
- $\Delta\Phi(\mathrm{cluster} - \mathrm{track}) < 0.02$ between the cluster and the track,
- ratio of the cluster energy to the track momentum,
- total number of hits in the TRT,
- ratio of the number of high-threshold hits to the total number of hits in the TRT.

The requirement of hits in the vertexing layer of the Pixel detector reduces the electrons from photon conversion. The TRT detector provides discrimination power against pions because electrons emit more radiation than pions. Therefore cuts on the relative number of high threshold hits are used. The ratio of cluster energy to track momentum also distinguishes between electrons and charged hadrons: relativistic electrons should have an energy to momentum ratio close to unity. This ratio is affected by the bremsstrahlung differently in the tracker and in the calorimeter because the radiated photons - clustered around the electron - also deposit energy in the calorimeter while the momentum in the tracker is reduced.

Using $Z \rightarrow ee$ and QCD dijet Monte Carlo samples for electrons with $E_T > 20$ GeV within the range $|\eta| < 2.47$ and excluding the transition region between the barrel and end-cap calorimeters ($1.37 < |\eta| < 1.52$), the expected identification efficiencies are estimated to be 94%, 90%, and 72% with respective rejection factors against background jets with true $E_T > 20$ GeV of 1100, 6800, and 92000 for loose, medium, and tight electron identification, respectively [39].

4.2.1 Electron energy resolution

Energy resolution of reconstructed electrons is parametrized as $\sigma(E)/E = a/\sqrt{E} \oplus b \oplus c/E$. The dominant term in the resolution is the first term absorbing effects from statistical fluctuation in the calorimeter sampling, b is a constant and c is the noise term. Monte Carlo simulations have been used to estimate the energy response for electrons with an energy of 100 GeV [38]. The dominant first term has been predicted for such electrons to give 11% and 15% resolutions at small pseudorapidities and in the end-cap, respectively.

4.3 Jets

At hadron colliders, both the initial and final state of scattering processes consist of color-charged quarks and gluons. At the energy scale of a high energy collision the coupling between the partons vanishes asymptotically and can be described by perturbative QCD, but as the partons leave the close proximity of the primary interaction the energy scale enters into the non-perturbative regime where the strong coupling increases and therefore the color confinement of quarks takes place. A strong color-field develops between the quarks and gluons in the final (and initial) state and colorless hadrons are created in the final state of a collision. Depending on the p_T and multiplicity of the partons in the hard subprocess a highly collimated spray or shower of hadrons is produced, which is usually called a *jet*. Experimentally the partons cannot be seen; only the hadrons and their decay products can be detected and jets from them can be reconstructed, which can be associated with partonic intial or final states. Therefore a looking at a jet in a single event is not physical, the correct physical picture is to consider the jet production as a stochastic process to which a lot of possible underlying processes can contribute.

In this analysis we consider processes in which several jets are produced therefore a brief summary is given about the reconstruction and calibration of jets at ATLAS.

The principle detector for the jet reconstruction is the calorimeter system. The constituents of calorimeter jets are groups of calorimeter readout cells of energy deposits. The deposits in the calorimeter readout cells are grouped into topological clusters (topo-clusters). Topo-clusters are three-dimensional objects and take advantage of the fine calorimeter segmentation of the ATLAS detector. They are developed around calorimeter cells whose ratio of signal to root-mean-square (RMS) noise distribution is above a threshold of 4. Cells neighboring the seed that have a signal-to-RMS-noise ratio of 2 are then included iteratively, and finally all nearest cells are added to the topo-cluster. The magnitude of the topo-cluster four-vector is obtained by summing the energy of all the included cells, and its direction corresponds to that of a unit vector originating from center of the ATLAS coordinate system and pointing to the energy weighted topo-cluster barycenter. The topo-clustering algorithm includes a splitting step: All cells in a cluster are searched for local maxima in terms of energy content, and the local maxima are then used as seeds for a new iteration of topological clustering, which will split the original cluster in more topo-clusters.

These topo-clusters are then input to a jet finding algorithm. There are several algorithms to find jets, in this analysis the anti-k_T [40] algorithm has been used as it has been found to provide the best performance at ATLAS. The algorithm uses the clusters as *proto-jets* and defines a distance measure

$$d_{ij} = \min\left(p_{T,i}^{-2}, p_{T,j}^{-2}\right) \frac{\Delta_{ij}^2}{R^2} \tag{4.1}$$

$$d_{ii} = p_{T,i}^{-2} \tag{4.2}$$

where

- $p_{T,i}$, y_i, and ϕ_i are the transverse momentum, rapidity and azimuth of proto-jet i,
- $\Delta_{ij} = (\phi_i - \phi_j)^2 + (y_i - y_j)^2$ is the distance in the azimuth-rapidity plane between proto-jet i and j,
- $R = 0.4$ or 0.6.

The algorithm takes the list of all proto-jets and compute d_{ij} for all of them, and then finds the one with smallest d_{ij} and

- if $i \neq j$ removes proto-jet i and j and add their 4-vector sum as a new proto-jet,
- if $i = j$ removes proto-jet i and call it a final jet.

At this stage the jets are called *calorimeter jets* at the *electromagnetic scale* because the detector cells have been calibrated so far only assuming electromagnetic interactions. The next step is to bring the calibration to a *hadronic scale* that is to calibrate the jets to the jets that would have been reconstructed if it would have been possible to take all true final state hadron's contribution into account as well. After the hadronic scale, jet energy scale corrections have to be applied to correct for noise, pile-up and additional calibration algorithmic effects - at this stage jets are called *physics jets.* Finally the calibration sources in the physics process itself can be used (e.g. W or Z boson mass).

4.3.1 Jet energy scale calibration

The choice of jet energy scale (JES) calibration for the first ATLAS data is a Monte Carlo based jet-by-jet correction applied as a function of the jet transverse momentum and pseudorapidity [41]. The derivation of the jet energy scale calibration and the estimate of its uncertainty are based on a comparison of simulated jets reconstructed from the calorimeter jet constituents with jets built from stable particles excluding muons and neutrinos (called Monte

Carlo truth jets). Reconstructed jets are calibrated first to the energy scale measured by the calorimeters, called the electromagnetic (EM) scale. The electromagnetic energy scale is established using test-beam measurements for electrons and muons in the electromagnetic and hadronic calorimeters. This energy scale accounts correctly for the energy of photons and electrons, but it does not correct for all detector effects.

The *jet response*, $R(p_T, \eta)$, as a function of the transverse momentum and pseudorapidity, is defined as

$$R(p_T, \eta) = p_T^{jet} / p_T^{\mathrm{MC\ truth\ jet}}, \tag{4.3}$$

where $p_T^{MC\ truth\ jet}$ is the transverse momentum of the particle jet from the Monte Carlo event generation, and p_T^{jet} is the transverse momentum of the reconstructed calorimeter jet after the JES calibration. The determination of the jet energy-scale calibration consists of three steps. Firstly, the jet energy response at the electromagnetic scale, $R^{EM}(p_T^{\mathrm{MC\ truth\ jet}}, \eta)$, is determined in fixed $p_T^{\mathrm{MC\ truth\ jet}}$ bins. The mean of the jet response, determined by a Gaussian fit in each $p_T^{\mathrm{MC\ truth\ jet}}$ bin, is considered as the average jet response at the center of the $p_T^{\mathrm{MC\ truth\ jet}}$ bin considered. In a second step an inversion technique is applied to transform a jet response measured in $p_T^{\mathrm{MC\ truth\ jet}}$ bins to a jet response that is a function of $p_T^{jet,EM}(R^{EM}(p_T^{jet,EM}, \eta))$. Finally the resulting response is parametrized as a function of $p_T^{jet,EM}$ and η with free parameters for fitting.

The JES *correction* is defined as the inverse of the response function, and applied inclusively to all jets. The calibrated transverse momentum of a jet is then calculated as

$$p_T^{jet,calib} = 1/R^{EM}(p_T^{jet,EM}, \eta) \cdot p_T^{jet,EM}. \tag{4.4}$$

The jet four-momentum is calibrated in an equivalent way, using $1/R^{EM}(p_T^{jet,EM}, \eta)$ as a scale factor for each of its components. This definition implies that the jet direction remains unchanged after the JES calibration.

4.3.2 Jet energy scale uncertainties

There have been efforts to estimate the various systematic uncertainties associated with the current JES calibration method. The methods are all based on Monte Carlo variation of each component of the particular source of systematics. The JES uncertainties will be constrained with other methods in the future, when the estimate of its various components based on Monte Carlo variations is replaced by in-situ measurements such as single particle studies. The main contributions to the JES systematics have been found to belong to three main categories:

1. Detector description, experimental conditions and the JES calibration method. In this set of uncertainties the main sources were found to be the following:

   - Dead material: the jet energy scale is affected by any increased amount of inactive material since the energy deposited by particles in this extra material is not measured or accounted for in the standard calibration procedure. The effect of extra dead material on the jet energy scale has been evaluated with a dedicated geometry model in the simulations.
   - Topo-cluster noise thresholds: the electronic noise in data could differ from the noise description used in the Monte Carlo simulation. To evaluate this uncertainty Monte Carlo samples have been reconstructed with different signal-to-noise thresholds for topo-cluster seeds and neighbors.
   - Beam spot: if the beam spot is shifted with respect to the detector center, the origin of the jet could differ from the one assumed by the reconstruction, and the jet p_T^{jet} could be biased as a consequence. Variations in the JES using different beam spot positions have been studied.
   - Absolute EM scale: a 3% flat uncertainty has been assumed for this source. It basically accounts for differences between the test-beam studies and the full simulation, different calibration methods

Table 4.3: *Jet energy scale relative systematic uncertainties from Monte Carlo based study for anti-k_T jets with $R = 0.4$.*

	$R = 0.4$	$R = 0.4$
η region	$p_T^{jet} > 20$ GeV	$p_T^{jet} > 60$ GeV
$0 < \lvert\eta\rvert < 1.2$	7.6%	5.9%
$1.2 < \lvert\eta\rvert < 2.8$	8.4%	6.4%

and the time stability of the electromagnetic scale from variations in the detector.

- Assumptions in the JES calibration method: in the method it is assumed that every constituent needs the same average compensation when deriving the calibration constants, and the assumptions made in the jet selection and topology applied during the calibration.

2. The physics model and parameters employed in the Monte Carlo event generator, fragmentation and underlying event model. Two Monte Carlo generators, ALPGEN [32] and PYTHIA [25], have been used and different models in all stages of event generation have been varied and the impacts on jet response have been studied.

3. The hadronic shower model used in the Monte Carlo detector simulation. The properties of the hadronic showering of particles interacting in the calorimeter influence the shape and extent of the energy deposits and therefore the jet energy scale. ATLAS test-beam data for single pions with energies ranging from 2 to 180 GeV have been compared to various set of parameters for the description of hadronic showers.

A summary, including all the effects variation studies above, of jet energy systematic uncertainties for different p_T^{jet} and η regions, with jet cone size $R = 0.4$, is given in Table 4.3 [41].

Multiple interactions

With increasing beam intensity a non-negligible fraction of the events will contain multiple proton-proton interactions in the same bunch crossing (pile-up). These extra interactions produce additional soft particles that can overlap with jets produced in the hard scattering primary interaction resulting in extra energy added to jets. The estimate of the pile-up relative systematic uncertainty has been done using ATLAS runs up to May 17th, 2010. This period corresponds to 7 nb^{-1} of integrated luminosity. For jets with $20 < p_T^{jet} < 50$ GeV, the pile-up relative systematic uncertainty was estimated to be about 1% in the barrel and 1-2% in the endcaps. For $p_T^{jet} > 50$ GeV, the pile-up uncertainty was found to be only significant for $|\eta| > 2.1$ and it is smaller than 1%.

4.3.3 Jet energy resolution

The energy resolution of reconstructed jets is parametrized as

$$\frac{\sigma}{E} = \frac{a}{\sqrt{E(\text{GeV})}} \oplus b \oplus \frac{c}{E}. \tag{4.5}$$

The first tem, so-called *sampling term*, is due to the statistical fluctuations in the calorimeters. The second constant, b, is due to the calorimeter non-compensation and detector non-uniformities leading to differences in the resolution in the various parts of the calorimeter. The last term is the noise contribution to the energy resolution.

Full simulated PYTHIA [25] QCD dijet events have been used [38] to measure the energy resolution of reconstructed jets as a function of the jet energy. Table 4.4 shows the results obtained for the three coefficients for k_T algorithm with parameter $R = 0.6$ in two different regions in pseudorapidity.

Table 4.4: *Parameters of the jet energy resolution obtained from dijet events.*

	a (%)	b (%)	c (GeV)
$0 < \|\eta\| < 0.5$	64	2.7	5.4
$1.5 < \|\eta\| < 2.5$	112	1.0	10.0

4.4 Missing transverse energy

In decay processes of massive vector bosons neutrino final states can carry away a large fraction of the momentum. The neutrino has no electric charge and only takes part in weak interactions, therefore it doesn't interact electromagnetically with the active detector material. Weak interactions with the nucleus of the detector atoms are possible but have a negligible cross section. Therefore experimentally neutrinos show up as imbalance in the overall measured momentum of the hard scattering process. However, there exist also several instrumental sources for overall momentum imbalance. One striking feature of hadron colliders is that the hadron remnants, after the scattering, can carry on their flight down the beam pipe. This is only true for the longitudinal direction along the beam pipe. In transverse direction though the detector system covers the full solid angle. Therefore conservation of the measured momentum, before and after the proton-proton scattering process, in the transverse $x-y$ plane must take place. To measure momentum imbalance in the transverse plane a new variable, the transverse missing energy or momentum (E_T^{miss}), has been defined. Its calorimeter-based definition takes the negative vector sum of the calorimeter cells in the $x-y$ plane

$$\begin{aligned} E_x^{miss} &= -\sum_{i=1}^{N_{cell}} E_i \sin\theta_i \cos\phi_i \\ E_y^{miss} &= -\sum_{i=1}^{N_{cell}} E_i \sin\theta_i \sin\phi_i \\ E_T^{miss} &= \sqrt{(E_x^{miss})^2 + (E_y^{miss})^2} \end{aligned} \tag{4.6}$$

where E_i, θ_i and ϕ_i are the cell energy, polar angle and azimuthal angle respectively. E_T^{miss} is reconstructed over the range $\eta < 4.5$ using calorimeter information, and adding corrections for energy loss in the cryostat (cryo term) and measured muons (muon term). Noise contributions are suppressed by limiting the number of cells, N_{cell}, used in the sum. This is done by topo-cluster seeded by cells with $|E_i| > 4\sigma_{noise}$, and are built by iteratively adding neighboring cells with $|E_i| > 2\sigma_{noise}$ and, finally, by adding all direct neighbors of the accumulated secondary cells. The final missing transverse energy at cell level is defined as

$$E_{x,y}^{miss,final} = E_{x,y}^{miss,calo} + E_{x,y}^{miss,cryo} + E_{x,y,}^{miss,muons}. \tag{4.7}$$

The $E_T^{miss,calo}$ term is defined above as summing up all calorimeter cells above noise threshold. Calibration of this term is done by cell or cluster weighting methods.

The $E_T^{miss,muon}$ term is calculated from the momenta of muons measured in a large range of pseudorapidity, $|\eta| < 2.7$

$$E_{x,y}^{miss,muon} = - \sum_{\text{rec.muons}} E_{x,y}. \tag{4.8}$$

In the region $\eta < 2.5$ only good-quality muons in the muon spectrometer with a matched track in the inner detector are considered. For higher values of pseudorapidity, outside the fiducial volume of the inner detector, no matched track is required and the muon spectrometer is used alone. For muons energy lost in the calorimeter is already included in the calorimeter term. No p_T threshold cut is applied to the reconstructed muons. The overall E_T^{miss} resolution is only marginally affected by the muon term due to the good identification and resolution of muons at ATLAS. However, unmeasured, badly measured or fake muons can be a source of large fake E_T^{miss}.

The $E_T^{miss,cryo}$ term is due to the cryostat between the LAr barrel electromagnetic calorimeter and the tile barrel hadronic calorimeter. The thickness of the cryostat is about half an interaction length where hadronic showers can loose energy. The loss can be recovered as a correction using the correlation of energies between the last layer of the LAr calorimeter and the first layer of the hadronic calorimeter. A similar correction for the end-cap cryostats is also applied. The cryostat correction is defined as

$$E_{x,y}^{miss,cryo} = - \sum_{rec.jets} Ejet_{x,y}^{cryo}, \tag{4.9}$$

where all reconstructed jets are summed in the event, and

$$Ejet^{cryo} = w^{cryo} \sqrt{E_{EM3} \times E_{HAD}}, \tag{4.10}$$

where w^{cryo} is a calibration weight determined during the calibration and E_{EM3} and E_{HAD} are the jet energies in the third layer of the electromagnetic and first layer of the hadronic calorimeter. This term contributes at the level of $\approx 5\%$ per jet for jets with $p_T > 500$ GeV.

4.4.1 Refined E_T^{miss}

A more precise calculation of E_T^{miss} is possible by associating the calorimeter cells with each of the different types of the offline reconstructed physics objects (electrons, photons, τ-leptons, jets, muons) in a chosen order: electrons, photons, muons, hadronically decaying τ-leptons, b-jets and light jets. Refined calibration of the object is then used to replace the initial global calibration cells as the calibration of these objects is known to a higher accuracy. During association care has to be taken not to double count cells corresponding to overlapping objects. All cells, even those not associated with any such objects (called *CellOut* term), are also added during the refined calculation. The total contribution therefore is defined as

$$E_{x,y}^{Refined} = -(E_{x,y}^{RefElePho} + E_{x,y}^{RefTau} + E_{x,y}^{Refbjets} + E_{x,y}^{RefJets} + E_{x,y}^{RefMuon} + E_{x,y}^{CellOut}). \tag{4.11}$$

Studies have found that the *CellOut* term contributes mainly from soft physics processes.

4.4.2 E_T^{miss} resolution

It is more quantitive to also define the total transverse energy of an event, $\sum E_T = \sum_i^{N_{cell}} E_i \sin\theta_i$, and investigate the E_T^{miss} performance as a function of $\sum E_T$. With the minimum bias events at 7 TeV center-of-mass energy, the E_T^{miss} resolution, calculated as the width variation of E_x^{miss} and E_y^{miss} as a function of $\sum E_T$, has been compared between data and Monte Carlo [42]. For minimum bias events contribution comes only from two terms: the main fraction of the contribution comes from CellOut term, and a small contribution from the RefJet term. The resolution has been found to be $\sigma(E_x^{miss}, E_y^{miss}) \approx 0.4 \times \sqrt{\sum E_T}$ GeV. Studies have also been done with events in the L1Calo trigger stream of events at 7 TeV center-of-mass energy. In this stream there are contributions not only from the the CellOut and RefJet terms but also from the RefEle term. Results show that the resolution is a bit worse than for the minimum bias events, for the L1Calo stream (see Section *Trigger and data aquisition*) the resolution is $\sigma(E_x^{miss}, E_y^{miss}) \approx 0.5 \times \sqrt{\sum E_T}$ GeV.

4.5 Muons

With the power of two independent high precision tracking systems, the muon spectrometer and the inner detector, ATLAS is capable of identifying and reconstructing muons with high efficiency up to $|\eta| < 2.7$.

The *stand-alone muon* reconstruction is based completely on the muon spectrometer. As a pre-processing of raw data, first drift-circles are formed in the MDTs or clusters in the CSCs and the trigger chambers (RPCs and TGCs). Then pattern recognition algorithms try to find segments and then tracks in the bending plane in the muon chambers. Hits in the precision chambers are used and the segments found are required to point to the center of ATLAS. The hit coordinate ϕ in the non-bending plane measured by the trigger chambers is associated to the segment when available. A minimum of two track segments in different muon stations are combined to form a muon candidate using three dimensional tracking in the magnetic field. Then the muon candidate track is fitted and the fitted track parameters (p_T, η, ϕ, distance to closest approach to primary vertex both along the beam axis and in the transverse plane) are extrapolated to the interaction point taking into account both multiple scattering and energy loss in the calorimeters. For the energy loss the reconstruction uses either a parameterisation or actual measurements of calorimeter energy losses. Typical muon energy loss in the calorimeters is $\sim$3 GeV.

The *combined muon* reconstruction associates the stand-alone muon spectrometer candidates to an inner detector track, using Pixel, SCT and TRT detectors. The association between the stand-alone and inner detector tracks is performed using a χ^2 fit, defined from the difference between the respective track parameters weighted by their combined covariance matrices. The parameters are evaluated at the point of minimum approach to the beam axis. The combined track parameters are obtained either from a statistical combination of the tracks, or from a refit to the full track.

The reconstruction and identification efficiencies for muons with $p_T > 10$ GeV, as extracted from W and Z signal Monte Carlo samples is estimated to be 94%. The availability of muons with energies up to 100 GeV energy in cosmic rays made it possible to cross check the results. Cosmic ray studies indicate that the performance is in agreement with Monte Carlo expectation. The tracking resolution has been measured to be better than 5% and the muon detection efficiency is in reasonable agreement with the values measured in simulated events. Recent collision data has also been used to cross check the muon reconstruction efficiency predictions [43] and agreement was found also within the statistical uncertainties with respect to previous results.

4.5.1 Non-prompt and fake muon sources

We define *prompt muons* as real muons coming from the decay of particles coming directly from the hard subprocess of scattering of partons from the proton. The main sources of *non-prompt* muons are real muons from the following sources:

- heavy flavor (b and c quarks) decays,
- early π/K decays, or “decays in-flight”, in which the muon is tracked in the inner detector,
- late π/K decays, or “decays in-flight” that occur when the muon from the decay is not tracked in the inner detector.
- muons originating from showers in the calorimeter.

Fake muons are objects which are reconstructed as muons but do not originate from muons such as:

- “punch-throughs”, showers not fully contained in the calorimeter,
- “sail-throughs”, that occurs when a non-muon particle crosses the calorimeter and enters the muon spectrometer.

The decay-in-flight process, dominant at low momentum, results in genuine muons that produce high quality tracks in the muon spectrometer, while the punch-through process, dominant at high momentum, typically leads to poorly reconstructed muon spectrometer tracks not correlated with the actual presence of a muon. The dominant contribution for combined muons are therefore coming from heavy flavor and late decay-in-flight processes. The contribution of π/K decays in inclusive muon spectrum measured from minimum bias collision events have been estimated to be at a level of $\approx$ 0.05%. The knowledge on the fraction of heavy flavor decay muons depends on the understanding of heavy flavor to light flavor fractions produced in direct collisions or during jet evolution, therefore it is expected to depend on the particular analysis applied.

4.5.2 Muon momentum resolution

We define the resolution as

$$\frac{\Delta p}{p} = \frac{p_{\mathrm{ID}} - p_{\mathrm{MS}}}{p_{\mathrm{ID}}} \qquad (4.12)$$

where p_{ID} is the muon momentum as estimated in the inner detector, while p_{MS} is the momentum of the track reconstructed by the muon spectrometer and then back-extrapolated to the primary vertex. The distribution of $\frac{\Delta p}{p}$ has been measured using proton-proton collision events. The measured muon momentum resolution has several dominant contributions [43]. For the inner detector the momentum resolution is dominated by multiple scattering for muons with $p_T < 20$ GeV, providing a momentum resolution of $\approx 2\%$. The standalone muon spectrometer resolution is dominated by energy loss fluctuations up to a momentum of 10 GeV and by multiple scattering above 10 GeV. A fractional stand-alone momentum resolution of $\approx 5\%$ is expected for muons with $p_T < 10$ GeV. The combined muon momentum resolution varies between 5 and 8 % depending on the p_T and η of the muon. Muons in the central barrel region ($|\eta| < 1.0$) and with high transverse momentum have the best resolution of about 5%. Muons outside this region or with low momentum have a momentum resolution of about 8 %.

Chapter 5

Event selection

In this chapter the analysis is presented for top quark pair signal observation in the muon+jets channel based on an integrated luminosity of 2.9 pb^{-1} of 7 TeV center-of-mass energy proton-proton collision data collected from April until September of 2010 in ATLAS.

5.1 General outline of the analysis

The ATLAS experiment has just started to collect proton-proton collision data. In the early phase of the experiment it is important to establish the existence of benchmark processes in the data. Given that only a short time has passed since the first collisions the understanding of the detector systems and the particle and physics object identification and reconstruction is still evolving. Under such circumstances key observations in the data must be based primarily on methods that rely on the Monte Carlo simulations as little as possible and use data-driven approaches in most cases. This thesis uses two major data-driven methods in order to measure the background rates for the top quark pair signal from the data. Rates from Monte Carlo simulations are only used for normalization of backgrounds which have either negligible contribution or which are known to a reasonable precision.
The general strategy of the top quark observation analysis presented is to

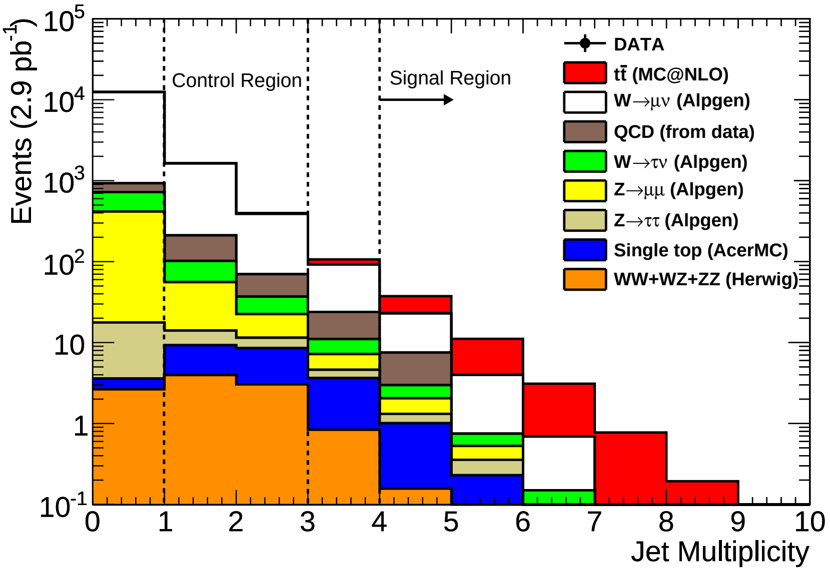

Figure 5.1: *Expected distribution of jet multiplicity for candidate events after* $W \rightarrow \mu\nu$*+jets selection from Monte Carlo event generators and after full detector simulation. On the stacked jet multiplicity plot the top quark pair signal expectation is indicated with an arrow pointing to the red colored histogram, the* $W \rightarrow \mu\nu$*+jet background contribution is indicated with white color and the QCD multijet background is indicated with brown color.*

define a signal enriched region, the signal region (SR), where we expect the top quark pair signal populates the final states the most and the background contributions can be estimated from sideband regions, and a control region (CR) which is signal depleted and where the background rates are measured and extrapolated to the SR. The analysis does not use b-quark or b-jet discrimination methods in order to minimize the sensitivity of the results on the knowledge of the fractions of heavy and light quark flavor processes in the data and on the b-tagging performance.

As described in Section 2.3.2, the main signal pattern of top quark pairs in the muon plus jets channel is the presence of an isolated muon with high transverse momentum, at least four jets and significant amount of missing transverse energy. During the analysis therefore triggering on a single muon trigger (see Section 5.3.1), and an offline reconstructed single, isolated muon with transverse momentum (p_T) greater than 20 GeV is required. Missing transverse energy (E_T^{miss}) above at least 20 GeV is also required to select events with high transverse momentum neutrinos from the W decays. The choice of the cuts at 20 GeV is explained in Section 5.3. This set of discrimination cuts however select $W \rightarrow \mu\nu$+jets as well as top quark pair signal events in the muon plus jets final state.

After the single muon trigger, the single offline, isolated high p_T muon and the transverse missing energy discrimination the definition of the SR and CR is based on the jet multiplicity of the events. Top quark pair candidates are expected to populate the high jet multiplicity regions, this is illustrated in Figure 5.1 which shows the jet multiplicity distribution after the selection cuts mentioned, and using Monte Carlo generated 7 TeV center-of-mass proton-proton collision events with full detector simulation. From Figure 5.1 one can draw the following important conclusions:

- the low jet multiplicity region (in particular the region labeled as "Control Region") is almost free from the top quark pair signal;
- top quark pair events start to significantly populate the jet multiplicity bins from the bin of three jets on, reaching a maximum at around four jets, and have a dominant contribution in the high jet multiplicity

region, where the label “Signal Region” is used for indication;

- $W \to \mu\nu$+jets events populate all jet multiplicity bins throughout the phase space from low to high jet multiplicity, with decreasing contribution, but significant contribution in the signal region;
- from low to middle jet multiplicity there are contributions from boson pair production (WW, WZ, ZZ), Z production, final states with tau lepton ($W \to \tau\nu$, $Z \to \tau\tau$), but towards the high jet multiplicity region these contributions are suppressed almost completely;
- the QCD multijet background also populates all jet multiplicity bins, with decreasing contribution, and also contributing with a significant fraction to the signal region.

The definition of the CR and SR in this analysis is based on these conclusions. The background rates for the top signal are measured in the sideband or control regions at low jet multiplicity and extrapolated to the signal region. The control region is defined such that, after the lepton and missing transverse energy selection cuts, the event must have exactly 1 jet or 2 jets. In this thesis both the exclusive 1 and 2 jet bins are used for either the background normalization in the control region or for the extrapolation to the signal region. The physical reason for using exclusive bins in the control region will be explained in Section 5.6.2. The signal region is defined such that the presence of at least four jets, with at least 25 GeV transverse momentum each, is required in the event. Therefore the SR selection is an inclusive selection for at least four jets. The choice of inclusive jet selection for signal region was made to have maximal statistics and signal yield in the data. The method to extrapolate the background rate from the sideband CR uses the assumption that the ratio of rates of $W \to \mu\nu$+jets events in the neighboring exclusive jet multiplicity bins is constant. In the next sections the validity of this assumption will be discussed too. The estimation and suppression of the instrumental QCD multijet background is also based on a data-driven approach which defines, conceptually similarly to the general strategy used for the top signal observation, a multijet background enriched region to measure the relative enhancement of fake and non-prompt muons, originating from the multijet environment, with respect to the signal enriched region. The details of this method will be discussed in the analysis sections.

5.2 Data sample

5.2.1 Data quality selection

As described in Section 3.2.4 at ATLAS the data is collected in luminosity blocks. To monitor the data quality color encoded flags, so-called *data quality flags* (DQ flag), are used to indicate if the detectors and triggers were performing well during data taking [44]. A DQ flag is assigned for each subdetector, or data acquisition system, and it is also given globally for each luminosity block. There are three types of data quality flags: red, yellow and green. The green color indicates that a particular subdetector system performed well during the data taking of the corresponding luminosity block. This makes it possible to filter on the data and use only those luminosity blocks for data analysis which were flagged with green DQ flags. The data quality flags required to be green for this analysis ensure stable 3.5 TeV LHC beams and L1 central trigger and luminosity determination to be in good conditions. Also all the inner detector, calorimeter and muon spectrometer flags are required to be green. Additionally combined *virtual* flags have been constructed, based on the underlying detectors involved, to qualify the performance of physics object reconstruction. Such requirements filter on the performance of tracking of electron and muon candidates, vertexing, muon reconstruction, electron reconstruction, missing transverse energy terms and jet reconstruction. In particular for the muon reconstruction the global detector alignment performance and the magnet system are required to have green DQ flags.

The meaning of yellow and red data quality flags is to tag luminosity blocks for which either the decision has not been made or has been made to flag problems with the performance of any of the reconstructed objects or with any of the relevant subdetectors, respectively.

5.2.2 Luminosity of data sample

In the analysis, the 2010 ATLAS running periods A, B, C, D, E and F has been used from the data. The total integrated luminosity of this data sample was measured to be 2.9 pb^{-1}. The luminosity calibration was based primarily on van de Meer scans of the proton beams (see Section 3.2.5). The statistical uncertainty on the luminosity estimate is at a negligible level and the ATLAS luminosity working group reports a systematic uncertainty of 11% on the estimate.

5.2.3 Non-collision background rejection

Hard scatterings from real collisions can have significant background from several non-collision events like beam-halo, cosmic background, etc. Such background sources are not coming from the hard scattering vertex therefore they usually produce tracks which cannot be associated to any of the reconstructed vertices. Therefore, prior to any analysis event selection, events are processed only if any of the reconstructed primary vertex candidate has at least five associated reconstructed tracks.

5.3 Selection of reconstructed objects

The main motivation for object and event selection cuts are to efficiently select signal and signal-like events while suppressing instrumental QCD multijet background which is a general feature of hadron colliders. Some of the selection cuts on the physics objects used in this thesis are the result of a Monte Carlo simulation based cut optimization study [45] during which various discriminators have been scanned to obtain maximal signal over background ratio (S/B) or significance ($S/\sqrt{S+B}$). The main motivation for the individual selection cuts can be understood from the distributions of the corresponding variables and are explained in the next sections.

In the muon+jets analysis, presented in this chapter, two approaches will be used to estimate or suppress the instrumental QCD multijet background: the analysis will be done both with or without applying a cut on the combination of missing transverse energy and the reconstructed transverse W mass, called the *triangular cut* (see section 5.3.5). The two approaches let less or more multijet background into the CR and SR event candidates and therefore provide a way to confirm the confidence in the final results by comparison of the two separate analysis scenarios.

The following preselection cuts were applied, unless otherwise stated:

- single muon trigger (either L1_MU10 or EF_mu10_MSonly),
- exactly one offline isolated muon with $p_T > 20$ GeV and $|\eta| < 2.5$,
- missing transverse energy cut, $E_T^{\mathrm{miss}} > 20$ GeV,
- exactly one jet with $p_T > 25$ GeV, $|\eta| < 2.5$,
- $E_T^{\mathrm{miss}} + M_T(W) > 20$ GeV (triangular cut, see section 5.3.5).

This set of cuts will be referred to as "$W \rightarrow \mu\nu$+1 jet selection with triangular cut".

5.3.1 Muon trigger

The choice of the trigger is based on the rate of the trigger and on whether the trigger is prescaled. There are two triggers used in the analysis. The first one is a level one muon trigger, L1_MU10, and is used for data in run periods A to E3. In the early period of data taking, only the level one hardware-based triggers were enabled and the high level triggers were in pass-through mode, that's why in the analysis a level one trigger is used for the analysis of the first periods of data taking. The second is a high level muon trigger, EF_mu10_MSonly, used for the analysis of data run periods E4 to F. The EF_mu10_MSonly high level trigger is seeded by the level one L1_MU0 trigger. Neither of the triggers were prescaled in the data runs used for this analysis. Figure 5.2 shows typical online L1 muon trigger rates (in the example for run 160801). The rate of L1_MU0 and L1_MU10 triggers are quite high and stable therefore they both provide good statistics. The high rate of L1_MU0 was the reason for choosing the EF_mu10_MSonly trigger as soon as it was enabled. The "MSonly" term in the name of the trigger means that for the trigger decision only the muon spectrometer information was used, it was not required that the triggered muon candidate tracks be matched to any inner detector tracks.

Trigger efficiency curves from Monte Carlo simulation of fully reconstructed $Z \rightarrow \mu\mu$ events can be used to estimate the high efficiency regions of the L1_MU10 and EF_mu10_MSonly triggers as a function of the transverse momentum and the pseudorapidity of the μ candidates. The trigger efficiency is measured with respect to offline reconstructed muons from $Z \rightarrow \mu\mu$ Monte Carlo simulated events. Once there will be reasonable statistics from real Z$\rightarrow$ $\mu\mu$ events in data, that can be used to re-evaluate the muon trigger efficiencies. Figure 5.3 shows the trigger efficiency curves, obtained from the Monte Carlo simulated events, as a function of the transverse momentum and the pseudorapidity of the muon candidates. The muon transverse momentum trigger efficiency curves demonstrate the turn-on behavior of the muon trigger and show that above 10 GeV the efficiency quickly reaches a stable plateau region. The muon pseudorapidity trigger efficiency curves reflect the coverage of the muon trigger detector system: for the L1_MU10 hardware based trigger the lower efficiency in the central pseudorapidity region shows the poorer detector coverage of the L1 trigger system in the barrel region, while the curve of the EF_mu10_MSonly trigger shows the result of the more precise, offline software based, high level trigger algorithms which use the full muon detector information.

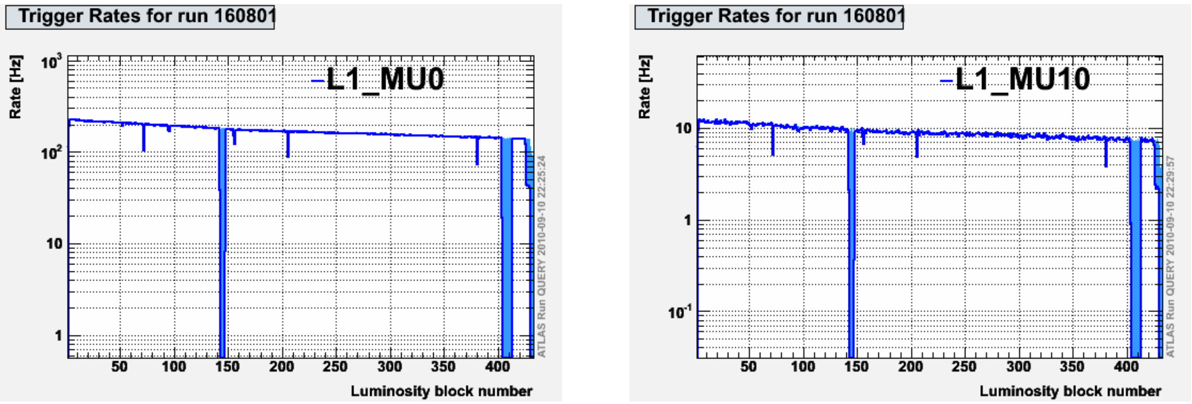

Figure 5.2: *Trigger rates in run 160801 for L1_MU0 and L1_MU10 muon triggers.*

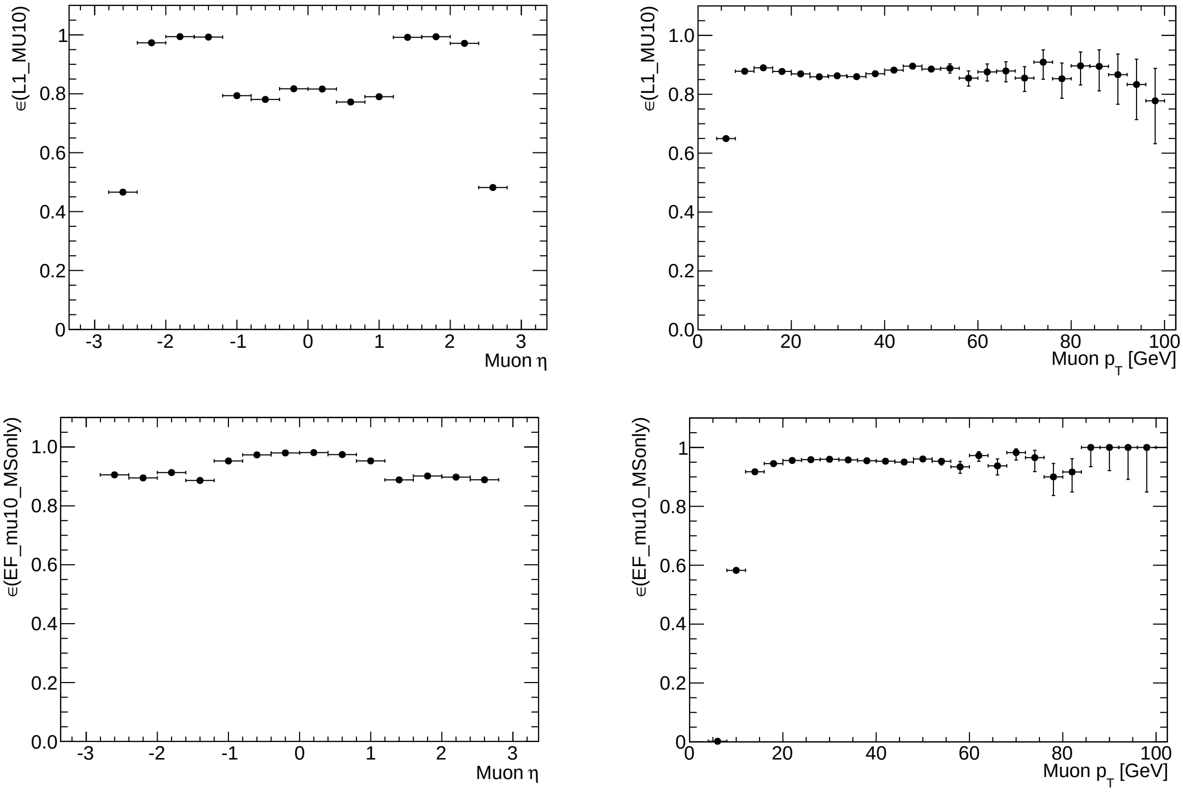

Figure 5.3: *Trigger efficiency curves for the L1_MU10 and EF_mu10_MSonly muon triggers with respect to offline reconstructed muons as a function of the p_T and η of the muon, using full simulated $Z \to \mu\mu$ Monte Carlo events.*

5.3.2 Muon selection

Reconstructed muon candidates are required to be combined inner detector and muon spectrometer tracks. In order to select muons efficiently from massive W decays, and to be well above the trigger p_T threshold of 10 GeV, muons are required to have at least 20 GeV of transverse momentum. Increasing the transverse momentum threshold from 20 GeV to higher values would decrease the expected signal yield. To select muons only from fiducial regions of the detectors an acceptance cut in the pseudo-rapidity region of $|\eta| < 2.5$ is applied on the offline reconstructed muons. This acceptance cut also maximizes the event acceptance of the Inner Detector (and therefore combined tracking). To suppress muons originating from heavy flavor decays within jets, muons are removed from the event if their distance to a jet, $\Delta\text{R}(\mu - \text{jet})$, is closer than 0.4. The choice of the value 0.4 is driven by the $\Delta\text{R}(\mu - \text{jet})$ distribution in fully simulated Monte Carlo $W \rightarrow \mu\nu$+jets events, shown on Fig 5.4. The distribution has a clear transition region at around $\Delta\text{R} = 0.4$. We consider the entries below 0.4 to be due to muons within jets as the jet cone size used in this analysis is 0.4 - matching well with the position of the transition.

Quality cuts for muon candidates are applied as a result of the cut optimization analysis mentioned above. Calorimeter isolation and object separation cuts are also applied to reduce contamination from instrumental QCD multi-jet environment. Therefore the following set of cuts are used to select muon candidates for the analysis:

- $\Delta\text{R}(\mu,\text{any reconstructed jet}) > 0.4$,
- the sum of the transverse energy in the calorimeter in a cone of $\Delta\text{R} = 0.3$ around the muon candidate (except the muon's transverse energy), so-called *calorimeter isolation*, is required to be smaller than 4 GeV,
- the sum of the transverse momentum of the reconstructed tracks in a cone of $\Delta\text{R} = 0.3$ around the muon candidate (except the muon's transverse momentum), so-called *track isolation*, is required to be smaller than 4 GeV.

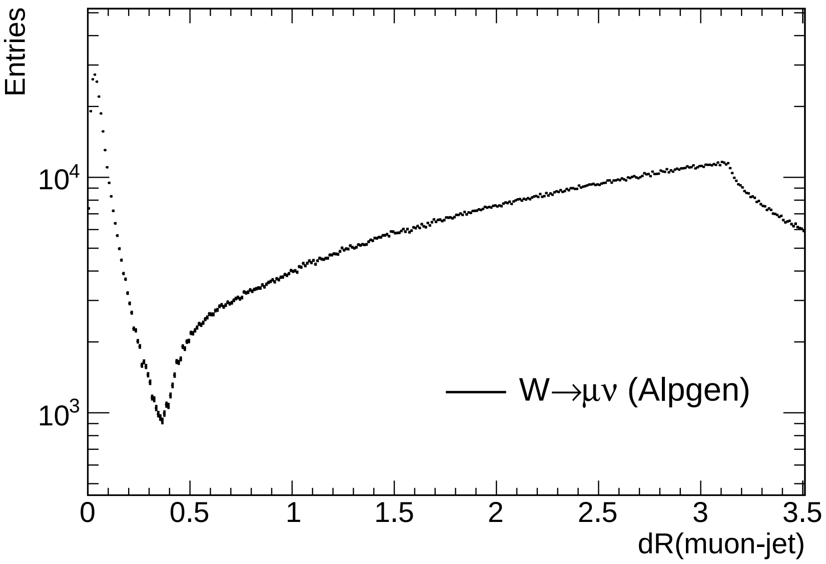

Figure 5.4: *Distribution of the distance,* $\Delta\mathrm{R}(\mu-\mathrm{jet})$*, between reconstructed muon and jet candidates.*

Control plots for the transverse momentum, pseudo-rapidity, azimuthal angle, calorimeter and track isolation are shown for the $W \to \mu\nu + 1$ jet selection in Figures 5.5, 5.6, 5.7, 5.8 and 5.9, respectively. As mentioned before the distributions are shown after applying the triangular cut (see section 5.3.5), except for the distributions of the muon isolation variables (track and calorimeter based isolation). This cut suppresses the QCD multijet background, therefore it is not included in the Monte Carlo samples for the transverse momentum, pseudo-rapidity, azimuthal angle plots. These distributions illustrate that the Monte Carlo already describes the data well. For the case of the muon calorimeter and track isolation distributions, which are sensitive on the presence of the QCD multijet environment, a PYTHIA [25] dijet Monte Carlo sample was used to show the expectations from simulation. These two distributions also show a reasonable agreement with the data, their discriminator values are indicated on the plots. The choice of the values, 4 GeV both, are driven by the fact that these distributions show a clear signal enhancement towards smaller values of isolation. These variables give a measure of the amount of radiation present around the muon in the event. The effect of enhancement for W+jets events towards small values of isolation can be understood by imagining that a single muon from the decay of a massive boson should be well isolated, that is the radiation (in form of calorimeter deposits or tracks) around the muon should be small with respect to the momentum of the muon. The effect is opposite for non-prompt or fake muons within or near jets where the amount of radiation is rather high everywhere in the event therefore the average energy or track multiplicity is high when compared to the momentum of a non-prompt or fake muon. The two isolation variables are not used in the analysis directly for absolute Monte Carlo normalization of any backgrounds. They are used mainly in data-driven approaches: the relative enhancement produced by applying the isolation cut with respect to not applying it is used. In any case the values used for methods based on relative change in the isolations are all measured from the data.

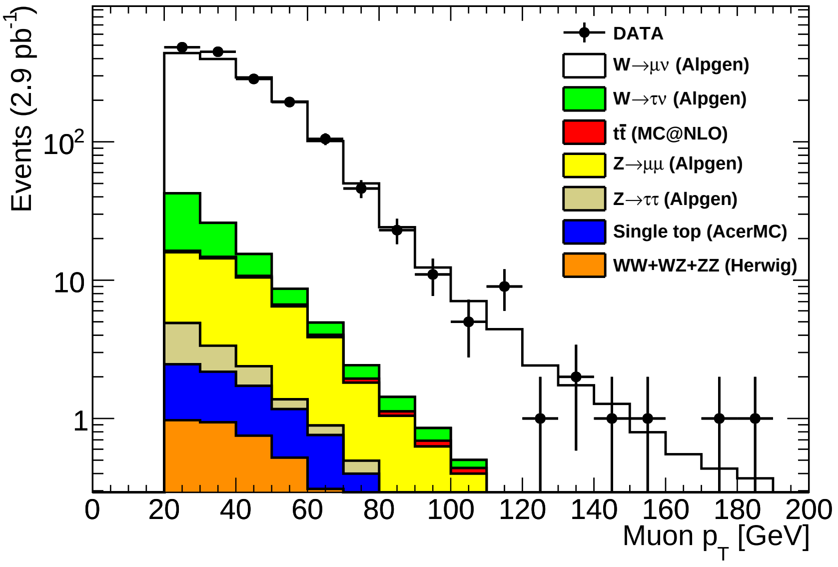

Figure 5.5: *Control plot showing the distribution of p_T of muon candidates from Monte Carlo simulation and data after preselection cuts.*

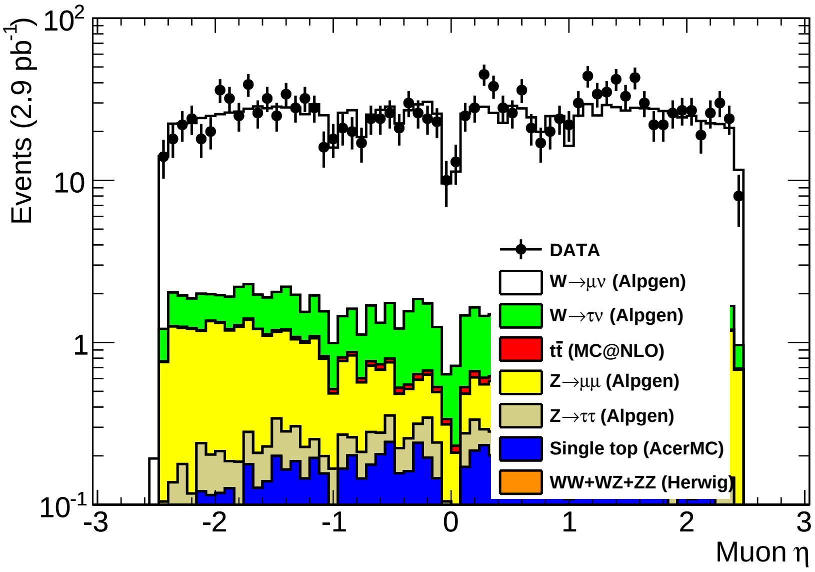

Figure 5.6: *Control plot showing the distribution of pseudorapidity of muon candidates from Monte Carlo simulation and data after preselection cuts except the cut on pseudorapidity.*

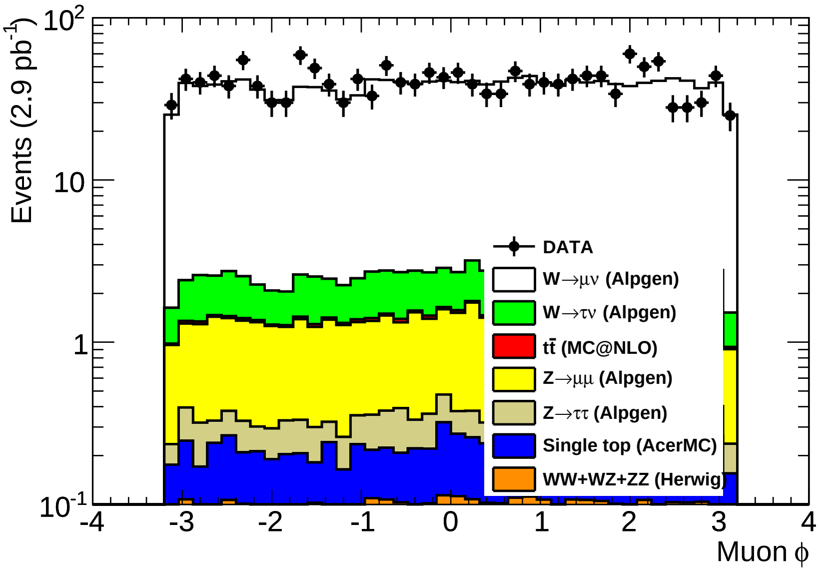

Figure 5.7: *Control plot showing the distribution of the azimuthal angle of the muon candidates from Monte Carlo simulation and data.*

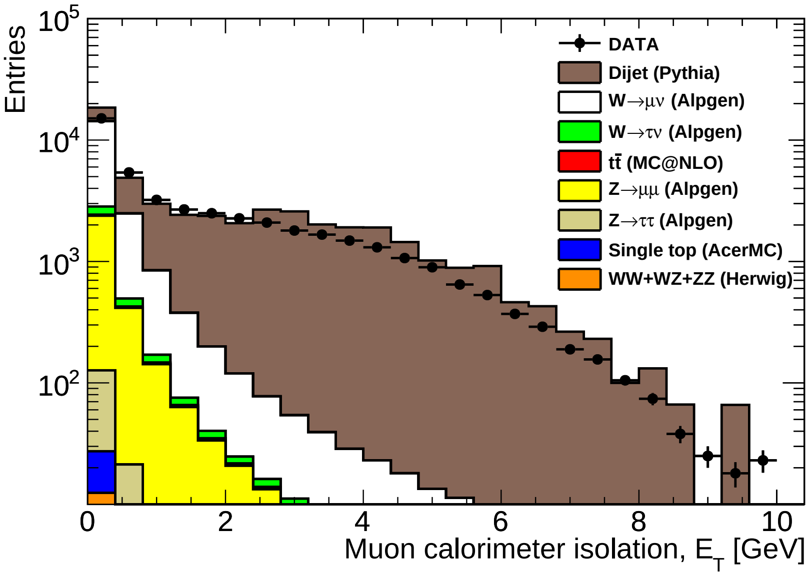

Figure 5.8: *Control plot showing the distribution of calorimeter isolation, EtCone30, of muon candidates from Monte Carlo simulation and data.*

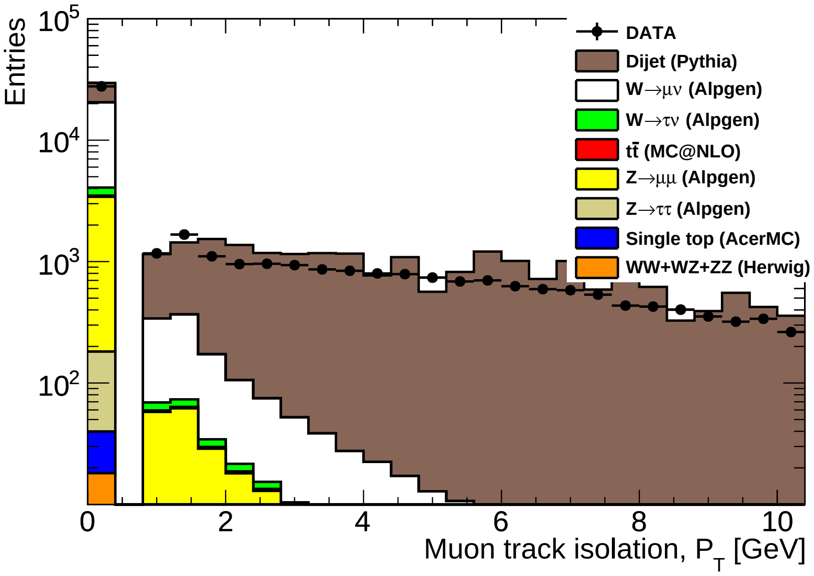

Figure 5.9: *Control plot showing the distribution of track-based isolation, PtCone30, of muon candidates from Monte Carlo simulation and data.*

5.3.3 Jet selection

Jets are reconstructed with the anti-kt jet reconstruction algorithm with parameter R=0.4 by combining topological clusters in the calorimeters (see Chapter 4.3 for more details). The clusters are calibrated at the electromagnetic energy scale. The jets are then calibrated to the hadronic energy scale, using p_T and η dependent correction factors obtained from Monte Carlo simulation.

In the analysis a minimum transverse momentum of 25 GeV is required on the jets. The choice is driven by two main reasons.

The first is that in the simulation there is a point where the partons in the matrix element of the hard subprocess are matched to the parton shower Monte Carlo simulation. This matching is usually done with a minimum transverse momentum threshold, typically around 10 to 20 GeV. Choosing a reconstructed jet momentum cut right at the matrix element to parton shower matching momentum threshold is theoretically not advisable. Such a choice can make the results of any analysis very sensitive to the matching parameters.

The other reason is that the jets in the final state of top quark pair production have higher momenta than the jets in other background processes. This is because the energy scale of a top quark pair event is higher, there are two massive top quarks involved, each with 170 GeV of mass. Therefore increasing the jet p_T threshold upwards, from say 20 GeV, it is expected to improve the signal to background ratio. The results of optimization studies for maximal top signal significance[1], however, suggested not to increase the minimum jet momentum to higher than 25 GeV because it would lead to an unacceptable loss in the signal yield.

The jet reconstruction efficiency can also be studied to make a reasonable choice on the jet transverse momentum threshold. Here the jet reconstruction efficiency is defined as the ratio of the number of full detector simulated and reconstructed anti-$\mathrm{k_T}$, $R = 0.4$, jets that are matched to any true *particle*

---

[1] Significance is defined in this section as signal over square-root of signal plus background, $\Sigma = S/\sqrt{S+B}$.

jet[2] to the number of all particle jets. The matching is done with a cone of $\Delta R = 0.2$. Figure 5.10 shows the jet reconstruction efficiency as a function of the transverse momentum of the true particle jet using $W \rightarrow \mu\nu$+jets ALPGEN [32] events. The jet reconstruction efficiency distribution shows a threshold at 20 GeV. A choice of 25 GeV minimum cut on the jet transverse momentum is already in the plateau region of the efficiency curve. A cut on

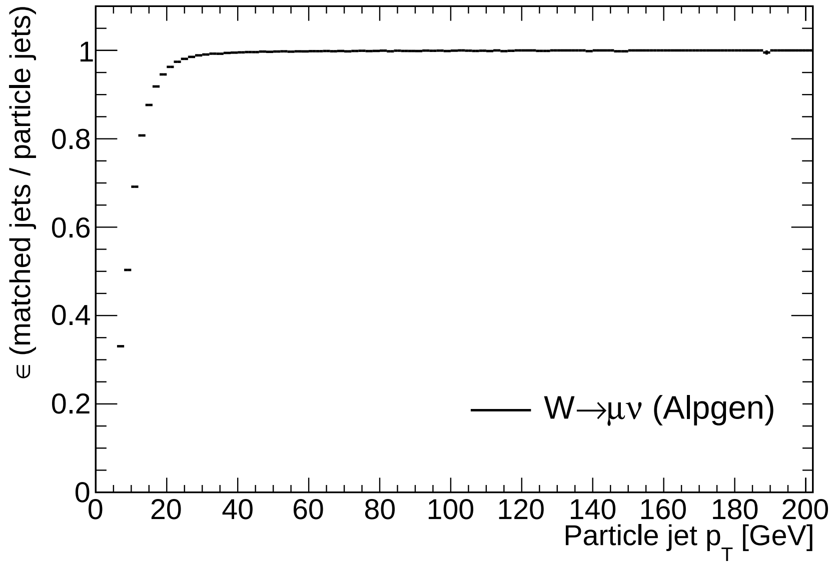

Figure 5.10: *Jet reconstruction efficiency of full simulated anti-*$\mathrm{k_T}$*,* $R = 0.4$*, jets with respect to true particle jets as a function of the transverse momentum of the particle jet from Monte Carlo simulation, using* $W \rightarrow \mu\nu$*+jets Alpgen events.*

the pseudorapidity of the jet, $|\eta| < 2.5$, is used to select jets from the central region of the detector where all the detectors provide good acceptance.

During the jet finding and reconstruction from calorimeter cells, the reconstruction algorithm cannot distinguish between calorimeter signals from isolated electrons and other jet constituent electromagnetic particles. This can lead to the situation that a true electron is reconstructed both as an electron candidate and as a jet. The *overlap* of a jet with an electron is defined based

---

[2] Particle jets are jets reconstructed with the cone algorithm with parameter $R = 0.4$. The particle jets are formed after the simulation of hadronization, but before the detector simulation, therefore all detector effects are removed when using them.

on the corresponding distance, $\Delta\mathrm{R}(\mathrm{electron} - \mathrm{jet})$, between them. If the distance is less than 0.2 the jet is removed from the event in order to avoid double-counting electrons as jets. The motivation for the cut value is on similar grounds as for the muon-jet separation cut, and is illustrated on Fig 5.11. The reason for the cut to a narrower volume, $\Delta\mathrm{R}(\mathrm{electron} - \mathrm{jet}) < 0.2$ compared to $\Delta\mathrm{R}(\mathrm{muon} - \mathrm{jet}) < 0.4$, used for flagging jets as potentially electrons is the ambiguity between electrons and jets. The rate of electrons faking jets is much higher than for muons faking jets because the rate of bremsstrahlung from muons is negligible with respect to that of the electrons. The impact of muon-jet overlap removal, where suspicious muons are removed, is negligible on the final results. But since the electron-jet overlap removing algorithm removes *jets*, that are primarily used for the analysis, a more conservative choice has been made on their overlap discrimination.

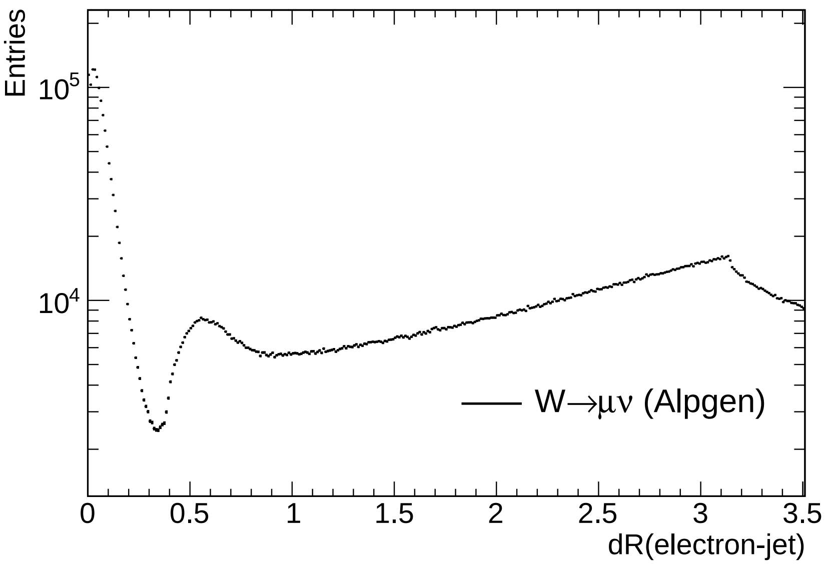

Figure 5.11: *Distribution of the distance,* $\Delta\mathrm{R}(\mathrm{electron} - \mathrm{jet})$*, between reconstructed electron and jet candidates.*

Control plots are presented on Figures 5.12, 5.13 and 5.14 showing the distribution of the pseudo-rapidity, transverse momentum of the leading jets and the multiplicity of jets, respectively. All distributions show good agreement between data and Monte Carlo simulations.

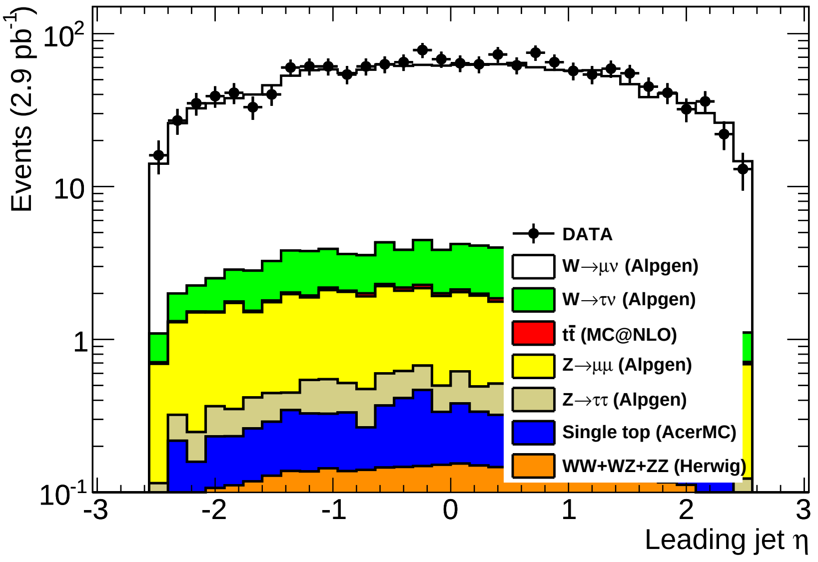

Figure 5.12: *Control plot showing the distribution of pseudo-rapidity of the leading jets from Monte Carlo simulation and data.*

5.3.4 Missing transverse energy discrimination

The missing transverse energy is constructed from the vector sum of all calorimeter cell energies, projected onto the transverse plane. Cells not associated to a jet or electron are included at the electromagnetic scale. Cells associated with jets are taken at the corrected energy scale that was used for jets, while the contribution from cells associated with electrons are substituted by the calibrated transverse energy of the electron. Finally, the contribution from muons is included, also removing the contribution of any calorimeter cells associated to the muon (see Section 4.4 for more details). To select top quark pair and W-like candidate events, the missing transverse energy (E_T^{miss}) is a good discriminator against the pure multijet production. This is illustrated on Figure 5.15 where the reconstructed missing transverse energy distributions are shown for fully simulated inclusive QCD multijet,

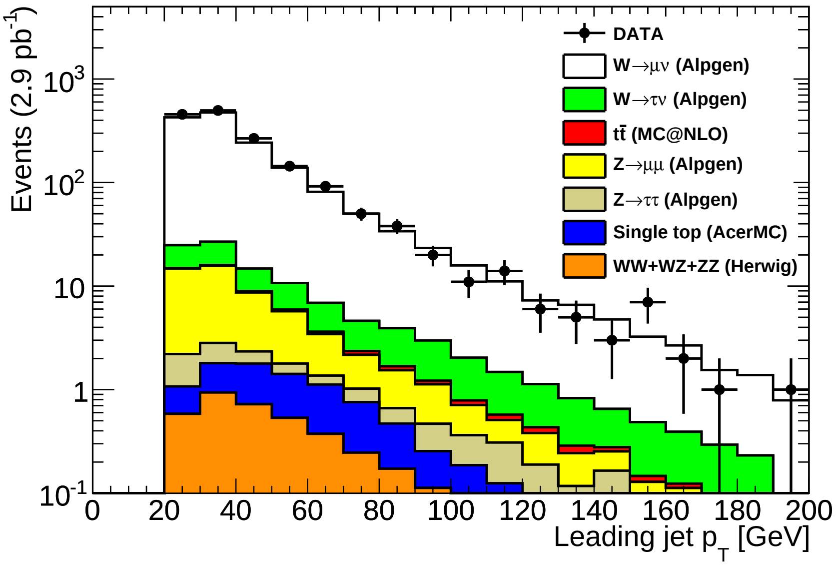

Figure 5.13: *Control plot showing the distribution of transverse momentum of the leading jets in events from Monte Carlo simulation and data.*

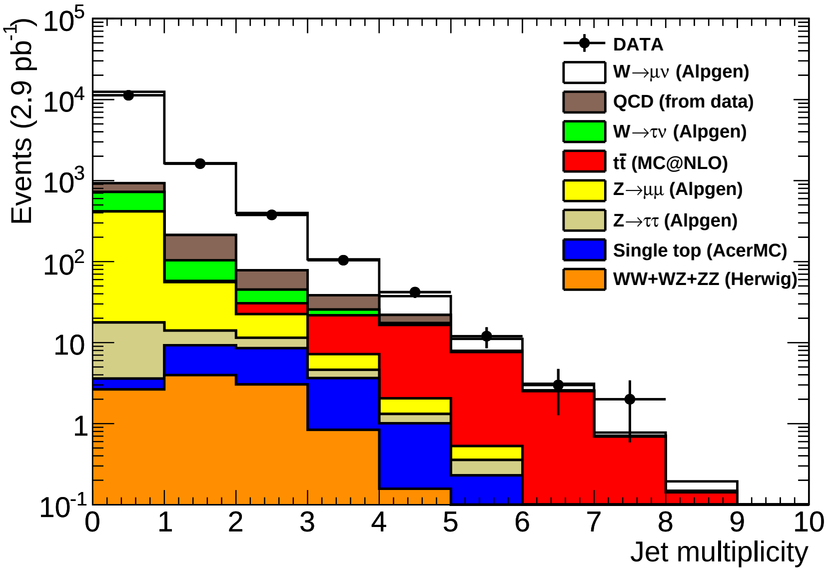

Figure 5.14: *Control plot showing the multiplicity of jets in Monte Carlo simulation and data.*

$W \to \mu\nu$+jets and $t\bar{t}$ events. The histograms are overlayed and normalized to unit area. The discriminator value of 20 GeV seems to be a natural choice to use in the analysis; it clearly separates between the low E_T^{miss} region dominated QCD dijet events. In Figure 5.16 the distribution of E_T^{miss} is presented also, but after the $W \to \mu\nu$+1 jet selection. The plot illustrates that the top signal and the W-like events populate E_T^{miss} regions above 20 GeV and that the QCD multijet background is suppressed by the triangular cut, the distributions are in good agreement between the Monte Carlo simulations and the data - without including the QCD.

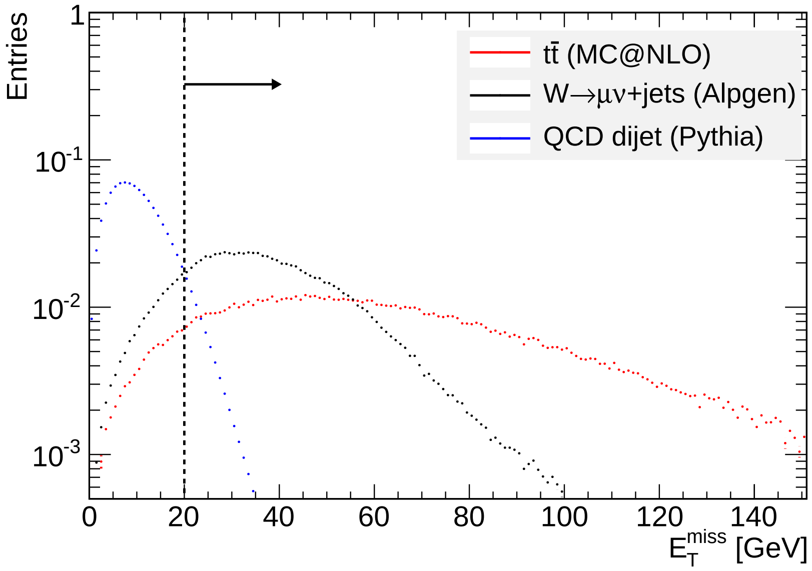

Figure 5.15: *Distribution of missing transverse energy in simulated QCD dijet, W(→ $\mu\nu$)+ jets and top quark pair events. The histograms are normalized to unit area.*

5.3.5 Triangular cut

Discrimination against instrumental QCD background can be done by choosing a suitable variable or variables which exploit the fact that the QCD populates different phase space regions than signal-like $t\bar{t}$ and W+jets events. For QCD events the reconstructed directions of both the missing transverse

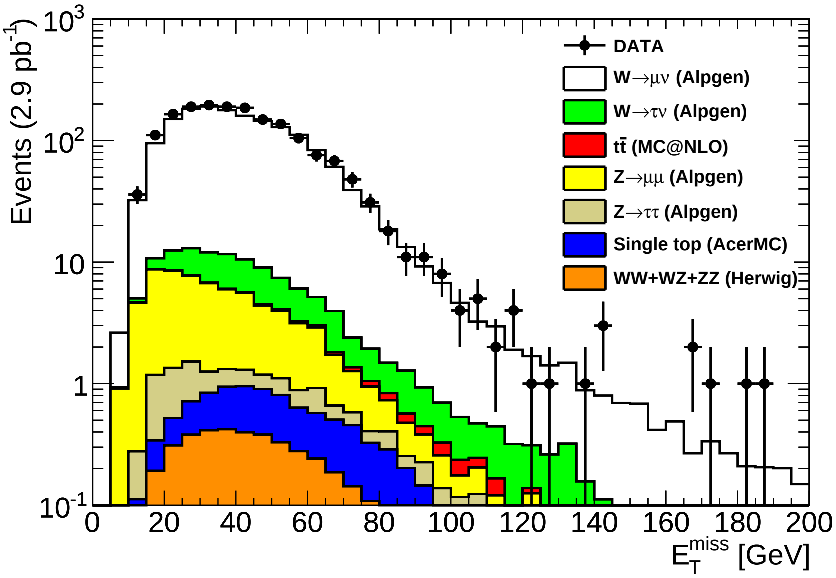

Figure 5.16: *Distribution of missing transverse energy after exclusive $W(\rightarrow \mu\nu)+$ 1 jet candidate selection on data and Monte Carlo.*

energy and the lepton are expected to point into the jet direction. For events with the presence of W bosons the distribution of the reconstructed transverse mass (calculated from the measured missing transverse energy and the lepton transverse momentum) should show peak at the W boson mass, while for QCD events no such peak should be present. We reconstruct the W transverse mass, $M_T(W)$ as follows. Let us denote the four-momenta of the muon and the neutrino by p_μ and p_ν, respectively. Then calculate the invariant mass squared

$$M^2(W) = (p_\mu + p_\nu)^2 = p_\mu^2 + p_\nu^2 + 2p_\mu p_\nu \ . \tag{5.1}$$

Neglecting the lepton masses we arrive at

$$M^2(W) = 2(E_\mu E_\nu - \vec{p}_\mu \vec{p}_\nu) = 2(|\vec{p}_\mu||\vec{p}_\nu| - |\vec{p}_\mu||\vec{p}_\nu| \cos\alpha) \ , \tag{5.2}$$

where α is the angle between the muon and the neutrino. Finally taking only the transverse components:

$$M_T(W) = \sqrt{2p_T^{\mu}p_T^{\nu}(1 - \cos\Delta\phi(\mu,\nu))}\ . \tag{5.3}$$

After selecting events with a single muon the transverse W mass is therefore reconstructed from the muon and the missing transverse energy as

$$M_T(W) = \sqrt{(2p_T^{\mu}E_T^{miss}(1 - \cos\Delta\phi(\mu, E_T^{miss}))}\ . \tag{5.4}$$

The reconstructed transverse mass should therefore discriminate between events with a W boson and multijets. We can use another property of the events in addition: in multijet events the missing transverse energy itself is small because there are no neutrinos from real massive vector boson decays but only from much lighter hadron decays. Therefore the correlation between the reconstructed transverse W mass and the missing transverse energy is investigated for example for QCD and for signal events. Simulation of di-jet events using the PYTHIA event generator and simulation of $t\bar{t}$ events using the MC@NLO event generator was used to produce Figures 5.17 and 5.18. The two distributions differ significantly. The signal-like events populate the two-dimensional $M_T(W) - E_T^{\text{miss}}$ plane at values higher than $M_T(W) > 40$ GeV and $E_T^{\text{miss}} > 20$ GeV. QCD di-jet events populate orthogonally at $M_T(W) < 40$ GeV and $E_T^{\text{miss}} < 20$ GeV. The simple missing energy discrimination, $E_T^{\text{miss}} > 20$ GeV, was already mentioned to be well motivated, but to suppress QCD multijet background even further an additional cut is used, $M_T(W) + E_T^{miss} > 60$ GeV. This is referred to as the triangular cut. The two cuts are illustrated on the two figures and show a reasonable separation between the simulated QCD and signal events.

The impact of the triangular cut on the reconstructed transverse W mass is shown on Figures 5.19 and 5.20. On the stacked plots, the QCD background is indicated with brown color and is the result of the matrix method data-driven QCD background estimation, the details of which are presented in Section 5.5. In the first figure the triangular cut is not applied and therefore there is a large QCD contamination towards low $M_T(W)$ values. In the second figure the triangular cut is applied. The dominant signal contribution is untouched, while the QCD background is almost completely suppressed.

In this analysis, both event selection scenarios, selection with and without triangular cut, are used. The reason is that although the QCD is suppressed by the triangular cut, it is still not reduced completely. One cannot neglect the QCD contamination in the signal region, so even if it is suppressed the analysis has to be able to estimate it. In the end of the analysis it turns out that even with the triangular cut the inclusive 4-jet selection has a significant QCD background contamination. Therefore, as mentioned before, an important cross-check on the result of the thesis is if both approaches lead to the same results.

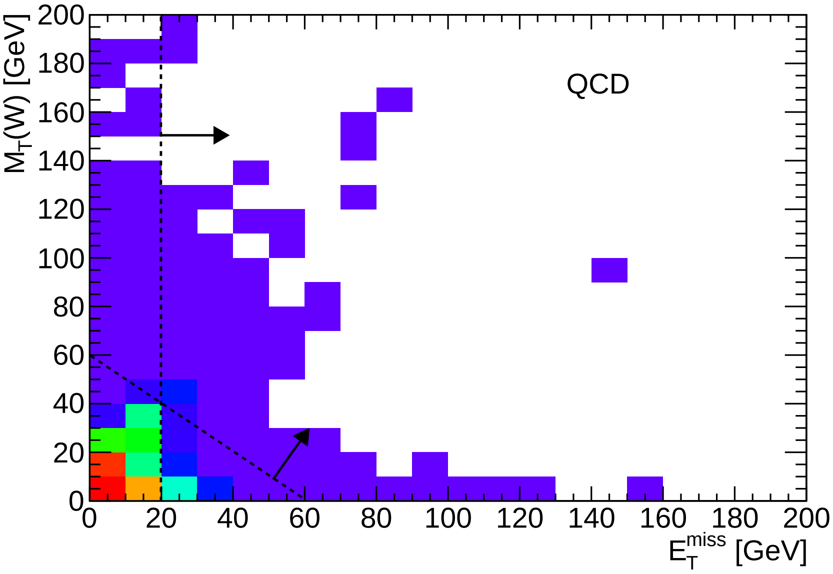

Figure 5.17: *Correlation between reconstructed transverse mass of the* μ-E_T^{miss} *system and the transverse missing energy from simulated QCD background events.*

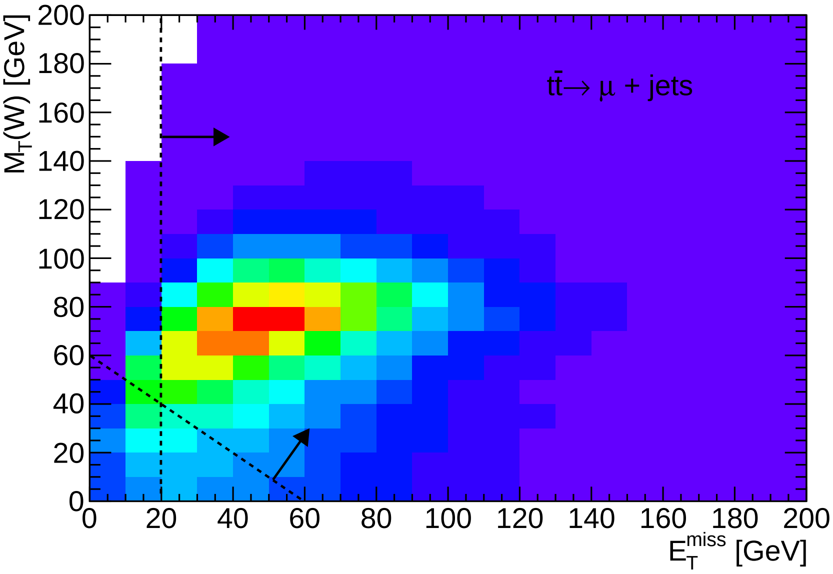

Figure 5.18: *Correlation between reconstructed transverse mass of the* μ-E_T^{miss} *system and the transverse missing energy from simulated* $t\bar{t}$ *signal events.*

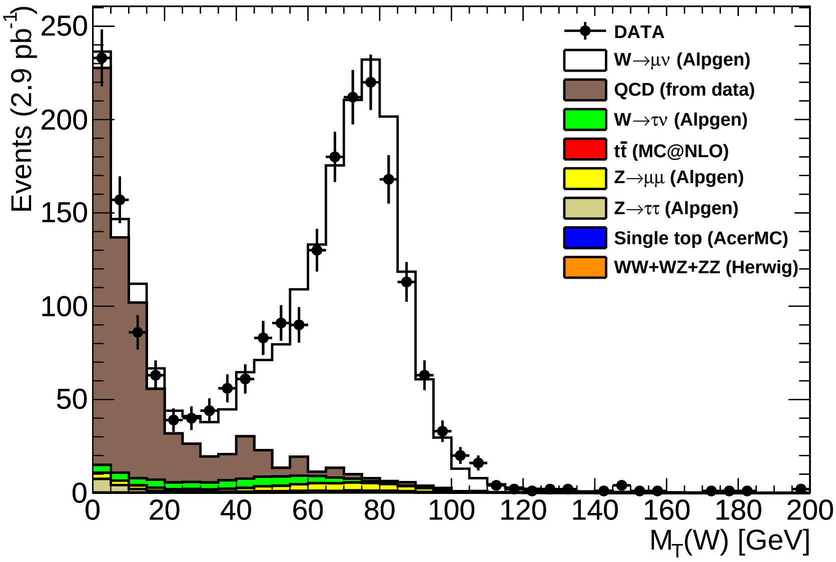

Figure 5.19: *Distribution of reconstructed transverse mass after exclusive* $W \rightarrow \mu\nu +$ *1 jets candidate selection before the triangular cut, for data and Monte Carlo.*

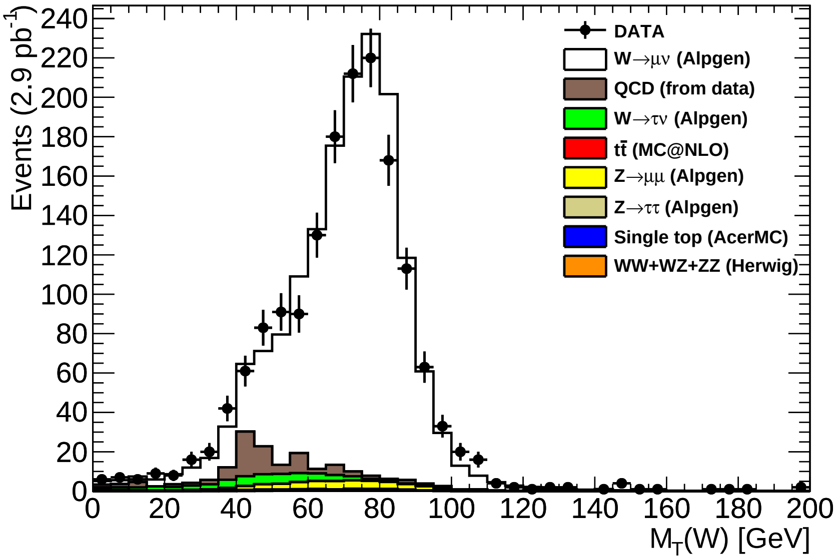

Figure 5.20: *Distribution of reconstructed transverse mass after exclusive* $W \rightarrow \mu\nu +$ *1 jet candidate selection with the triangular cut, for data and Monte Carlo.*

5.3.6 Pile-up sensitivity

During the analysis at the LHC there were $\mathcal{O}(10^{11})$ protons per bunch per proton beam with bunch spacing of 1000 ns. The peak luminosity during the analysis of the current data was $\sim 3 \times 10^{31}$ cm^{-2}s^{-1}. Assuming an average total proton-proton cross section of $\sim 8 \times 10^{8}$ nb $= 8 \times 10^{-25}$ cm^2 one expects on average 1 proton-proton interaction per bunch crossing. The presence of more than one interaction in the *same* bunch crossing is called *pile-up*. With continuously increasing luminosity, the impact of pile-up effects can become real. In case of pile-up, one expects an increase in the number of reconstructed vertices per event. It is also expected that there is a hardest subprocess and a corresponding primary vertex, while the additional vertices are due to the pile-up interactions. As a result, the number of tracks in the reconstructed vertices of pile-up events are expected to be smaller than that of the hardest subprocess. One can construct a variable, with the use of jets and their associated tracks, which is sensitive to the presence of pile-up. The *Jet Vertex Fraction* (JVF) [46] is the fraction of each jet's constituent transverse track-momentum contributed by each vertex. Tracks are matched to each jet with $\Delta R(\text{track}, \text{jet}) \leq 0.4$. The general definition of JVF is then as follows

$$\text{JVF}(\text{jet}_i, \text{vtx}_j) = \frac{\sum_k p_T(\text{trk}_k^{\text{jet}_i}, \text{vtx}_j)}{\sum_n \sum_l p_T(\text{trk}_l^{\text{jet}_i}, \text{vtx}_n)} \; , \tag{5.5}$$

which gives the JVF for a single jet, jet_i, with respect to a vertex, vtx_j, in the event by summing up the p_T of all matched tracks from the given vertex divided by the total jet-matched tracks' p_T from all vertices. The JVF in this analysis is used to refer to the fraction of matched track momentum from the identified hard-scatter vertex, which is defined to have the maximum sum p_T from all associated tracks. In Fig. 5.21 the distribution of the reconstructed JVF is shown for all jets in the data after requiring the non-collision background rejection cut (see next section). Three regions can be distinguished in the distribution: jets without matched tracks but which are still within the fiducial region (JVF$= -1$ by initialization), jets originating from pile-up collisions (JVF$= 0$), hard-scatter jets with some contribution from pile-up collisions ($0.5 \leq \text{JVF} \leq 1.0$). The sensitivity of an analysis result to pile-up can be studied by cutting on the JVF and searching for any deviation from the nominal values. When the pile-up sensitivity will be discussed in Section 5.6.5 and Chapter 6 a discrimination cut on the jets for $|\text{JVF}| > 0.75$ will be used to consider only jets from pure hard-scatter vertex and therefore with reduced pile-up.

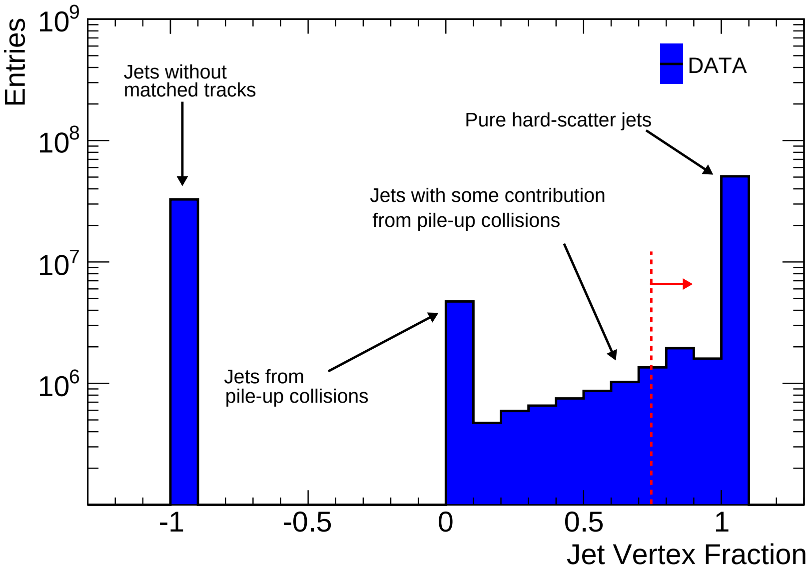

Figure 5.21: *Reconstructed Jet Vertex Fraction with respect to the selected primary vertex for all jets in the data.*

5.4 Object and event selection summary

In this section the object and event selections of the analysis are summarized. There are two analysis scenarios applied in parallel in the thesis: the two approaches have a common set of base selections, they only differ in the use of the triangular cut. The reconstructed object selections are summarized in Table 5.1. The event selection is shown in Table 5.2 and Table 5.3. The two tables show the Monte Carlo expectations for the number of events at 2.9 pb^{-1} integrated luminosity, after each selection cut inclusively and in each different jet multiplicity bin for signal and background processes, for the analysis approach without and with the triangular cut, respectively. The uncertainties on the numbers in the tables are below one percent and are due to the Monte Carlo statistics. The signal regions in the tables, the inclusive 4 jet selection columns, are highlighted. From the tables one can conclude that in the final signal region the signal event yield is expected to be the same for the two analysis approaches. The only difference is expected to be the amount of QCD background contamination in the signal region and the size of its uncertainty. The QCD background expectation is not shown in the table because it is estimated from the data in the next section.

Table 5.1: *Summary of object selection cuts used in the analysis.*

Selection	Value
Number of tracks in any vertex candidate	≥ 5
Trigger	L1_MU10, EF_mu10_MSonly
Muon type	combined
Muon-jet overlap, ΔR	≥ 0.4
Muon calorimeter isolation, R=0.3	< 4 GeV
Muon track isolation, R=0.3	< 4 GeV
Muon p_T	> 20 GeV
Muon $\lvert\eta\rvert$	< 2.5
Jet type	anti-k$_T$, $R = 0.4$
Jet-electron overlap, ΔR	≥ 0.2
Jet p_T	> 25 GeV
Jet $\lvert\eta\rvert$	< 2.5

Table 5.2: *Expected number of events at 2.9* pb^{-1} *from full Monte Carlo simulation of the various signal and background processes, without the triangular cut. The number of events from left to right are after the cumulative cuts. For the jet multiplicities they are understood separately.*

Process	Trigger	1 muon	$E_T^{\mathrm{miss}} > 20$ GeV	1 jet	2 jets	3 jets	$\geq$ **4 jets**
$t\bar{t}$	96	59	52	1.9	8.5	15	**26**
$W \rightarrow \mu\nu$+jets	17500	14700	13500	1482	334	72	**20**
$W \rightarrow \tau\nu$+jets	1527	521	400	62	18	4.6	**1.4**
$Z \rightarrow \mu\mu$+jets	2355	906	477	53	14	3.3	**1.2**
$Z \rightarrow \tau\tau$+jets	307	122	45	18	7.1	2.1	**0.7**
Single top	28	19	17	5.7	5.8	2.9	**1.1**
Diboson	19	13	11	4.2	3.2	0.9	**0.2**

5.5 QCD background estimation

Estimation of the instrumental QCD background for the control and signal regions, with $E_T^{\mathrm{miss}} > 20$ GeV, in the data cannot be done using only Monte Carlo simulations, because the cross section of the multiparton production is so huge that it is virtually impossible to generate enough events to predict the shapes of the distributions from multijet processes with sufficient precision in the signal region. The physical reason is that the leptonic decays of massive vector bosons in the $t\bar{t}$ or W+jets events produce large values of missing transverse energy in the detector and isolated muons with high transverse momenta while multijet QCD-like events generally produce leptons with low p_T and low energy neutrinos which subsequently produce low transverse missing energy. However, the cross section of multijet production is so large that the high transverse momentum and high missing transverse energy tail regions produce a non-negligible contamination in the signal and control regions.

Table 5.3: *Expected number of events at 2.9* pb^{-1} *from full Monte Carlo simulation of the various signal and background processes, with the triangular cut. The number of events from left to right are after the cumulative cuts. For the jet multiplicities they are understood separately.*

Process	trigger	1 muon	$E_T^{\mathrm{miss}} > 20$ GeV	Triangular cut	1 jet	2 jets	3 jets	$\geq$ **4 jets**
$t\bar{t}$	96	59	52	49	1.8	8.1	15	**25**
$W \rightarrow \mu\nu$+jets	17500	14700	13500	13400	1428	320	68	**19**
$W \rightarrow \tau\nu$+jets	1527	521	400	373	46	14	3.8	**1.2**
$Z \rightarrow \mu\mu$+jets	2355	906	477	454	42	11	2.6	**0.9**
$Z \rightarrow \tau\tau$+jets	307	122	45	23	4.8	2.9	1.0	**0.5**
Single top	28	19	17	16	1.8	5.5	2.8	**1.1**
Diboson	19	13	11	10.6	4.0	3.0	0.8	**0.2**

5.5.1 Matrix method

The method to estimate the QCD background rate is called the *matrix method*. It is based on the assumption that the shape of the E_T^{miss} distribution is approximately independent of the tightness of the muon quality cuts. To utilize the method we define *tight* muons as described in Section 5.3.2, while *loose* muons are defined as tight except removing the calorimeter and track based cone isolation cuts. The triangular mass cut is not used in the selections in order to enhance the amount of data with QCD-like events. Loosening and tightening the muon isolation enriches and depletes the QCD background in the sample of the selected events. At the same time it is also expected that it will not affect the signal-like events because for the signal there is at least one well isolated muon: after loosening the muon isolation the same event will still survive the selection cuts. One can then write the following equations:

$$N^{\text{loose}} = N_{\text{fake}}^{\text{loose}} + N_{\text{real}}^{\text{loose}} \tag{5.6}$$

$$N^{\text{tight}} = \epsilon_{\text{fake}} \cdot N_{\text{fake}}^{\text{loose}} + \epsilon_{\text{real}} \cdot N_{\text{real}}^{\text{loose}}, \tag{5.7}$$

where N^{loose} is the number of events after all cuts with loose muon selection, while N^{tight} is the number of events after all cuts with tight muon selection using the *same* muon for both loose and tight selection, $\epsilon_{\text{fake}} = N_{\text{fake}}^{\text{tight}}/N_{\text{fake}}^{\text{loose}}$ is the ratio of tight to loose events for QCD-like events which produce fake (or non-prompt) muons, and $\epsilon_{\text{real}} = N_{\text{real}}^{\text{tight}}/N_{\text{real}}^{\text{loose}}$ is the ratio of tight to loose events for the signal-like events producing real muons. One expects ϵ_{real} to be close to one, as it mainly contains real isolated muons. It can be estimated from a Monte Carlo simulation of $Z \to \mu\mu$ and $W \to \mu\nu$ events. The value of ϵ_{fake} is measured from data using a fake or non-prompt muon enriched sample. The QCD-enhanced sample is created by selecting events with low missing transverse energy. As mentioned before, these events are expected to be populated mainly by QCD multijet processes, this was shown in Figure 5.15. The solution to the system of equations yields the estimated number of QCD-like fake events in the signal region, $N_{\text{fake}}^{\text{tight}}$, as

$$N_{\text{fake}}^{\text{tight}} \equiv \epsilon_{\text{fake}} \cdot N_{\text{fake}}^{\text{loose}} = \frac{\epsilon_{\text{fake}}}{\epsilon_{\text{real}} - \epsilon_{\text{fake}}} (N^{\text{loose}} \cdot \epsilon_{\text{real}} - N^{\text{tight}}) \tag{5.8}$$

where one measures again N^{loose} and N^{tight} from the data, estimates ϵ_{fake} with the measured value at low E_T^{miss} in the data and finally ϵ_{real} is estimated from Monte Carlo simulations of signal-like events with high statistics[3].
Note that the important factor for the number of fake leptons in the tight selection is actually just

$$f(\epsilon_{\text{fake}}, \epsilon_{\text{real}}) = \frac{\epsilon_{\text{fake}} \cdot \epsilon_{\text{real}}}{\epsilon_{\text{real}} - \epsilon_{\text{fake}}} \ , \tag{5.9}$$

and also note that $N^{\text{tight}} \cdot \epsilon_{\text{real}} \approx N^{\text{tight}}$ because $\epsilon_{\text{real}} \approx 1$. Therefore the total number of fakes in a tight selection in general can be appoximated as

$$N_{\text{fake}}^{\text{tight}} = f(\epsilon_{\text{fake}}, \epsilon_{\text{real}}) \cdot (N^{\text{loose}} - N^{\text{tight}}). \tag{5.10}$$

As a consequence the factor, $f(\epsilon_{\text{fake}}, \epsilon_{\text{real}})$, can be interpreted as a weight factor for the measured $N^{\text{loose}} - N^{\text{tight}}$ events in the data. Hence, after the estimation of $\epsilon_{\text{fake}}(\xi, \dots)$ and $\epsilon_{\text{real}}(\xi, \dots)$ as a function of some relevant variables, the distribution of the fakes in the tight sample can be obtained by re-weighting each data event in a loose-with-tight-veto selection with a proper event weight factor, $f(\epsilon_{\text{fake}}(\xi, \dots), \epsilon_{\text{real}}(\xi, \dots))$.
The main question is therefore what are the results on the estimation of ϵ_{fake} and ϵ_{real}. Monte Carlo distributions were studied to estimate the stability and the separation of ϵ_{fake} and ϵ_{real} as a function of the transverse missing energy and muon transverse momentum. Although the QCD events cannot be simulated well for high missing transverse energy or high muon transverse momentum, the general stability can be studied up to ~ 50 GeV. A mixture of various processes from simulated multiparton production, using the ALP-

---

[3] The name “matrix method” originates from the generalization of the method. In the general case even more unknowns and equations can be constructed and can be written up in a vector-matrix form. The inversion of the matrix of coefficients, containing the efficiencies, gives the solution for the vector of unknowns in general.

GEN event generator, was used to create a pseudo-data sample, referred to as *TopMix QCD*, for QCD-like events. For the simulation of signal-like $W \to \mu\nu$ and $Z \to \mu\mu$ events, producing isolated muons from decay of massive particles, the ALPGEN event generator has been used as well. Both samples have been run through full detector simulation. The results are shown on Figure 5.22 and Figure 5.23. The two plots show the ratio of events with tight and loose muon selection as a function of the missing transverse energy of the events and the transverse momentum of the single muon. The error bars on the plots are only the Monte Carlo statistical uncertainties. The figures illustrate that the basic assumption, that the shape of the missing transverse energy distribution is to first order independent of the tightness of the muon quality cuts, is true. One can conclude also that there is a clear separation in ϵ(tight/loose) between QCD-like events with fake and non-prompt muons, and signal-like events with real isolated muons. Within the statistical uncertainties the ϵ(tight/loose) is in general stable as a function of the missing transverse energy and the muon transverse momentum.

As mentioned above, we expect ϵ_{real} to be close to 1, by construction, therefore in the analysis the ϵ_{real} values are measured from the Monte Carlo simulations of $Z \to \mu\mu$ events, because in the data the measurement from $Z \to \mu\mu$ events is limited by statistics given the current data sample size. For ϵ_{fake} the same approximation cannot be done. Measured values for ϵ(tight/loose) at low missing transverse energy are shown as follows. The behaviour of ϵ(tight/loose) at low missing transverse energy region is as expected, see Figure 5.24. It is stable and much lower than 1. The dependence of ϵ(tight/loose) on the muon transverse momentum, see Figure 5.25, in selected events with $E_T^{\mathrm{miss}} < 10$ GeV, cannot be used directly for the parametrization of the fake rates from the data at high muon transverse momentum, because this variable is sensitive to the presence of signal. Massive boson decays produce muons with high transverse momenta. Therefore ϵ(tight/loose) increases towards the high muon momentum regions where the data will be “contaminated” with real muons and subsequently ϵ(tight/loose) increases up to 1. Looking at the ϵ(tight/loose) dependence on the pseudorapidity of the muon candidates, see Figure 5.26, measured at $E_T^{\mathrm{miss}} < 10$ GeV, a satisfying stability is found. Therefore for the analysis it was decided to use the muon pseudorapidity for the parametrization of ϵ(tight/loose).

The matrix method event re-weighting technique results are summarized in Table 5.4 for the two control regions and for the signal region, and for applying and not applying the triangular cut. The missing transverse energy distributions, including the QCD estimate from the matrix method, are shown in Figures 5.27 and 5.28 without triangular cut, and Figures 5.29 and 5.30 with triangular cut applied. There is a good agreement between the Monte Carlo simulation with the data-driven multijet prediction and the data. In the case when the triangular is not applied the multijet events clearly dominate the low E_T^{miss} region and their contribution falls steeply towards higher values of missing energy. In the case when the triangular cut is applied the QCD contribution in the low E_T^{miss} region is largely suppressed but at around 20 GeV the tail of the multijet contamination is still visible and gives a significant but decreasing contamination to the $W \rightarrow \mu\nu$ + 1jet candidates as a function of the missing transverse energy. The results obtained in the data-driven estimation of multijet background are directly used in the $W \rightarrow \mu\nu$ + 1jet, $W \rightarrow \mu\nu$ + 2jets exclusive and $W \rightarrow \mu\nu$ + 4jets inclusive selections.

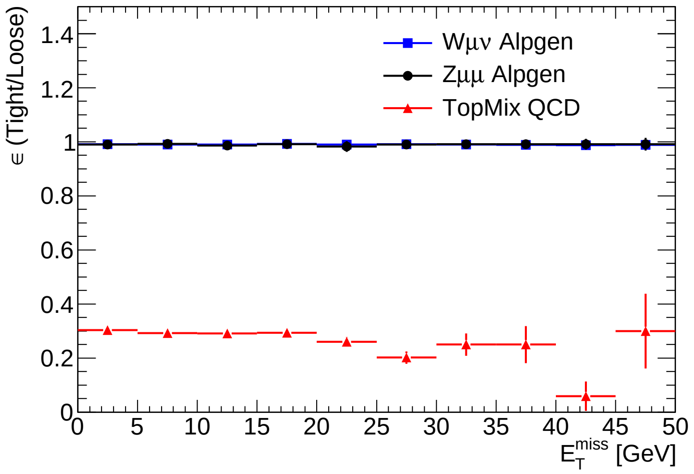

Figure 5.22: *Ratio of the number of tight to loose events as a function of the transverse missing energy for signal-like and QCD-like simulated events.*

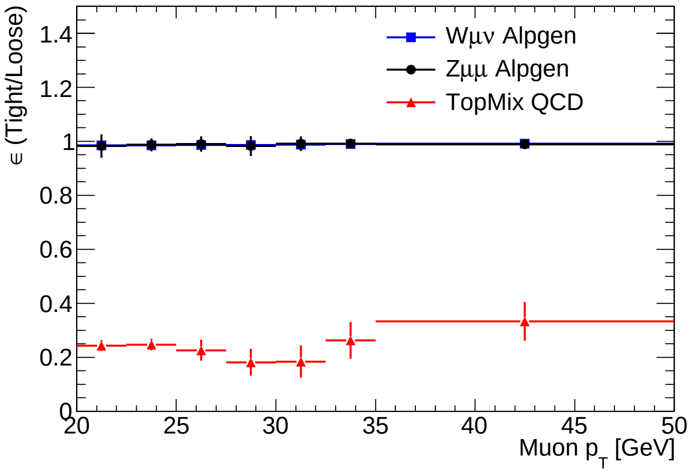

Figure 5.23: *Ratio of the number of tight to loose events as a function of the transverse momentum of the muon candidates for signal-like and QCD-like simulated events.*

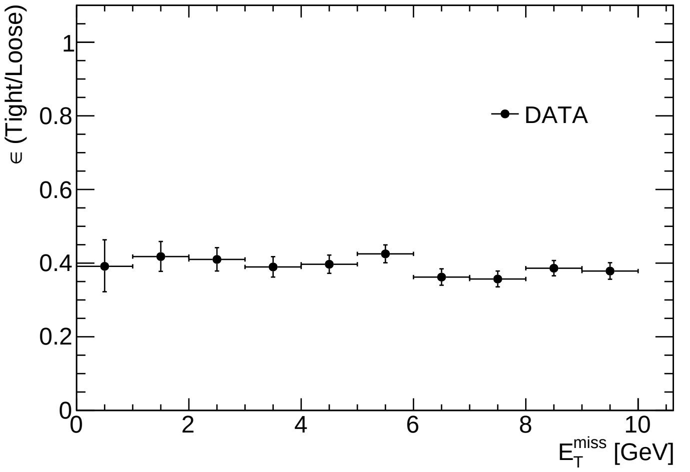

Figure 5.24: *Ratio of the number of tight to loose events as a function of the missing transverse energy in the data.*

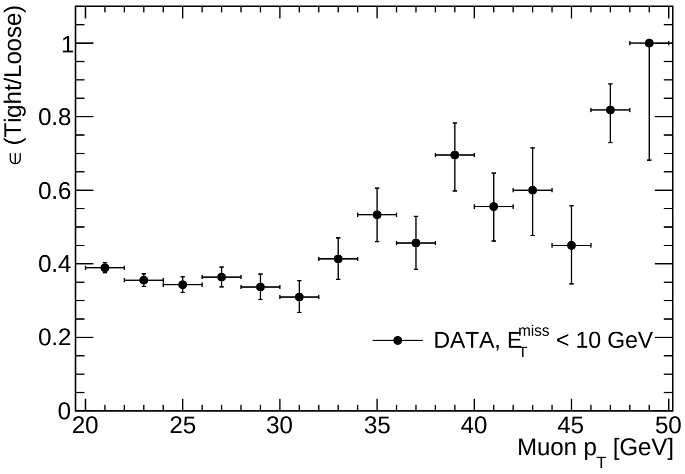

Figure 5.25: *Ratio of the number of tight to loose events as a function of the transverse momentum of the muon candidates in the data for* $E_T^{miss} < 10\ GeV$.

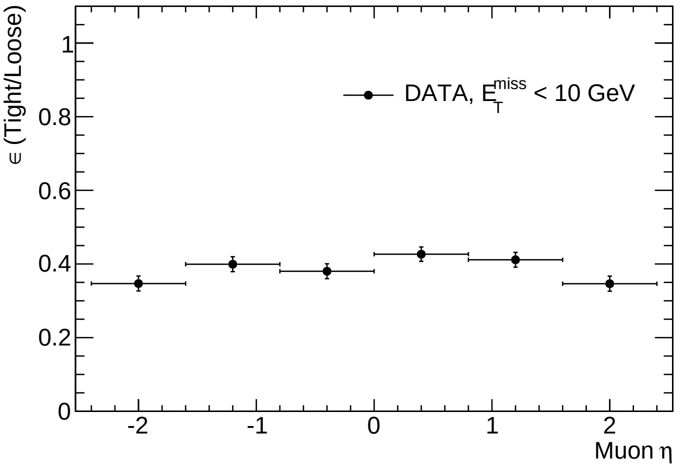

Figure 5.26: *Ratio of the number of tight to loose events as a function of the pseudorapidity of the muon candidates in the data for* $E_T^{miss} < 10\ GeV$.

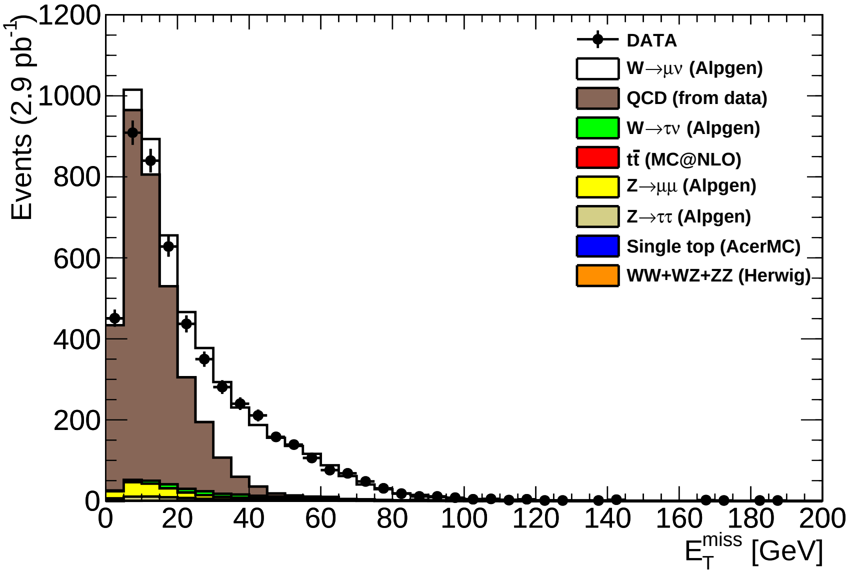

Figure 5.27: *Distribution of missing transverse energy after exclusive $W(\rightarrow \mu\nu)+$ 1 jet candidate selection for data and Monte Carlo.*

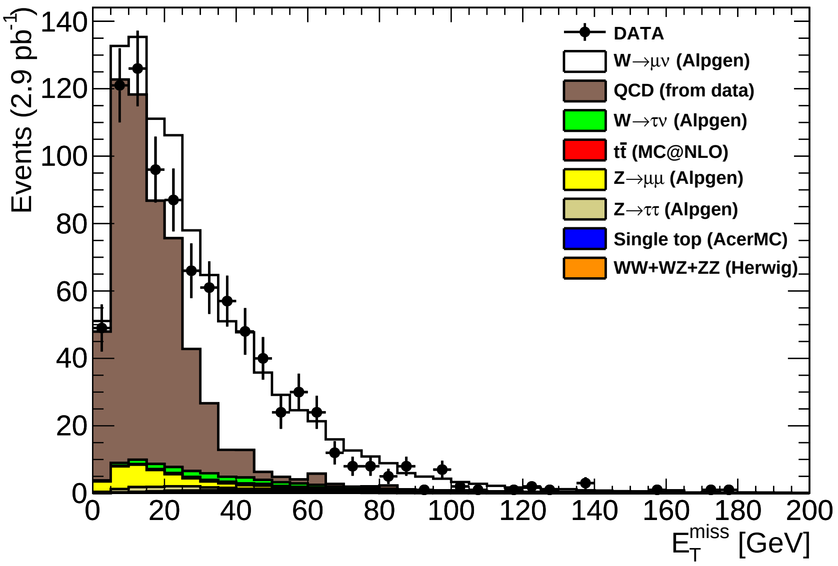

Figure 5.28: *Distribution of missing transverse energy after exclusive $W(\rightarrow \mu\nu)+$ 2 jets candidate selection for data and Monte Carlo.*

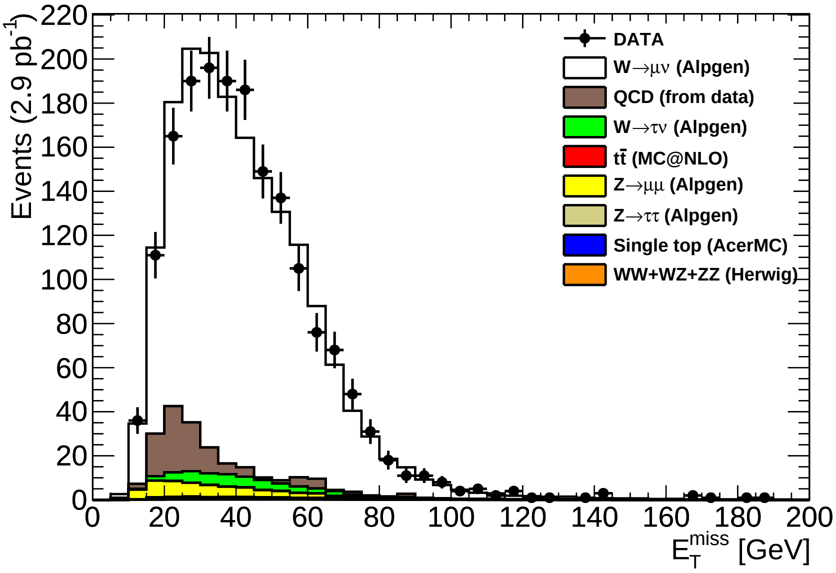

Figure 5.29: *Distribution of missing transverse energy after exclusive W(→ $\mu\nu$)+ 1 jet candidate selection with triangular cut for data and Monte Carlo.*

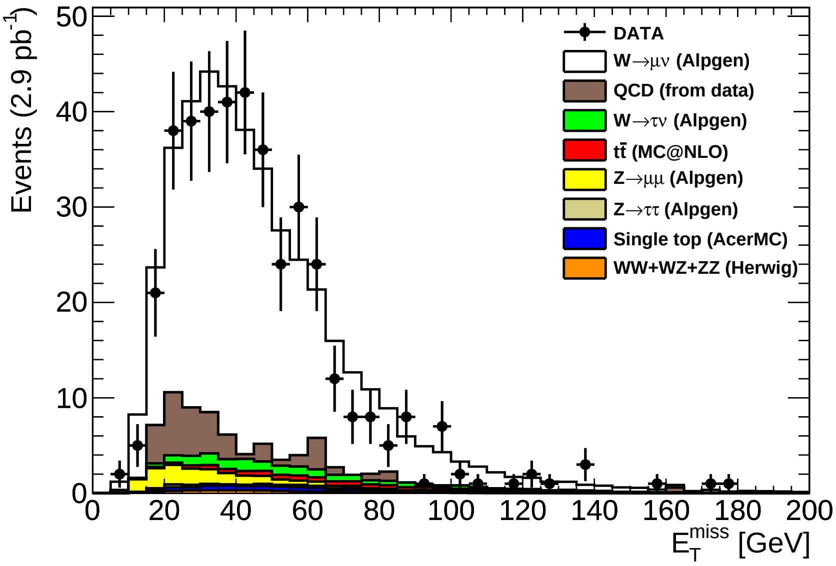

Figure 5.30: *Distribution of missing transverse energy after exclusive W(→ $\mu\nu$)+ 2 jets candidate selection with triangular cut for data and Monte Carlo.*

5.5.2 Uncertainties of the QCD background estimation

The statistical uncertainty of the method originates from the counting of N^{loose} and N^{tight} events in the data. Additional to the statistical uncertainty there are three sources of systematics to consider when estimating the total uncertainty on the QCD estimates: estimation of ϵ_{real}, estimation of ϵ_{fake} and whether the method can reproduce the correct fake rates from a known mixture of fake and real leptons (consistency).

It is expected that the ϵ_{real} for signal events, or real muons, is well approximated by the Monte Carlo simulations. Measuring ϵ_{real} from the Monte Carlo simulation may be slightly biased and the true efficiency in the data might be slightly different. However, ϵ_{real} is a ratio of two numbers, therefore the small biases expected are reduced when taking ratios. Unfortunately at low integrated luminosity the measurement of $Z \rightarrow \mu\mu$ events in the data is limited by statistical uncertainties while the Monte Carlo statistical uncertainties are negligible. Also, the method itself is not sensitive on a few percent changes in ϵ_{real}.

Measurement of ϵ_{fake} happens from data. Therefore it is the best estimate of the fakes by construction. Signal contamination at low E_T^{miss} (from $Z \rightarrow \mu\mu$ events) may present a bias in measuring ϵ_{fake} at low missing transverse energy. A Monte Carlo based study showed that the method's results stay within 10 % of their nominal value when correcting the measured ϵ_{fake} in the Monte Carlo with a factor weighting the relative deviation from the true ϵ_{fake}.

Studies have been done to reproduce the known simulated fake rates in a mixture of Monte Carlo samples consisting of both fake and real lepton events. This approach can test the performance of the method. In general the known fake rates were reproduced within a 10-20% uncertainty (without the signal correction mentioned before).

Therefore an overall conservative 30% systematic uncertainty is used for the total uncertainty of the matrix method on top of any statistical uncertainties on the observed N_{loose} and N_{tight}.

Table 5.4: *Value of tight and loose events measured from the data in low and high missing transverse energy regions as a function of the jet multiplicity, with and without the triangular cut.*

Variable	1 jet	2 jets	$\geq$ 4 jets
N^{loose}, $E_T^{miss} < 10$ GeV	3985 ± 63	483 ± 22	15 ± 4
N^{tight}, $E_T^{miss} < 10$ GeV	1552 ± 39	193 ± 14	7 ± 3
N^{loose}, $E_T^{miss} > 20$ GeV	3222 ± 57	749 ± 27	80 ± 9
N^{tight}, $E_T^{miss} > 20$ GeV	2222 ± 47	500 ± 22	68 ± 8
N_{fake}^{tight}, w/o triangular cut	627 ± 190	152 ± 47	8.5 ± 3.9
N_{fake}^{tight}, with triangular cut	87 ± 28	29 ± 10	3.7 ± 2.2

5.6 Data-driven estimation of W+jets background

The Monte Carlo predictions for the absolute rate of W events which are produced in association with four (or more) energetic jets, populating the same region as the top signal, have a large uncertainty in general. Both the theoretical and experimental reason is the sensitivity of the overall W+jets rate on the matrix element to parton shower matching parameters (theory) or jet energy scale (experiment) variations, especially in case of high jet multiplicity. The idea is to measure a theoretically better understood *ratio* of cross sections of vector boson production and, using the measured value of the ratio, to extrapolate from a control region of W events with low jet multiplicity (the Control Region) into the signal region with high jet multiplicity (the Signal Region). The great advantage of this method is that experimentally numerous uncertainties cancel when taking ratios. The luminosity, lepton trigger efficiency and lepton reconstruction efficiency systematics cancel exactly. The jet energy scale uncertainty either cancels exactly if taking the ratios of rates of the same jet multiplicity but from different vector bosons (W or Z), or reduced. Another advantage is that these are data-driven methods, normalizing event rates to what is measured from the collision data and not using any absolute rate assumption from Monte Carlo event generators. There are various ways to use ratios of vector boson rates. One way is to use the W+jets to Z+jets ratio. The W to Z cross section ratios are predicted with a small uncertainty [47] [48]. The other way is to measure for the same boson the ratio $V + n$ jets$/V + (n - 1)$ jets, which is called the Berends-Giele scaling method [47].

5.6.1 Brief summary of the W/Z ratio method

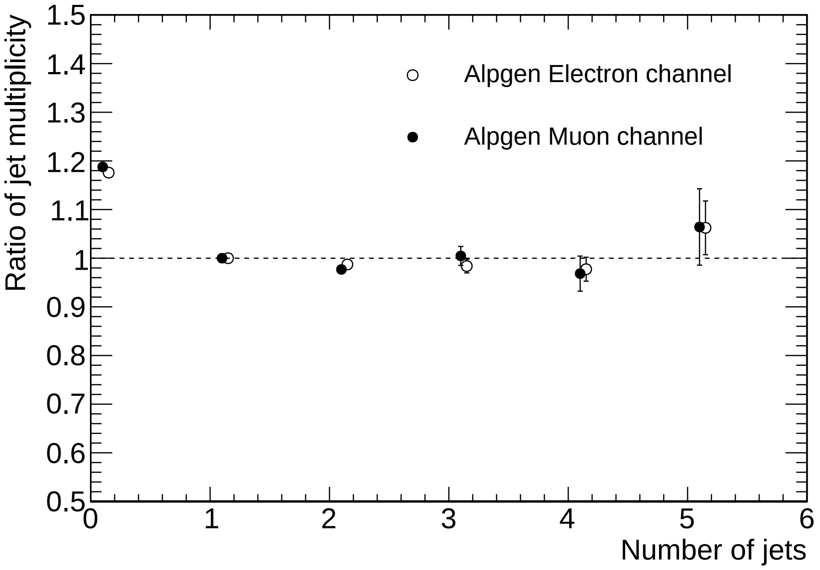

Figure 5.31: *Monte Carlo estimation of the $W + N/Z + N$ jet ratio as a function of the number of jets, N. The ratio is taken after normalization the jet multiplicity distributions for W and Z separately to the one-jet bin.*

Z boson events can be selected with high purity. Selecting two isolated, high p_T muons and requiring that their invariant mass be within 10 GeV of the Z invariant mass already produces an almost background-free Z sample. Since the jet multiplicity distribution for a Z sample can be measured with data, it can be used to reduce the Monte Carlo uncertainty on the fraction of W+jets present in the selected sample of top pair candidates. The physical

assumption here is that the $W+n$ jet/$Z+n$ jet ratio is constant, or stable in general, as a function of the multiplicity of jets. This means that the phase space and production mechanisms for associated jet production is similar for both type of vector bosons. This is illustrated in Figure 5.31 showing the Monte Carlo expectation, using Alpgen events with full detector simulation, for the W/Z ratio after separately selecting W and Z candidates in the electron[4] and muon channel, and taking the ratio of event rates in each jet multiplicity bin. The ratio is normalized such that it is equal to one for the $W+1$ jet and $Z+1$ jet events. The ratio is not strictly constant, in fact it decreases. There is a rather large decrease in the value of the ratio from the 0 jet bin to the 1 jet bin. Towards higher jet multiplicities the ratio is rather constant. This is interpreted in general in such a way that given a ratio for the 0 jet bin case, the rate of an additional one or more jet production is higher for the $Z+$ jets processes because the mass of the Z boson sets the energy scale of the hard subprocess higher than for the $W+$ jets and therefore $Z+$ jets events contain more energy for radiation. As a result the jet rate is expected to be higher for $Z+$ jets events than that for $W+$ jets events.
Unfortunately the Z+jets production cross section is one order of magnitude lower than the W+jets production, see Fig. 2.5 in Section 2.4. As a result the statistical uncertainty on the Z+jets rates limits the precision. Given the amount of data collected at the time of this analysis it was decided not to use the W+jets to Z+jets ratio method but another method which does not relay on having to measure the Z+jets rate, as discussed in the next subsection.

5.6.2 Berends scaling method

The vector boson ratio method used in this analysis is based on the so called Berends-Giele scaling [47]. It has been observed that within the Standard Model, the ratio of cross-sections, $V+n$ jets/$V+(n-1)$ jets, where $V=W$

---

[4] The electron channel selection is identical to the muon channel selection except of requiring tight electrons instead of muons, see Section 4.2 for the details of electron reconstruction.

or Z, is nearly constant as a function of n and it is equal for both W and Z. This is illustrated in Fig 5.32 where Monte Carlo simulation of W+jets and Z+jets events were used to demonstrate the phenomenon. As one can see the stability of the adjacent jet multiplicity ratios are quite clear from $n = 2$. (For $n = 1$ the special ratio of $V + 1$ jet$/V + 0$ jet is taken which involves the 0 jet bin case. The $V + 0$ jet production is a different process than the $V + n$ jets production and in this analysis the 0 jet bin is not used.) As a consequence in this method the number of W events in the Signal Region (that is requiring at least four jets) can be formulated as

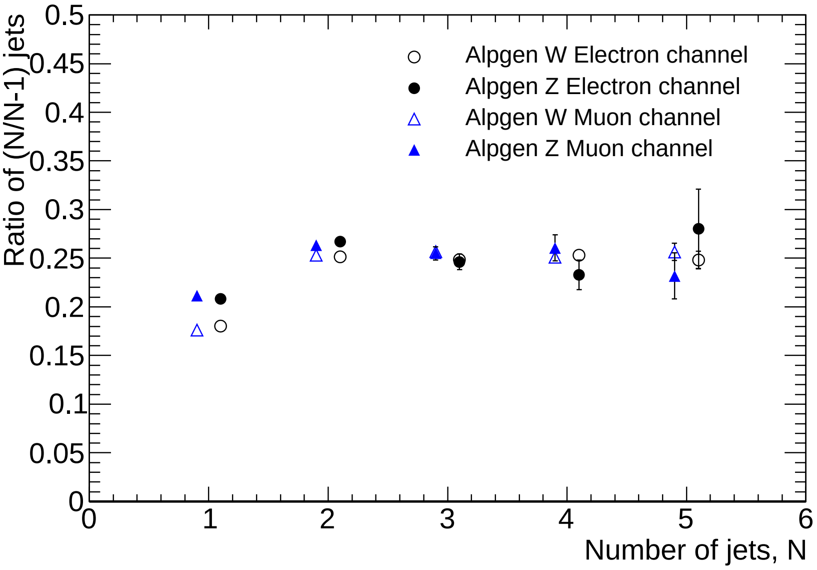

Figure 5.32: *Monte Carlo estimation of the* $V + n\,\mathrm{jet}/V + (n-1)\,\mathrm{jet})$ *ratio, with* $V = W$ *or* Z *boson, as a function of the number of jets,* n*.*

$$W^{\mathrm{SR}} = W^{\mathrm{CR}} \cdot \sum_{i=2}^{\infty} (V^{\mathrm{CR2}}/V^{\mathrm{CR1}})^i = W^{\mathrm{CR}} \cdot \frac{R^2}{1-R} \qquad (5.11)$$

where the sum is taken over jet multiplicity bins, starting at bin $i = 2$, V denotes the rates of either W or Z boson, and subsequently V^{CR2} and V^{CR1} denote rates of candidates events in the Control Regions and $R = V^{\mathrm{CR2}}/V^{\mathrm{CR1}}$. For a proof of the final simplified formula after the last equation

see Appendix A. Having measured a (constant) value of the ratio $V^{\mathrm{CR2}}/V^{\mathrm{CR1}}$ and the rate of W candidates in the CR from the data as a normalization, the integrated total rate of W events in the SR can be extrapolated step-by-step from one jet multiplicity bin to the next one and as a result can be formulated as a sum over increasing power of the ratio of rates in adjacent bins from a starting bin up to infinity. However, care has to be taken when choosing either W or Z as the V boson. As outlined above for the W/Z ratio method the Z sample has the advantage of purity but has much lower cross section, while the W sample is more contaminated but has higher a cross section. In case of the W/Z ratio the W contamination is not reduced when taking the ratio of rates of W and Z in the same jet multiplicity bin, but in case of the Berend's scaling method with $V = W$ the uncertainty on the amount of background contamination is partially reduced in the ratio of rates of V+jets. In addition, the method with $V = W$ enjoys the high statistics from the huge cross section of the W production. Current studies indicate that at high integrated luminosity though, the $V = Z$ case may well give more precise results because of the purity of Z selection.
In this analysis the $V = W$ scenario is used due to the limited amount of Z candidates in the data.

5.6.3 Selection and composition of $W \to \mu\nu$ candidates in the control regions

Distributions of the reconstructed W transverse mass after preselections and without triangular cut are presented on Fig 5.33 and 5.34 for exclusive 1 and 2 jet events, respectively. The same figures with triangular cut applied are shown on Fig 5.35 and 5.36. The QCD multijet background, estimated from the data with the matrix method (see Section 5.5), is also included in the distribution. One can conclude that there is a non-negligible background contamination in the W candidates but the W signal can clearly be seen as a dominant peak in the distributions. If the triangular cut is not applied, in the low W transverse mass region, $M_T(W) = 0 - 20$ GeV, the $W \to$

$\mu\nu$+jet signal-like process is contaminated heavily with processes with low missing transverse energy; typically the largest contribution being QCD, with small contributions from $Z \rightarrow \mu\mu$+jets, $Z \rightarrow \tau\tau$+jets processes present as well. At higher values $W \rightarrow \mu\nu$+jet process dominates while the QCD background decreases (or stays at the same low level if the triangular cut was applied). The number of events counted in the data, the estimated number of background events, and the resulting $W \rightarrow \mu\nu$+1 jet and $W \rightarrow \mu\nu$+2 jet events, compared with the Monte Carlo expectations, are shown in Tables 5.5 and 5.6.

When not applying the triangular cut for both the 1 and 2 jet selections the QCD background was estimated with the matrix method to be at a 30% level. The rate of the other Standard Model backgrounds are estimated form the Monte Carlo simulations. Their estimated fraction is $< 10\%$.

Table 5.5: *Number of events surviving the exclusive W+1 jet selection in the data and the data-driven estimated and expected backgrounds.*

Process	W/o triang. cut	With triang. cut
Total data candidates	2222 ± 47	1618 ± 40
Estimated multijet	627 ± 190	87 ± 28
SM backgrounds	145 ± 29	104 ± 22
Measured $W \rightarrow \mu\nu$+1 jet	1450 ± 198	1427 ± 53
Expected $W \rightarrow \mu\nu$+1 jet	1482	1428

5.6.4 W+jets background estimation in the signal region

For the estimation of the predicted $W \rightarrow \mu\nu + 4$ jets rate the Berends scaling assumption is used (see Section 5.6.2). For the application first the ratio $r = (W + 2 \text{ jets})/(W + 1 \text{ jet})$ is calculated from the results of Tables 5.5 and 5.6 and yields 0.201 ± 0.063 and 0.212 ± 0.024, without and with the triangular cut, respectively, in agreement with the expectations.

Table 5.6: *Number of events surviving the exclusive W+2 jet selection in the data and the data-driven estimated and expected backgrounds.*

Process	W/o triang. cut	With triang. cut
Total data candidates	500 ± 22	377 ± 19
Estimate multijet	152 ± 47	29 ± 10
Estimated SM backgrounds	57 ± 19	45 ± 17
Measured $W \to \mu\nu$+2 jets	291 ± 56	303 ± 28
Expected $W \to \mu\nu$+2 jet	334	320

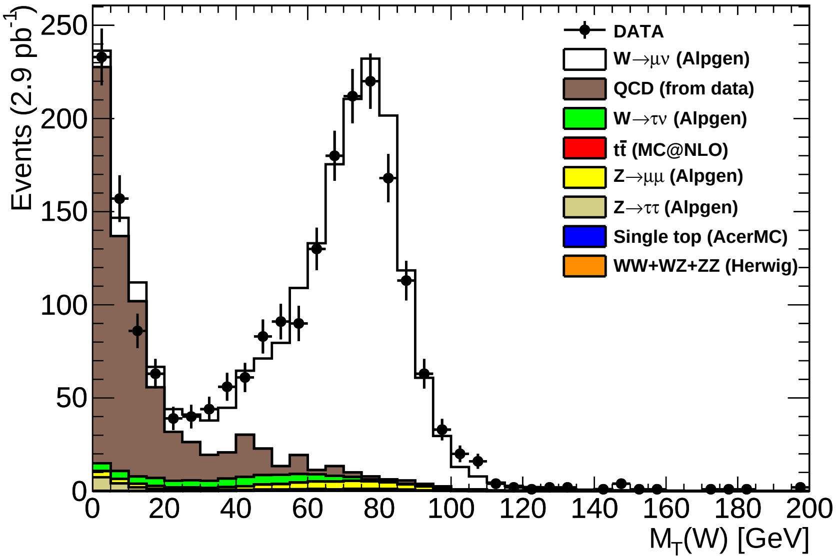

Figure 5.33: *Distribution of reconstructed transverse mass after exclusive $W \to \mu\nu+$ 1 jet candidate selection for data and Monte Carlo.*

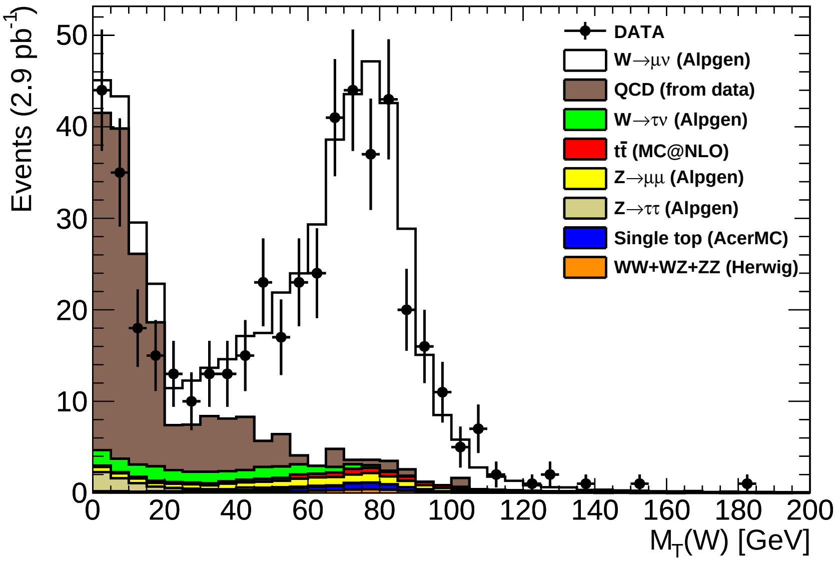

Figure 5.34: *Distribution of reconstructed transverse mass after exclusive* $W \rightarrow \mu\nu +$ *2 jets candidate selection for data and Monte Carlo.*

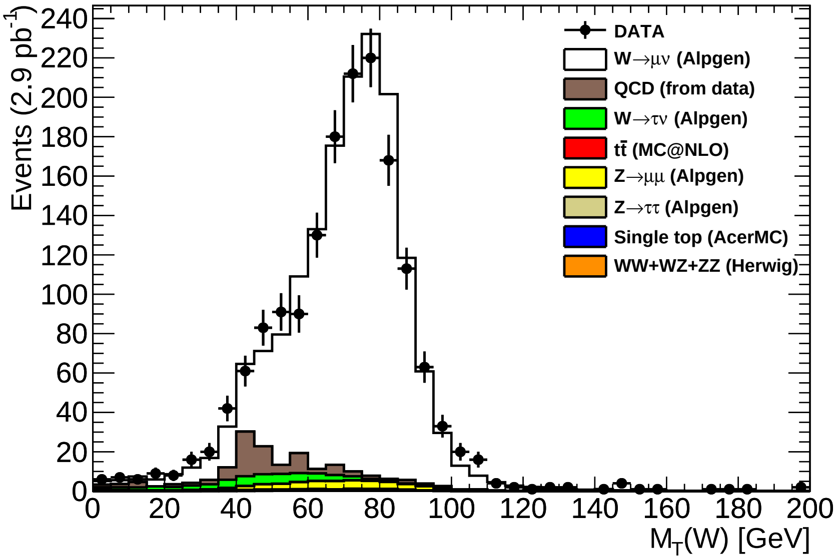

Figure 5.35: *Distribution of reconstructed transverse mass after exclusive* $W \rightarrow \mu\nu +$ *1 jet candidate selection with triangular cut for data and Monte Carlo.*

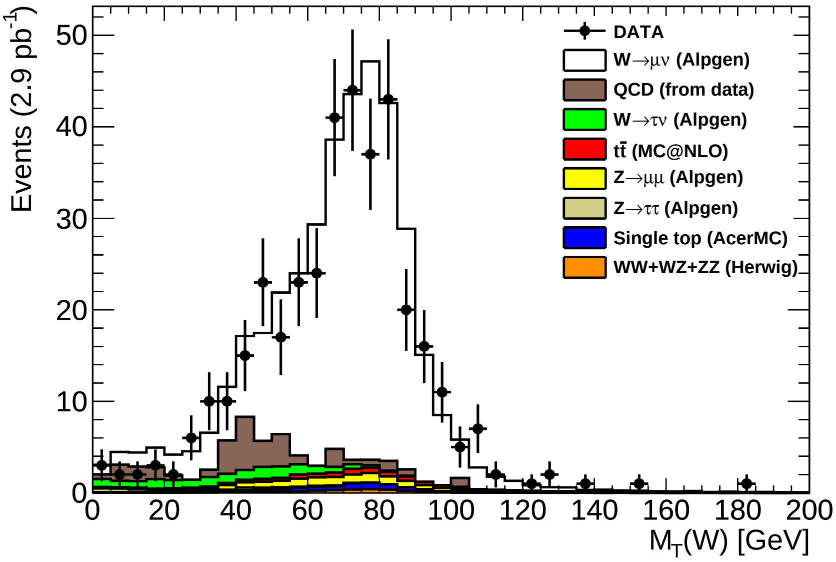

Figure 5.36: *Distribution of reconstructed transverse mass after exclusive* $W \rightarrow \mu\nu +$ *2 jets candidate selection with triangular cut for data and Monte Carlo.*

Using the measured rate of $W \rightarrow \mu\nu + 2$ jets as a control region the Berends scaling formula, see equation 5.6.2, is used to estimate the number of $W \rightarrow \mu\nu + 4$ jet events in the SR. The calculation is done separately for the baseline selection and with the triangular cut. The results are shown in Table 5.7. The uncertainties reported in the table contain statistical and systematic uncertainties added in quadrature. The details of the uncertainties are discussed in the next subsection. The final results for the measured $W \rightarrow \mu\nu + 4$ jets rates for the analysis scenarios without and with the triangular cut are $14.6 \pm 4.0(\text{stat}) \pm 5.6(\text{sys})$ and $17.3 \pm 4.0(\text{stat}) \pm 5.2(\text{sys})$ events, respectively. Both results are in good agreement with the Monte Carlo expectations. The value for the case with triangular cut turns out to be a bit larger than the case without the triangular cut, contradicting somewhat the intuition. The difference is well within the statistical uncertainty therefore it is interpreted as being due to a fluctuation in the data. The statistical uncertainties on the $W \rightarrow \mu\nu + 4$ jets rates results are in both cases already smaller than the systematic errors.

Table 5.7: *Estimation of the inclusive $W \rightarrow \mu\nu$+4 jets signal region selection in the data using the selection without and with the triangular cut.*

Input	W/o triang. cut	With triang. cut
Estimated $W \rightarrow \mu\nu$+1 jet	1450 ± 198	1427 ± 53
Estimated $W \rightarrow \mu\nu$+2 jets	291 ± 56	303 ± 28
Estimated $r = W + 2/W + 1$	0.201 ± 0.063	0.212 ± 0.024
Expected $r = W + 2/W + 1$	0.225	0.224
Measured $W \rightarrow \mu\nu$ + 4 jets	14.6 ± 6.9	17.3 ± 6.5
Expected $W \rightarrow \mu\nu$ + 4 jets	20.4	19.4

5.6.5 Uncertainties on W+jets background

There are two types of sources contributing to the uncertainty of the estimation of the W+jets rates: statistical and systematic. The statistical uncertainty is a reducible uncertainty which is limited by the amount of data collected by ATLAS, but which is expected to be reduced significantly in the near future. It is due to the finite sample size when counting events in the W+1 jet and W+2 jets bin. During calculation of the uncertainties a 100% correlation is assumed between the two jet bins.

The main source of systematics on the rate of W+ jets originates from the assumption that the ratio, $r = (W + 2\,\text{jets})/(W + 1\,\text{jet})$, is constant. Theoretical uncertainties associated with this assumption can originate from the matching of the fixed order tree level matrix element partons with the simulated parton showers. As mentioned before in Section 2.2 the partons after the hard subprocess enter into the regime of non-perturbative QCD. At this low energy scale regime the partons radiate and reconnect themselves to hadrons. The hard subprocess and the parton radiation are completely different calculations in theory, and therefore the partons in the perturbative hard scattering process must be matched to the radiated showers or jets in the non-perturbative case. This matching procedure has parameters, like the transverse momentum of the partons and the jets, the distance between the partons and the jets in the azimuth-pseudorapidity two dimensional space. Any theoretical estimation on the absolute rate of W+ jets events, and subsequently the ratio $r = (W + 2\text{ jets})/(W + 1\text{ jet})$, can be sensitive therefore on the parameters of the matching procedure which can lead to a systematic uncertainty. A study has been done to estimate the amount of this type of systematic uncertainty [26]. Hence, we use a 24% irreducible systematic uncertainty on the rate of W+jets based on the result of the paper [26] on parameter variation of matrix element generators to parton shower matching. As mentioned in Section 5.5.2 the total uncertainty on the data-driven matrix method QCD backround estimation is the square root of the statistical uncertainty on the measured fake rate and a 30% relative systematic uncertainty from the method added in quadrature.

During the estimation of the Standard Model backgrounds from Monte Carlo simulation the following systematic uncertainties have been used. For the $Z \to \mu\mu$, $Z \to \tau\tau$ and $W \to \tau\nu$ a 20% uncertainty is assumed. The justification for the amount of this uncertainty is that the $Z \to ll$ event rates have already been measured at ATLAS [49] with a precision of 10%. The relative rates of the $Z \to \tau\tau$ and $W \to \tau\nu$ final states with respect to their other leptonic final states can be estimated from Monte Carlo simulations with a reasonable precision. Therefore the 20% uncertainty is a conservative estimate. In case of the di-boson WW, WZ, ZZ and the almost negligible single top and top quark pair contamination in the control regions a total 100% relative systematic uncertainty have been used.

Jet energy scale has also its associated systematic uncertainties due to misreconstruction of jets in a multijet environment. In the case of the Berends scaling method to estimate the W+jets background the *ratio* of $W + 2$ jets to $W + 1$ jets event rates is used, hence due to the ratio the overall impact is reduced. The QCD multijet background rate is also measured from relative rates of events from the high statistics low missing transverse energy sideband region. Therefore the arguments are similar. It is important to emphasize that these major background contributions in the signal region are measured from the data itself. Therefore uncertainties estimated from simulation based studies cannot be quoted directly on the data-driven estimates. An attempt to estimate the possible size of the effect of such systematical uncertainty has been made based on Monte Carlo simulations: the expected $W+1$ and $W+2$ jets rates have been re-evaluated from the Monte Carlo samples with varied jet energy and momentum components with an amount of 5-10% (depending on the pseudorapidity and momentum of the jets, see Section 4.3), and then the impact of the variation on the Berends ratio, $r = W+2/W+1$, has been computed. As a result a 3-4% variation has been found on the Berends ratio itself. Variation of such an amount on the ratio has a negligible impact on the final results.

Chapter 6

Observation of top-antitop events

In this chapter the observation analysis is presented in the top signal region. As discussed in the previous chapter, events are selected after triggering on a single muon with p_T threshold of 10 GeV. After the trigger, the presence of exactly one, offline reconstructed, isolated muon with $p_T > 20$ GeV is required in the event. The events are also required to have missing transverse energy larger than 20 GeV. There are two analysis scenarios considered in the thesis: without and with the use of the triangular cut, $E_T^{\text{miss}} + M_T(W) < 60$ GeV. The two approaches let smaller or larger QCD multijet background rate into the control and signal regions. The top signal region is then defined by selecting events with at least four jets with $p_T > 25$ GeV. The full details of the object and event selection are summarized in Table 5.1 and Tables 5.2 and 5.3, respectively.

The distribution of missing transverse energy for the signal region selection is shown on Fig. 6.1 and 6.2 and both for with and without the triangular cut selection. The estimation of the expected number of background events in the top signal region is done similarly to the estimation of the $W+$ jets rates in the control regions (discussed in Chapter 5). The result on the data-driven $W \rightarrow \mu\nu + 4$ jets rate prediction is used for the normalization of this type of background in the signal region. For the QCD multijet background the same matrix method estimation is used. The other Standard Model backgrounds are estimated from the Monte Carlo expectations again. The total background is hence composed of these three components. The various background rates and the excess over the background in the inclusive 4 jets bin SR is summarized in Table 6.1.

Table 6.1: *Number of events surviving the inclusive 4 jets signal region selection in 2.88* pb^{-1} *of data, with and without the triangular cut.*

Process	W/o triang. cut	With triang. cut
Total candidates	68 ± 8.2	59 ± 7.7
Measured $W \rightarrow \mu\nu$	14.6 ± 6.9	17.3 ± 6.5
Estimated multijet	8.5 ± 3.9	3.7 ± 2.2
Estimated SM backgrounds	3.5 ± 0.7	2.8 ± 0.6
Total background	26.6 ± 7.9	23.9 ± 6.9
Excess over background	41.4 ± 11.5	35.1 ± 10.3

In both scenarios, with and without the triangular cut, the dominant background contribution is the $W \rightarrow \mu\nu$+jets process. For the selection without the triangular cut the $W \rightarrow \mu\nu$+jets is found to contribute to 21% of the total candidates. The second dominant background contribution is the multijet background, which is expected because the triangular cut suppresses the pure QCD multijet contamination. It is found to constitute 12% of the total candidates. The smallest background contributions are the other Standard Model background processes which are found to be at a few percent level.

For the analysis with the triangular cut applied, the $W \rightarrow \mu\nu$+jets background is estimated to be slightly higher, 29%. The absolute rate of estimated $W \rightarrow \mu\nu$+jets is also somewhat larger in case of the triangular cut, but this is probably due to a statistical fluctuation in the QCD background estimate in the control regions of the Berends scaling method. Both analyses yield an excess of similar size over the estimated background.

In the table the errors quoted contain the same type of statistical and systematic uncertainties that have been mentioned at the end of the previous chapter. The dominant uncertainty contribution is the statistical uncertainty in the signal region, the systematic uncertainty on the QCD background from the matrix method and the theoretical systematic uncertainty on the assumption that the $W+2/W+1$ jet ratio is constant.

Additionally to these uncertainties systematic uncertainty due to pile-up events has also been considered and found to have a negligible impact on the final result. Both the major backgrounds and the signal is extracted from the data, so the result may be sensitive to the presence of pile-up events in the data. This effect has been investigated as described in Section 5.3.6. The estimation of the impact has been done only at this final level of the analysis because the analysis is primarily data-driven and therefore pile-up might affect *both* the (data-driven) background estimate and the total data or excess extracted in the signal region. The whole analysis has been repeated with a cut on the Jet Vertex Fraction of $|\mathrm{JVF}| > 0.75$ to reduce jets that might originate from vertices produced in the same bunch crossings but from independent proton-proton interactions. The impact on the final excess has been found to be $< 1\%$ for both analysis scenarios.

The resulting missing transverse and jet multiplicity distributions in the signal region of inclusive four jets selection are shown on Figures 6.1, 6.2 and 6.3,6.4, respectively. The two backgrounds, W+jets and multijet, dominate the distributions and all the plots suggest an excess in the data over a background-only hypothesis. Adding the $t\bar{t}$ Monte Carlo simulation to the data-driven backgrounds there is a good agreement between the data and the backgrounds plus the $t\bar{t}$ signal. In case of the production of real top pair events in the muon plus jets final state, the invariant mass of the three-jet system from the top and the hadronically decaying W boson can be reconstructed. First, hadronically decaying W candidates are selected, after the four jet inclusive signal region selection, by finding the two-jet combination in the events leading to the highest transverse momentum. Then each of the remaining jets are combined with the two-jet system separately until the three-jet system with the highest transverse momentum is found. The resulting three-jet invariant mass distributions are shown on Figures 6.5 and 6.6 for the analysis scenario without and with triangular cut, respectively.

The figures show that the data distributions have a peak structure with a maximum at around a reconstructed top candidate mass of $150 - 170$ GeV. The distributions from the Monte Carlo simulations show that such three-jet invariant mass distributions are expected to be dominated by the top quark pair signal.

Using the ratio of Poisson means (see Appendix B) as a statistical test of the background-only hypothesis the statistical significance of the excess has been estimated. For the two analysis scenarios, without and with the triangular cut, one sided Gaussian standard deviations of 3.1 and 3.0, respectively, have been obtained. The level of the excess found in the data is consistent with Monte Carlo expectation for $t\bar{t}$ events (see Tables 5.2 and 5.3). Therefore it is a 3 sigma observation of top quark pair production in proton-proton collisions at 7 TeV center-of-mass energy.

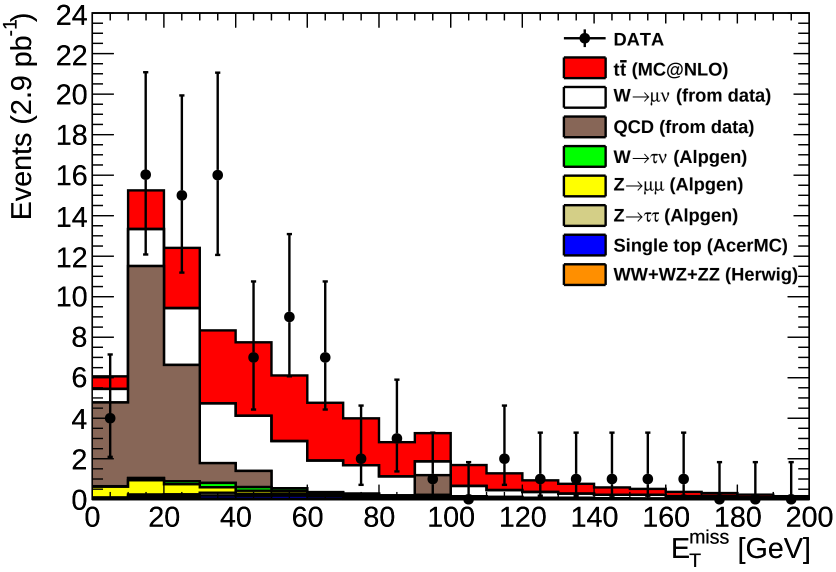

Figure 6.1: *Distribution of transverse missing energy after inclusive 4 jets candidate selection on data and Monte Carlo, without the triangular cut.*

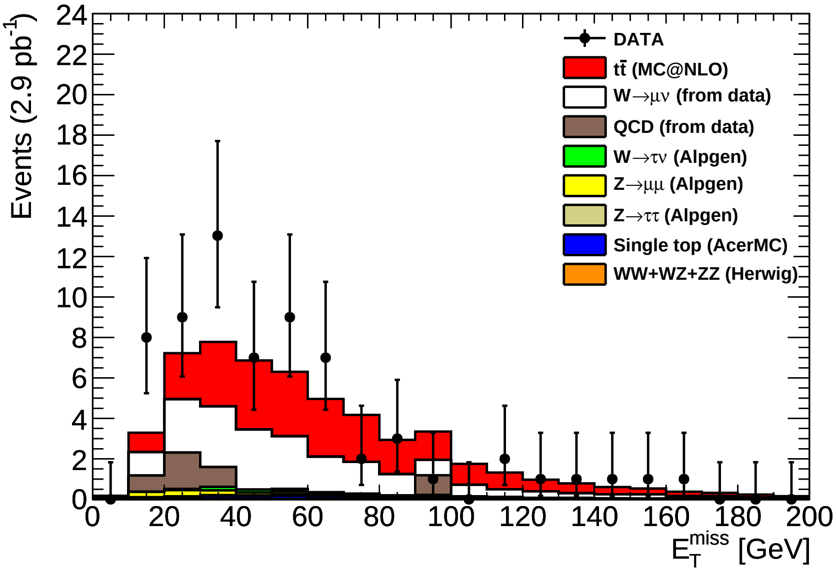

Figure 6.2: *Distribution of transverse missing energy after inclusive 4 jets candidate selection on data and Monte Carlo, with the triangular cut.*

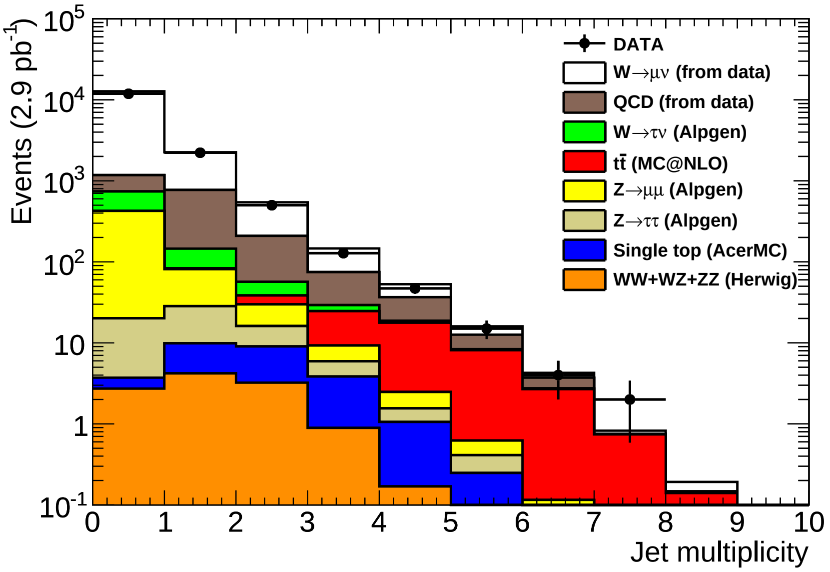

Figure 6.3: *Distribution of jet multiplicity in data and Monte Carlo, without the triangular cut.*

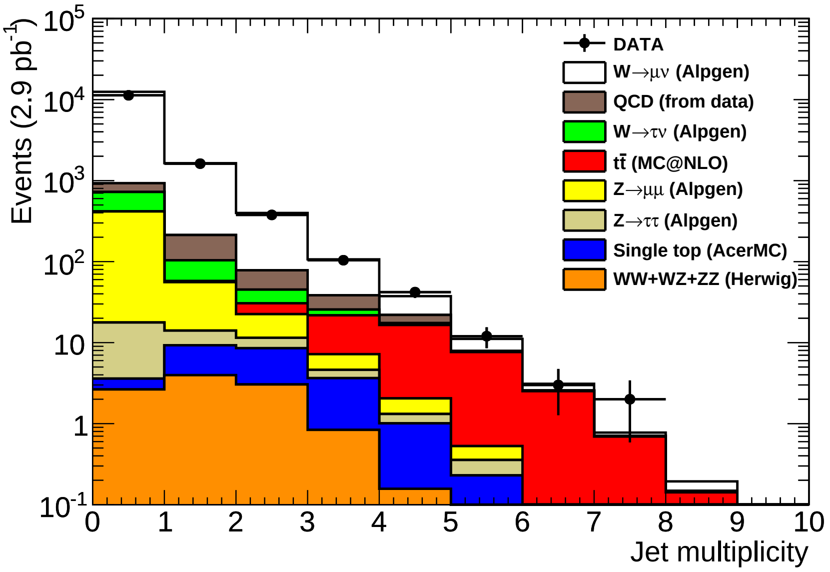

Figure 6.4: *Distribution of jet multiplicity in data and Monte Carlo, with the triangular cut.*

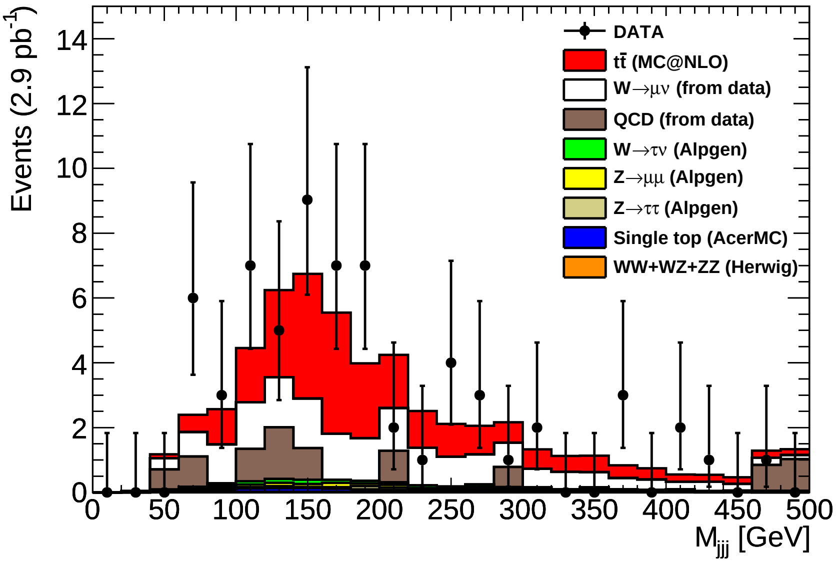

Figure 6.5: *Distribution of reconstructed three jet invariant mass for the three jet combination leading to the highest* p_T^{jjj} *in data and Monte Carlo, without the triangular cut.*

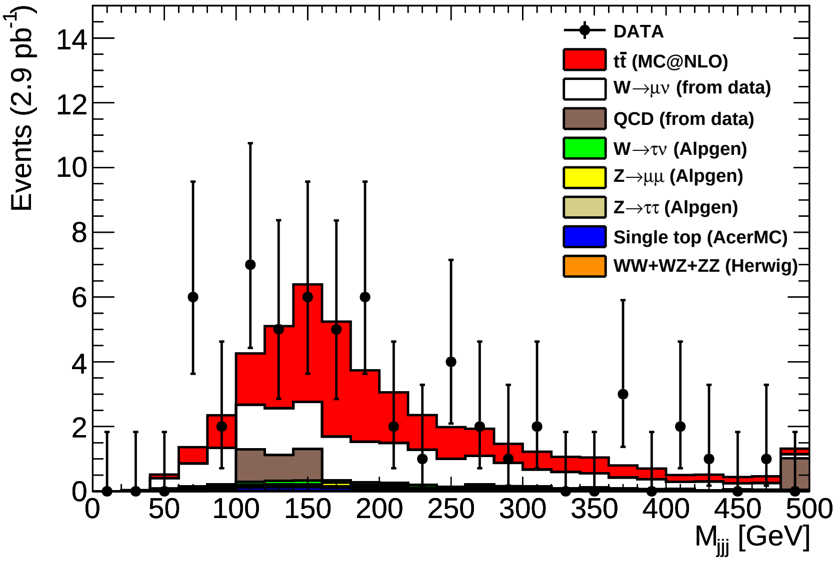

Figure 6.6: *Distribution of reconstructed three jet invariant mass for the three jet combination leading to the highest* p_T^{jjj} *in data and Monte Carlo, with the triangular cut.*

Chapter 7

Summary

An analysis has been presented based on an integrated luminosity of 2.9 pb^{-1} of 7 TeV center-of-mass energy proton-proton collision data in ATLAS at the Large Hadron Collider. The data have been collected since March until September of 2010. Clear signals from $W+$ jets and $Z+$ jets events have been seen. The aim of the analysis is to observe top quark pair production in the collision data. Two analysis approaches have been used independently and yielded consistent result. The first approach allowed more multijet background in the data in order to estimate its rate reliably. The other approach introduced a discriminator selection to suppress the multijet background. The dominant background contributions in the signal region are W+jets and multijet production processes. The rates of these backgrounds in the signal region have been estimated with data-driven methods using signal-free, sideband regions as auxiliary measurements. The use of Monte Carlo simulation based normalizations were minimized as much as possible.

After applying the signal region event selection cuts 23.9±6.9 background and 35.1±10.3 signal candidate events have been found. Assuming a background-only hypothesis in the data a one sided Gaussian sigma excess of 3.0 over the background has been observed. The size of the excess is consistent with the expectation for top quark pair production in the data.

The increasing amount of data at the LHC allows further refinement of the top quark observation analysis. Better understanding of W+jets, Z+jets and

QCD multijet events will lead to better background estimations in the top signal region. Observation of top quark pair production, at a level of more than 5 standard deviations, is expected as a result of the analysis of the full proton-proton collision data collected over the year 2010.

Bibliography

[1] C. Amsler et al. (Particle Data Group). *Review of Particle Physics*. *Phys. Lett.*, B667, 2008.

[2] S.Abachi et al. (D0). *Phys.Rev.Lett.*, 74(2632), April 1995.

[3] F.Abe et al. (CDF). *Phys.Rev.Lett.*, 74:2626, April 1995.

[4] G.Aad et al. (ATLAS). *J.Inst.*, Vol. 3, August 2008.

[5] F.Mandl, G.Shaw. *Quantum Field Theory.* John Wiley & Sons, 1984.

[6] A.D.Martin F.Halzen. *Quarks & Leptons: An Introductory Course in Modern Particle Physics.* John Wiley & Sons, 1984.

[7] G.Arnison et al. (UA1 Collaboration). *Experimental Observation Of Isolated Large Transverse Energy Electrons With Associated Missing Energy At* $\sqrt{s} = 540\ GeV$. *Phys. Lett.*, B 122, 1983.

[8] G.Arnison et al. (UA1 Collaboration). *Experimental Observation Of Lepton Pairs Of Invariant Mass Around 95 GeV/c*^{2} *At The Cern Sps Collider*. *Phys. Lett.*, B 126, 1983.

[9] A. Salam. *Elementary Particle Theory*. *Proc. 8th Nobel Symp., Aspenäsgården, ed. by N. Svartholm (Almqvist and Wiksell), Stockholm,* 1968.

[10] S. Weinberg. *A Model Of Leptons*. *Phys. Rev. Lett.*, 19, 1967.

[11] T.D.Lee, C.N.Yang. *Phys.Rev.*, 104, October 1956.

[12] C.S.Wu et al. *Phys.Rev.*, 105, February 1957.

[13] Richard L., Garwin et al. *Phys.Rev.*, 105, February 1957.

[14] P. W. Higgs. *Phys. Lett. 12*, 1964.

[15] D. Schaile and P.M. Zerwas. *Measuring the weak isospin of b quarks in e+e- annihilation*. *Phys.Rev.*, D45, 1992.

[16] G. Sterman et al. *Handbook of Perturbative QCD*. *Rev. Mod. Phys.*, 67, 1995.

[17] Davison E. Collins, John C., Soper. *Parton distribution and decay functions*. *Nucl. Phys. B*, 194, 1982.

[18] G. Altarelli and G. Parisi. *Nucl. Phys. B*, 126, 1977.

[19] L. N. Lipatov. *Sov. J.Nucl. Phys.*, 20, 1975.

[20] V. N. Gribov and L. N. Lipatov. *Sov. J.Nucl. Phys.*, 15, 1972.

[21] Yu. L. Dokshitzer. *Sov. Phys. JETP*, 46, 1977.

[22] The CTEQ Collaboration, H.L. Lai et al. *Eur. Phys. J. C*, 12, 2000.

[23] A.D. Martin et al. *Eur.Phys. J. C*, 63, 2009.

[24] G. Corcella, I.G. Knowles, G. Marchesini, S. Moretti, K. Odagiri, P. Richardson, M.H. Seymour and B.R. Webber. HERWIG 6.5. *JHEP*, 0101, 2001.

[25] T. Sjostrand, S. Mrenna and P. Skands. *PYTHIA 6.4 Physics and Manual*. *JHEP*, 05, 2006.

[26] J. Alwall et. al. *Comparative study of various algorithms for the merging of parton showers and matrix elements in hadronic collisions*. *http://arxiv.org/abs/0706.2569*, 2008.

[27] Paolo Nason Stefano Frixione and Bryan R. Webber. *JHEP*, 007, 2003.

[28] U. Langenfeld, S. Moch, and P. Uwer. *Phys. Rev.*, D80:054009, 2009.

[29] M. Jezabek and J. H. Kuhn. *QCD corrections to semileptonic decays of heavy quarks. Nuclear Physics B*, 314(1):1 – 6, 1989.

[30] A. Shibata et al. *Understanding Monte Carlo Generators for Top Physics*. *ATL-COM-PHYS-2009-334*, 2009.

[31] J. Butterworth et al. *Zeit. für Phys.*, C72, 1996.

[32] M. L. Mangano, M. Moretti, F. Piccinini, R. Pittau, and A. D. Polosa. *ALPGEN, a generator for hard multiparton processes in hadronic collisions*. *JHEP*, 07, 2003.

[33] J. Alwall et al. *Eur. Phys. J.*, C53, 2008.

[34] S.Ask, D.Malon, T.Pauly, M.Shapiro. *Report from the Luminosity Task Force*. *ATL-GEN-PUB-2006-002*.

[35] A.Bertin et al. *Calibrating the ATLAS luminosity detectors using beam separation scans*. *ATL-COM-LUM-2010-023*.

[36] D.Berge et al. *Determination of the absolute luminosity and the visible cross section from LHC van der Meer scans using events with MBTS triggers and with primary vertices*. *ATL-COM-LUM-2010-021*.

[37] S. Agostinelli et al. GEANT4: A simulation toolkit. *NIM A*, 506, 2003.

[38] G. Aad et al. *Expected Performance of the ATLAS Experiment - Detector, Trigger and Physics*. *arXiv:0901.0512, CERN-OPEN-2008-020*, 2009.

[39] G. Aad et al. *Electron and photon reconstruction and identification in ATLAS: expected performance at high energy and results at* $\sqrt{s} = 900$ *GeV*. *ATLAS conference note: ATLAS-CONF-2010-005*, 2010.

[40] G. P. Salam M. Cacciari and G. Soyez. *JHEP*, 04, 2008.

[41] M. Begel et al. *Jet energy scale and its systematic uncertainty for jets produced in proton-proton collisions at* $\sqrt{s} = 7$ *GeV and measured with the ATLAS detector*. *ATL-COM-PHYS-2010-404*, 2010.

[42] *Performance of the Missing Transverse Energy Reconstruction and Calibration in Proton-Proton Collisions at a Center-of-Mass Energy of* $\sqrt{s} = 7$ *TeV with the ATLAS Detector*. *ATLAS-CONF-2010-371*, 2010.

[43] *Muon Reconstruction Performance*. *ATLAS-COM-PHYS-2010-430*, 2010.

[44] M. Baak et al. *Data Quality Status Flags and Good Run Lists for Physics Analysis in ATLAS*. *ATL-COM-GEN-2009-015*, 2009.

[45] B. Abbott et al. *Study on reconstructed object definition and selection for top physics*. *ATLAS-COM-PHYS-2009-633*, 2009.

[46] D. W. Miller, A. Schwartzman, D. Su. . *ATL-COM-PHYS-2009-180*, 2009.

[47] F. A. Berends, W. T. Giele, H. Kuijf, R. Kleiss, W. J. Stirling. *Physics Letters B*, 224, 1989.

[48] E. Abouzaid, H. Frisch. *Phys. Rev. D*, 68, 2003.

[49] The ATLAS Collaboration. *Measurement of the* $Z \rightarrow ll$ *production cross section in proton-proton collisions at* $\sqrt{s} = 7$ *TeV with the ATLAS detector*. *ATLAS-CONF-2010-076*, 2010.

[50] J.T.Linnemann. *Measures of Significance in HEP and Astrophysics*. *http://arxiv.org/abs/physics/0312059*, 2003.

Appendix A

Berends scaling

The prove here is given that for $r \in \mathbb{R}_+$, $r < 1$

$$\boxed{S_2^{(\infty)} \equiv \sum_{i=2}^{\infty} r^i = \frac{r^2}{1-r}\ , r \in \mathbb{R}_+, r < 1} \tag{A.1}$$

First observe that $S_2^{(\infty)}$ is equivalent with $r^2 \cdot S_0^{(\infty)}$

$$S_2^{(\infty)} = \sum_{i=2}^{\infty} r^i = r^2 + r^3 + r^4 + \cdots + r^{\infty} = r^2 \cdot (1 + r + r^2 + \cdots + r^{\infty}) \tag{A.2}$$

$$S_2^{(\infty)} = r^2 \cdot \sum_{i=0}^{\infty} r^i = r^2 \cdot S_0^{(\infty)} \tag{A.3}$$

Then take a finite series whose index, i, runs from 0 to n,

$$S_0^{(n)} \equiv \sum_{i=0}^{n} r^i = 1 + r + r^2 + \cdots + r^n. \tag{A.4}$$

Multiplying $S_0^{(n)}$ by r yields

$$r \cdot S_0^{(n)} = r \cdot \sum_{i=0}^{n} r^i = r + r^2 + r^3 + \cdots + r^{n+1}. \tag{A.5}$$

Let us subtract Eq. A.5 from Eq. A.4,

$$S_0^{(n)} - r \cdot S_0^{(n)} = (1 - r) \cdot S_0^{(n)} = 1 - r^{n+1}, \tag{A.6}$$

therefore from this it follows that

$$S_0^{(n)} = \sum_{i=0}^{n} r^i = \frac{1 - r^{n+1}}{1 - r}. \tag{A.7}$$

Now express $S_2^{(n)}$ in terms of $S_0^{(n)}$,

$$S_2^{(n)} = r^2 \cdot S_0^{(n)} = r^2 \cdot \frac{1 - r^{n+1}}{1 - r} = \frac{r^2 - r^{n+3}}{1 - r}\ . \tag{A.8}$$

But we are interested in the case of $n \to \infty$ and in such a case $r^{n+3} \to 0$, because the condition was that $r < 1$. Therefore taking n to infinity yields

$$S_2^{(n)} \to S_2^{(\infty)} = \frac{r^2}{1 - r}\ . \tag{A.9}$$

Appendix B

Hypothesis test on the ratio of Poisson means

Both in case of astrophysics or particle physics a general problem is to be able to make a statistical statement on whether an observation of a Poisson process in an expected signal/source region is consistent with a background-only hypothesis. Consider a counting experiment where one counts the number of events in a region where one expects the signal. One then usually tries to estimate the number of background events in the signal region from a subsidiary or sideband measurement from the data itself. The statistical hypothesis test can be then constructed on the *ratio* of the observed number of background events in the signal-free region to the observed number of events in the potential signal region [50]. In the language of statistics the hypothesis test in this case is to calculate the probability that the number of background events in the signal region is as *extreme* as the observed one or higher. That is whether the observed number of events from the Poisson process is consistent with a fluctuation in the background only. The focus in statistics is usually on the *significance level*, α, of the hypothesis test, also known as the size of the test. In the formal theory of Neyman-Pearson hypothesis testing, α is specified in advance; once data are obtained, the *p-value* is the smallest value of α for which the background-only hypothesis would be rejected. Frequently the p-value is communicated by specifying the corresponding number of standard deviations in a one-tailed test of a Gaussian (normal) variate, that is one gives a Z-value given by

$$Z = \Phi^{-1}(1-p) = -\Phi^{-1}(p) \ , \tag{B.1}$$

where

$$\Phi(Z) = \frac{1}{\sqrt{2\pi}} \int_{-\infty}^{Z} exp(-t^2/2)dt = \frac{1 + \mathrm{erf}(Z/\sqrt{2})}{2} \tag{B.2}$$

so that

$$Z = \sqrt{2}\, \mathrm{erf}^{-1}(1-2p) \ . \tag{B.3}$$

For example, $Z = 3$ corresponds to a p-value of 1.35×10^{-3}. This relation can be approximated to better than 1% for $Z > 1.6$ as

$$Z \approx \sqrt{u - \ln u} \ , \tag{B.4}$$

where $u = -2\ln(p\sqrt{2\pi})$.

Let us denote the total observed number of events in a potential signal region as n_{on}, and the total observed number of events in the sideband region as n_{off}[1]. The expected value of n_{off} in the signal-free region we denote as μ_{off}, that of the n_{on} as μ_{on}, and the expected value of the background in the signal region we denote as μ_b. Let τ denote the ratio of expected means of n_{off} and n_{on} in case of the background-only hypothesis, that is when $\mu_{on} = \mu_b$,

$$\tau \equiv \mu_{off}/\mu_b. \tag{B.5}$$

In general τ is known from the sideband measurement and from some other assumptions (shape of the background, etc.). The point estimate of μ_{off} is n_{off}, therefore the point estimate of μ_b is

$$\hat{\mu}_b = n_{off}/\tau \ . \tag{B.6}$$

---

[1] The astrophysics equivalent is: the observation of n_{on} photons when a telescope is pointing at a potential source ("on-source") includes both background and the source, while the observation of n_{off} photons with the telescope pointing at a source-free direction nearby ("off-source") is the subsidiary measurement.

A *rough* estimate of the uncertainty on estimating μ_{off} by n_{off} is $\sqrt{n_{off}}$. From this it follows that an estimate of the uncertainty on $\hat{\mu}_b$ is

$$\sigma_b = \sqrt{n_{off}}/\tau \ , \tag{B.7}$$

which can be combined with Eq.B.6 to yield

$$\tau = \hat{\mu}_b/\sigma_b^2 = 1/(\hat{\mu}_b \delta_{b,rel}^2) \ , \tag{B.8}$$

where $\delta_{b,rel}^2$ is the relative uncertainty on the background estimate in the signal region, $\hat{\mu}_b$. This is a useful *approximation* to relate the uncertainty on the background estimtate to τ. Each of n_{on} and n_{off} is a sample from a Poisson probability with unknown means μ_{on} and μ_{off}; the background-only hypothesis is therefore that the *ratio of Poisson means*, $\lambda = \mu_{off}/\mu_{on}$, is equal to the corresponding ratio with background only, τ.

The joint probability of observing n_{on} and n_{off} is the product of Poisson probabilities for n_{on} and n_{off}, and can be rewritten as the product of a single Poisson probability with mean $\mu_{tot} = \mu_{on}+\mu_{off}$ for the total number of events n_{tot}, and the binomial probability that this total is divided as observed if the binomial parameter ρ is $\rho = \mu_{on}/\mu_{tot} = 1/(1+\lambda)$,

$$\begin{aligned} P(n_{on}, n_{off}) &= \frac{e^{-\mu_{on}}\mu_{on}^{n_{on}}}{n_{on}!} \times \frac{e^{-\mu_{off}}\mu_{off}^{n_{off}}}{n_{off}!} = \\ &= \frac{e^{-(\mu_{on}+\mu_{off})}(\mu_{on}+\mu_{off})^{n_{tot}}}{n_{tot}!} \times \\ &\frac{n_{tot}!}{n_{on}!(n_{tot}-n_{on})!}\rho^{n_{on}}(1-\rho)^{(n_{tot}-n_{on})} \ . \end{aligned} \tag{B.9}$$

That is, rewriting in terms of observables (n_{on}, n_{tot}) and parameters (λ, μ_{tot}),

$$P(n_{on}, n_{off}; \mu_{on}, \mu_{off}) = P(n_{tot}; \mu_{on}+\mu_{off}) P(n_{on}|n_{tot}; \rho) \tag{B.10}$$

$$= P(n_{tot}; \mu_{tot}) P(n_{on}|n_{tot}; 1/(1+\lambda)), \tag{B.11}$$

where on the right-hand side the probabilities P are Poisson and binomial, respectively. In this form, all the information about the ratio of Poisson

means, λ, is in the *conditional* binomial probability for the observed successes n_{on}, given the observed total number of events $n_{tot} = n_{on} + n_{off}$.
The p-value for the test of $\rho = 1/(1+\tau)$, and hence of the background-only hypothesis, is then the one-tailed probability sum

$$p = \sum_{j=n_{on}}^{n_{tot}} P(j|n_{tot};\rho) = \sum_{j=n_{on}}^{n_{tot}} \frac{n_{tot}!}{j!(n_{tot}-j)!}\rho^j(1-\rho)^{(n_{tot}-j)} \ . \tag{B.12}$$

This can be computed from the ratio of incomplete and complete beta functions

$$p = B(\rho; n_{on}, n_{off}+1)/B(n_{on}, n_{off}+1). \tag{B.13}$$

This can be seen from the definition of the incomplete and complete beta functions. The incomplete beta function is defined as

$$B(w;p,q) = \int_{x=0}^{w} x^{p-1}(1-x)^{q-1}dx \ . \tag{B.14}$$

The complete beta function is defined as

$$B(p,q) = \frac{(p-1)!(q-1)!}{(p+q-1)!} \ . \tag{B.15}$$

The corresponding Z-value then follows using Eq. B.3.
As an illustration Fig B.1 shows the distribution of the binomial probability, $P(j|n_{tot};\rho)$, of observing j events for the case of $n_{tot} = 78$ and $\rho = 0.56$, and showing an actual number of observed events at $j = 60$. The p-value is extracted as the integral of the probability distribution from the number of observed events to n_{tot}, as shown in the subfigure with filled area.

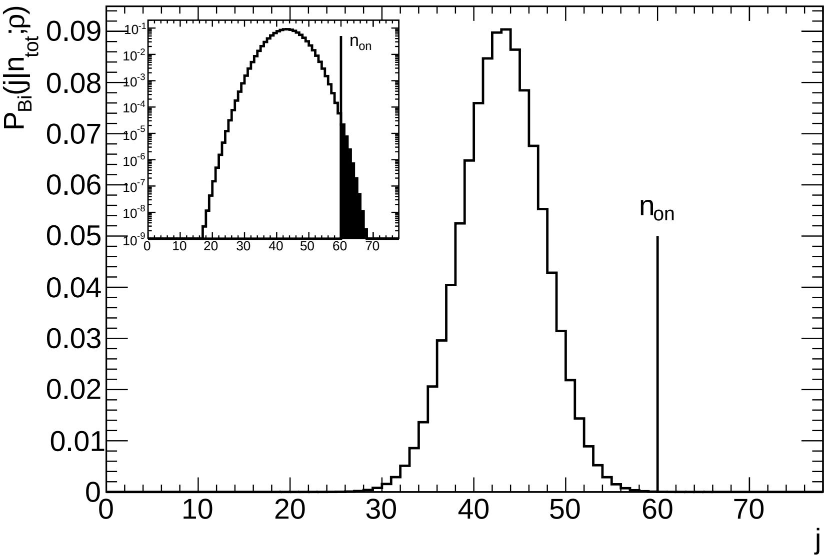

Figure B.1: *Binomial probability distribution for the background-only hypothesis,* $P(j|n_{tot};\rho)$*, as test statistic for the ratio of Poisson means, as a function of the number of events in the signal region,* j*. The actual observed number of events,* n_{on}*, is indicated with a vertical line, while the tail integral is indicated as filled histogram in the subfigure where a logarithmic scale is used for* P *(upper left corner).*

Appendix C

Monte Carlo cross sections

Table C.1: *List of processes and cross sections used for the normalization of the Monte Carlo samples.*

Process (generator)	σ **(pb)**
$t\bar{t}$ (MC@NLO)	87.4
$W \to \mu\nu + 0$ parton (Alpgen)	8461.2
$W \to \mu\nu + 1$ parton (Alpgen)	1563.1
$W \to \mu\nu + 2$ parton (Alpgen)	457.9
$W \to \mu\nu + 3$ parton (Alpgen)	123.3
$W \to \mu\nu + 4$ parton (Alpgen)	31.3
$W \to \mu\nu + 5$ parton (Alpgen)	8.5
$W \to \tau\nu + 0$ parton (Alpgen)	8339.7
$W \to \tau\nu + 1$ parton (Alpgen)	1557.7
$W \to \tau\nu + 2$ parton (Alpgen)	459.4
$W \to \tau\nu + 3$ parton (Alpgen)	123.0
$W \to \tau\nu + 4$ parton (Alpgen)	31.3
$W \to \tau\nu + 5$ parton (Alpgen)	8.5

Table C.2: *List of processes and cross sections used for the normalization of the Monte Carlo samples.*

Process (generator)	σ **(pb)**
$Z \rightarrow \mu\mu + 0$ parton (Alpgen)	802.4
$Z \rightarrow \mu\mu + 1$ parton (Alpgen)	162.0
$Z \rightarrow \mu\mu + 2$ parton (Alpgen)	48.3
$Z \rightarrow \mu\mu + 3$ parton (Alpgen)	13.5
$Z \rightarrow \mu\mu + 4$ parton (Alpgen)	3.4
$Z \rightarrow \mu\mu + 5$ parton (Alpgen)	1..0
$Z \rightarrow \tau\tau + 0$ parton (Alpgen)	802.0
$Z \rightarrow \tau\tau + 1$ parton (Alpgen)	162.3
$Z \rightarrow \tau\tau + 2$ parton (Alpgen)	49.3
$Z \rightarrow \tau\tau + 3$ parton (Alpgen)	13.4
$Z \rightarrow \tau\tau + 4$ parton (Alpgen)	3.5
$Z \rightarrow \tau\tau + 5$ parton (Alpgen)	0.8
WW (Herwig)	11.7
ZZ (Herwig)	1.0
WZ (Herwig)	3.4
Single top, Wt channel (MC@NLO)	14.6
Single top, t-channel ($\mu\nu$) (MC@NLO)	7.2
Single top, t-channel ($\tau\nu$) (MC@NLO)	7.1
Single top, s-channel ($\mu\nu$) (MC@NLO)	0.5
Single top, s-channel ($\tau\nu$) (MC@NLO)	0.5